

**EFFECTS OF SHEAR VELOCITY ON FRACTURE  
SHEAR STRENGTH OF ROCKS UNDER  
CONFINEMENTS**



**Matsee Kleepmek**

**A Thesis Submitted in Partial Fulfillment of the Requirements for the  
Doctor of Philosophy of Engineering in Geotechnology**

**Suranaree University of Technology**

**Academic Year 2014**

ผลกระทบของอัตราการเงินต่อกำลังเงินของรอยแตกในหิน  
ภายใต้ความดันล้อมรอบ



นางสาวมัทรี กลีบเมฆ

วิทยานิพนธ์นี้เป็นส่วนหนึ่งของการศึกษาตามหลักสูตรปริญญาวิศวกรรมศาสตรดุษฎีบัณฑิต  
สาขาวิชาเทคโนโลยีธรณี  
มหาวิทยาลัยเทคโนโลยีสุรนารี  
ปีการศึกษา 2557

# **EFFECTS OF SHEAR VELOCITY ON FRACTURE SHEAR STRENGTH OF ROCKS UNDER CONFINEMENTS**

Suranaree University of Technology has approved this thesis submitted in partial fulfillment of the requirements for the Degree of Doctor of Philosophy.

Thesis Examining Committee

---

(Dr. Decho Phueakphum)

Chairperson

---

(Prof. Dr. Kittitep Fuenkajorn)

Member (Thesis Advisor)

---

(Assoc. Prof. Ladda Wannakao)

Member

---

(Dr. Prachya Tepnarong)

Member

---

(Dr. Anisong Chitnarin)

Member

---

(Prof. Dr. Sukit Limpijumnong)

Vice Rector for Academic Affairs  
and Innovation

---

(Assoc. Prof. Flt. Lt. Dr. Kontorn Chamniprasart)

Dean of Institute of Engineering

มัทรี กลีบเมฆ : ผลกระทบของอัตราการเฉือนต่อกำลังเฉือนของรอยแตกในหินภายใต้ความดันล้อมรอบ (EFFECTS OF SHEAR VELOCITY ON FRACTURE SHEAR STRENGTH OF ROCKS UNDER CONFINEMENTS) อาจารย์ที่ปรึกษา : ศาสตราจารย์ ดร.กิตติเทพ เฟื่องขจร, 119 หน้า.

วัตถุประสงค์ของการศึกษานี้คือ เพื่อหาผลกระทบของอัตราการเฉือนต่อกำลังเฉือนสูงสุดและกำลังเฉือนคงเหลือของรอยแตกที่ทำขึ้นในห้องปฏิบัติการในหินแกรนิต หินทราย และหินมาร์ล กิจกรรมสำคัญคือ การทดสอบกำลังเฉือนภายใต้ความเค้นในสามแกนและมีความดันล้อมรอบสูงถึง 18 เมกะปาสคาล โดยใช้โครงกดในสามแกน รอยแตกที่ศึกษาจะประกอบด้วยรอยแตกที่ทำขึ้นภายใต้ความเค้นดึง และรอยแตกที่ทำขึ้นจากการตัดผิวเรียบ ความเร็วในการเฉือนผันแปรจาก  $1.15 \times 10^{-5}$  ถึง  $1.15 \times 10^{-2}$  มิลลิเมตรต่อวินาที ผลการทดสอบระบุว่า กำลังเฉือนสูงสุดและกำลังเฉือนคงเหลือลดลงตามความเร็วในการเฉือน ผลกระทบของความเร็วในการเฉือนปรากฏเด่นชัดสำหรับรอยแตกที่มีความขรุขระมาก ซึ่งพฤติกรรมนี้จะเห็นได้จากค่ากำลังเฉือนที่สูงสุดและกำลังเฉือนคงเหลือ กำลังเฉือนของรอยแตกผิวเรียบจะไม่ขึ้นกับความเร็วในการเฉือน เกณฑ์ของค่ากำลังเฉือนสูงสุดได้ถูกพัฒนาขึ้น โดยได้รวมผลกระทบของความดันล้อมรอบและความเร็วในการเฉือนไว้ในสมการ เกณฑ์นี้สามารถอธิบายกำลังเฉือนของรอยแตกภายใต้ความดันล้อมรอบและต่อเนื่องลงมาถึงสภาวะที่รอยแตกไม่มีความดันล้อมรอบ ดังเช่นสภาวะของการทดสอบกำลังเฉือนแบบตรง เกณฑ์นี้มีประโยชน์ในการคาดคะเนกำลังเฉือนของรอยแตกในหินที่มีอัตราการเคลื่อนตัวและภายใต้ความดันล้อมรอบที่ต่างไปจากค่าที่ใช้ในการศึกษานี้

สาขาวิชา เทคโนโลยีธรณี

ปีการศึกษา 2557

ลายมือชื่อนักศึกษา \_\_\_\_\_

ลายมือชื่ออาจารย์ที่ปรึกษา \_\_\_\_\_

MATSEE KLEEMK : EFFECTS OF SHEAR VELOCITY ON  
FRACTURE SHEAR STRENGTH OF ROCKS UNDER CONFINEMENTS.  
THESIS ADVISOR: PROFESSOR KITTEP FUENKAJORN, Ph.D., P.E.,  
118 PP.

#### ROCK FRACTURE/SHEAR VELOCITY/TRIAXIAL/DILATION

The objective of this study is to laboratory determine the effects of shear velocity on the peak and residual strengths of fractures artificially prepared in granite, sandstone and marl. The primary effort involves performing triaxial shear tests with confining stresses up to 18 MPa using a polyaxial load fame. Both tension-induced fractures and saw-cut surfaces are tested. The shear displacement velocities vary from  $1.15 \times 10^{-5}$  to  $1.15 \times 10^{-2}$  mm/s. The results indicate that the peak and residual shear strengths proportionally decrease with shear velocity. The shear velocity effects pronounce more on the fractures with high JRC values. This holds true for both peak and residual shear strengths. Shear strength of smooth fractures tends to be independent of the shear velocity. An empirical shear strength criterion is derived to explicitly incorporate the effects of confining pressure and shear velocity. The proposed criterion allows a reasonably good transition from the high confinement shear strengths to the unconfined condition (direct shear test). The criterion is useful for predicting the shearing resistance of rock fractures under displacement velocities and confining pressures beyond those used in this study.

School of Geotechnology

Academic Year 2014

Student's Signature \_\_\_\_\_

Advisor's Signature \_\_\_\_\_

## ACKNOWLEDGMENTS

I wish to acknowledge the funding supported by Suranaree University of Technology (SUT).

I would like to express my sincere gratitude thanks to Prof. Dr. Kittitep Fuenkajorn for his valuable guidance and efficient supervision. I appreciate for his strong support, encouragement, suggestions and comments during the research period. My heartiness thanks to Dr. Decho Phueakphum, Assoc. Prof. Ladda Wannakao, Dr. Prachya Tepnarong and Dr. Anisong Chitnarin for their constructive advice, valuable suggestions and comments on my research works as thesis committee members. Grateful thanks are given to all staffs of Geomechanics Research Unit, Institute of Engineering who supported my work.

Finally, I would like to thank beloved parents for their love, moral support and constant encouragement.

Matsee Kleepmek

# TABLE OF CONTENTS

	<b>Page</b>
ABSTRACT (THAI) .....	I
ABSTRACT (ENGLISH).....	II
ACKNOWLEDGEMENTS.....	III
TABLE OF CONTENTS.....	IV
LIST OF TABLES.....	VII
LIST OF FIGURES .....	IX
SYMBOLS AND ABBREVIATIONS.....	XIII
<b>CHAPTER</b>	
<b>I INTRODUCTION .....</b>	<b>1</b>
1.1 Background and rationale .....	1
1.2 Research objectives.....	2
1.3 Research methodology.....	2
1.3.1 Literature review.....	2
1.3.2 Sample preparation .....	3
1.3.3 Triaxial shear test.....	4
1.3.4 Development of mathematical relations .....	4
1.3.5 Conclusions and thesis writing .....	5
1.4 Scopes and limitations .....	5
1.5 Thesis contents.....	5

## TABLE OF CONTENTS (Continued)

	<b>Page</b>
<b>II LITERATURE REVIEW .....</b>	<b>7</b>
2.1 Introduction.....	7
2.2 Joint shear strength criteria .....	7
2.3 Joint shear strength testing.....	14
2.4 Joint shear strength under confinement .....	17
2.5 Effect of temperature on joints .....	20
2.6 Effect of shear velocity .....	23
<b>III SAMPLE PREPARATION.....</b>	<b>35</b>
3.1 Introduction.....	35
3.2 Sample preparation .....	35
<b>IV LABORATORY TESTING.....</b>	<b>56</b>
4.1 Introduction.....	56
4.2 Triaxial shear test on tension-induced fractures and smooth saw-cut surface.....	56
4.3 Direct shear test on tension-induced fractures .....	60
<b>V TESTING RESULTS .....</b>	<b>63</b>
5.1 Triaxial shear test on tension-induced fractures .....	63
5.2 Triaxial shear tests on smooth saw-cut surfaces.....	83
5.3 Direct shear tests on tension-induced fractures .....	86

## TABLE OF CONTENTS (Continued)

	<b>Page</b>
<b>VI SHEAR STRENGTH CRITERIA</b> .....	89
6.1 Introduction .....	89
6.2 Normalization of shear displacement rate .....	89
6.3 Criterion for peak shear strength .....	90
6.4 Criterion for residual shear strength .....	96
6.5 Verification of the proposed criterion .....	101
<b>VII DISCUSSIONS, CONCLUSIONS AND</b>	
<b>RECOMMENDATIONS FOR FUTURE STUDIES</b> .....	104
7.1 Discussions .....	104
7.2 Conclusions .....	106
7.3 Recommendations for future studies .....	108
REFERENCES .....	112
BIOGRAPHY .....	119

## LIST OF TABLES

Table	Page
2.1 Test cases and boundary conditions .....	25
3.1 Summary of the mechanical properties for all rock types.....	38
3.2 Summary of granite sample dimensions of the tension-induced fractures.....	43
3.3 Summary of granite sample dimensions of the tension-induced fractures (continue).....	44
3.4 Summary of sandstone sample dimensions of the tension-induced fractures .....	45
3.5 Summary of sandstone sample dimensions of the tension-induced fractures (continue).....	46
3.6 Summary of marl sample dimensions of the tension-induced fractures.....	47
3.7 Summary of marl sample dimensions of the tension-induced fractures (continue).....	48
3.8 Summary of granite sample dimensions of the saw-cut surfaces.....	49
3.9 Summary of granite sample dimensions of the saw-cut surfaces.....	50
3.10 Summary of granite sample dimensions of the saw-cut surfaces.....	51
3.11 Sample dimensions of granite prepared for the direct shear tests.....	53
3.12 Sample dimensions of sandstone prepared for the direct shear tests.....	54
3.13 Sample dimensions of marl prepared for the direct shear tests.....	55
5.1 Summary of peak and residual shear strengths and their corresponding normal stresses for granite.....	69

## LIST OF TABLES (Continued)

Table	Page
5.2 Summary of peak and residual shear strengths and their corresponding normal stresses for sandstone.....	70
5.3 Summary of peak and residual shear strengths and their corresponding normal stresses for marl .....	71
5.4 Summary of peak shear strengths and their corresponding normal stresses for smooth saw-cut surfaces .....	84
5.5 Summary of peak and residual shear strengths and their corresponding normal stresses of direct shear tests .....	86
6.1 Summary of the normalize shear velocities.....	90
6.2 Empirical constants A, $\eta$ and $\kappa$ .....	92
6.3 Constants $\alpha$ , $\lambda$ , $\eta$ and $\kappa$ .....	93
6.4 Empirical constants $\alpha$ , $\lambda$ , $\eta$ and $\kappa$ .....	98

## LIST OF FIGURES

Figure	Page
1.1 Research methodology.....	3
2.1 Small triangular slab of rock used to derive the stress transformation equations.....	8
2.2 Plane of weakness with outward normal vector oriented at angle $\beta$ to the direction of maximum principal stress.....	9
2.3 Constant Normal Load (CNL) and Constant Normal Stiffness (CNS) joint shear tests.....	15
2.4 Shear behaviors of rough granite joints for the first two cycles.....	16
2.5 Shear ( $\tau$ ) and normal ( $\sigma_n$ ) stresses calculated from the applied axial stress ( $\sigma_1$ ) and lateral stress on the fracture plane ( $\sigma_o$ ).....	18
2.6 Peak shear strength ( $\tau$ ) as a function of normal stress ( $\sigma_n$ ) for various $\sigma_p$ .....	19
2.7 Comparison between test results and curves fit.....	22
2.8 Fracture mechanics models.....	23
2.9 Shear test results of J10 with normal stresses of 1, 2 and 4MPa, with shear velocity of 0.5 mm/min.....	26
2.10 The relation of residual shear stress and normal displacement with normal stress.....	27
2.11 Combined effect of velocity and state parameters on friction.....	28
2.12 Schematic diagram of apparatus.....	30

## LIST OF FIGURES (Continued)

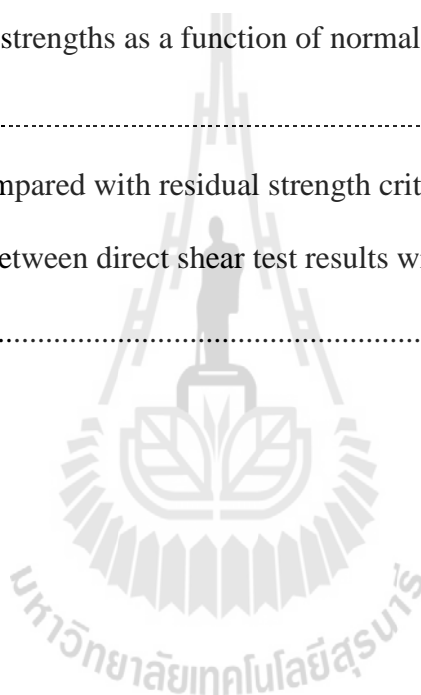
Figure	Page
2.13	The time-dependence of the coefficient of static friction for the sandstone.....31
2.14	Peak (left) and residual (right) shear strengths under various shear rates .....34
3.1	Area of rock tested in this study.....37
3.2	Some specimens for the three rock types.....39
3.3	Tension-induced fractures by line loading technique.....39
3.4	Some tension-induced fractures and their laser scanned images .....40
3.5	Examples of laser-scanned profiles to measure the maximum asperity amplitude to estimate the joint roughness coefficient (JRC).....41
3.6	Some specimens prepared for shear strength of saw-cut surfaces.....42
3.7	Some specimens prepared for direct shear tests.....52
4.1	Polyaxial load frame .....58
4.2	Directions of applied stresses with respect to the fracture orientation.....58
4.3	Direction relations of the fracture displacements.....60
4.4	Direct shear device used in this study.....61
4.5	Displacement dial gages used to measure the shear displacement and fracture dilation.....62
5.1	Shear stresses ( $\tau$ ) as a function of shear displacement ( $d_s$ ) for granite.....64
5.2	Shear stresses ( $\tau$ ) as a function of shear displacement ( $d_s$ ) for sandstone.....65
5.3	Shear stresses ( $\tau$ ) as a function of shear displacement ( $d_s$ ) for marl.....66

## LIST OF FIGURES (Continued)

Figure	Page
5.4 Major principle stress ( $\sigma_1$ ) as a function of the confining stress ( $\sigma_3$ ) under various shear velocities .....	68
5.5 Peak and residual shear stresses as a function of normal stress.....	72
5.6 Lateral-axial displacement ( $d_3-d_1$ ) curves of tension-induced fractures for granite.....	75
5.7 Lateral-axial displacement ( $d_3-d_1$ ) curves of tension-induced fractures for sandstone.....	76
5.8 Lateral-axial displacement ( $d_3-d_1$ ) curves of tension-induced fractures for marl.....	77
5.9 Normal displacement ( $d_n$ ) as a function of the shear displacement ( $d_s$ ) for granite.....	78
5.10 Normal displacement ( $d_n$ ) as a function of the shear displacement ( $d_s$ ) for granite.....	79
5.11 Normal displacement ( $d_n$ ) as a function of the shear displacement ( $d_s$ ) for granite.....	80
5.12 Some post-test fractures.....	82
5.13 Shear strengths of smooth saw-cut surfaces.....	85
5.14 Peak shear stresses as a function of normal stress.....	87
5.15 Some post-test fractures of sandstone for the direct shear tests.....	88

## LIST OF FIGURES (Continued)

<b>Figure</b>		<b>Page</b>
6.1	Major principal stresses at peak shear strength as a function of confining stresses results with the strength criterion.....	94
6.2	Peak shear strength criterion compared with test data.....	95
6.3	Residual shear strengths as a function of normal stress for various shear velocities.....	97
6.4	Test results compared with residual strength criterion.....	100
6.5	Comparisons between direct shear test results with the prediction by proposed equation.....	102



## SYMBOLS AND ABBREVIATIONS

$\sigma_1$	=	Major principal stress (axial stress)
$\sigma_{1, \text{peak}}$	=	Major principal stresses at peak
$\sigma_3$	=	Minor principal stress (lateral stress)
$\sigma_n$	=	Normal stress
$\sigma_{n, \text{peak}}$	=	Normal stress at peak
$\sigma_{n, \text{residual}}$	=	Normal stress at residual
$\tau$	=	Shear stress
$\tau_{\text{peak}}$	=	Shear stress at peak
$\tau_{\text{residual}}$	=	Shear stress at residual
$\sigma_1$	=	Maximum principal stress (axial stress)
$d_s$	=	Shear displacement
$d_n$	=	Normal displacement
$d_1$	=	Axial displacement (monitored in direction of $\sigma_1$ )
$d_3$	=	Lateral displacement (monitored in direction of $\sigma_3$ )
$\dot{d}_1$	=	Axial displacement rate
$\dot{d}_s$	=	Shear velocity
$\dot{d}_s^*$	=	Normalized shear velocity
$c$	=	Cohesion
$c^*$	=	Apparent cohesion

**SYMBOLS AND ABBREVIATIONS (Continued)**

$\phi$	=	Friction angle
$\phi^*$	=	Apparent friction angle
$\beta$	=	Angle between $\sigma_1$ and $\sigma_n$
$\theta$	=	Angle between $\sigma_1$ and fracture plane
A	=	Empirical constant
$\eta$	=	Empirical constant
$\kappa$	=	Empirical constant
$\alpha$	=	Empirical constant
$\lambda$	=	Empirical constant
$\mu$	=	$\tan\phi$
JRC	=	Joint roughness coefficient

# CHAPTER I

## INTRODUCTION

### 1.1 Background of problems and significance of the study

Understanding the nature behavior of rock mass is important in many geotechnical applications. The performance of engineering structures constructed in rock is concerned with the presence of fractures in rock when subjected to forces and displacements (Curran and Leong, 1983; Li et al., 2012). In rock masses, properties such as roughness, separation and joint aperture have considerable effects on shear strength of rock fractures. The shear behavior of rock fractures is usually estimated through direct shear tests (e.g., ASTM D5607-08) to determine the peak and residual strengths of the rock fractures. Its test configurations however pose some disadvantages that the magnitudes of the applied normal stress are limited by the uniaxial compressive strength of the rock and that the fractures are sheared under unconfined conditions. The triaxial shear testing (Brady and Brown, 2006; Jaeger et al., 2007) has been developed to simulate the frictional resistance of rock fractures under confinements. The normal stress at which the shear strengths are measured can be controlled by the applied axial stress and confining pressure.

The effect of shear velocity on rock fractures shear strength also plays an important role in the stability and safety assessment of the underground structures subjected to loading. Rapid loading or high shear velocity (seismic load and blasting) may impose different behavior to the shearing resistance of rock fractures, as

compared to the slow loading or low velocity of displacement (Crawford and Curran, 1981; Li et al., 2012; Chokchai, 2013). The shear velocity can also affect the shearing resistance of rock fractures, quantitative assessment of such effect has been rare.

## **1.2 Research objectives**

The objective of this study is to determine the effects of shear velocity on the shear strength of rock fractures under confinement. The effort involves performing triaxial shear tests on tension-induced fractures and smooth saw-cut surfaces by using a polyaxial load frame. The confining pressures vary from 1, 3, 7, 12 to 18 MPa. The axial stresses are applied under constant rates equivalent to the shear velocities on the fractures from  $1.15 \times 10^{-5}$  to  $1.15 \times 10^{-2}$  mm/s. Direct shear tests are also performed. Mathematical relationships between the shear velocity and the fractures shear strength are proposed to predict the shear strengths subject under various loading rates and confinements.

## **1.3 Research methodology**

This research consists of five main tasks; literature review, sample preparation, triaxial shear tests, development of mathematical relations, conclusions and discussions and thesis writing and presentation. The work plan is illustrated in the Figure 1.1.

### **1.3.1 Literature review**

Literature review has been carried out to study the previous researches on the effect of shear velocity on fracture shear strength under confinements. The sources of information are from text books, journals, technical reports and conference papers. A summary of the literature review has been given in the thesis.

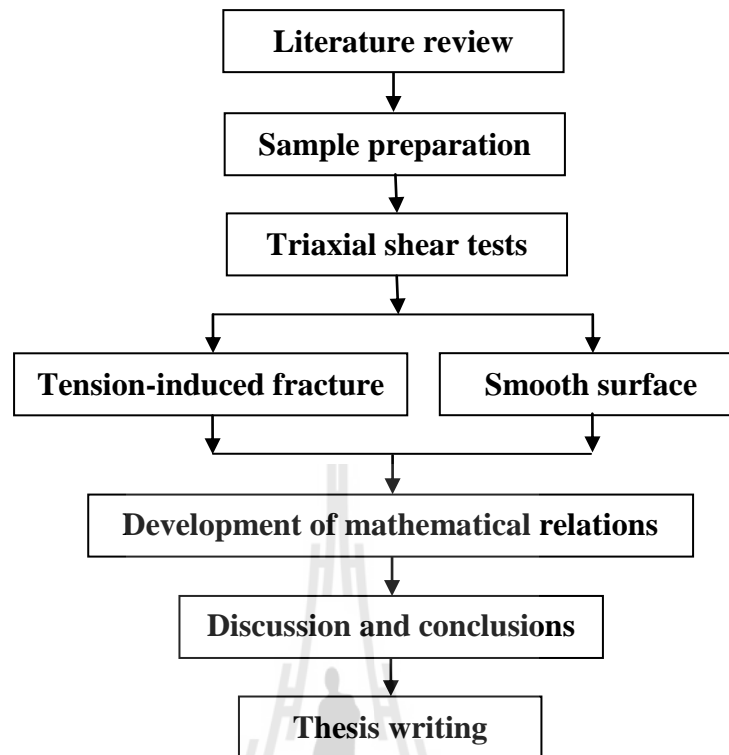


**Figure 1.1** Research methodology.

### 1.3.2 Sample preparation

The rock samples used in this study are Tak granite (Mahawat et al., 1990), Lopburi marl (Bunopas, 1992) and Phra Wihan sandstone (Boonsener and Sonpiron, 1997) which have been prepared to obtain rectangular block specimens with nominal dimensions of  $50 \times 50 \times 87 \text{ mm}^3$  and fracture surface with an area of  $50 \times 100 \text{ mm}^2$ . The fractures are artificially made in the laboratory by tension inducing method. The normal to the fracture plane makes an angle  $60^\circ$  with the axis of the specimens. All fractures are clean and well mated. The saw-cut surface specimens are used to form a complete pair of specimens primarily to avoid the effect of the groove caused by the cutting blade. Each block is cut diagonally and

hence obtaining the smooth fractures with the normal making an angle of  $60^\circ$  with the major axis of the specimen. All specimens are oven-dried before testing.

### **1.3.3 Triaxial shear tests**

The shear velocity tests has been performed to determine the rough fractures shear strength and develop sliding criteria of three rock types under confinements. Neoprene sheets are used to minimize the friction at all interfaces between the loading plate and the rock surface. A polyaxial load frame (Fuenkajorn and Kenkhunthod, 2010) is used to apply confining pressures from 1, 3, 7, 12 to 18 MPa. The axial displacement velocities are controlled constant at  $10^{-5}$ ,  $10^{-4}$ ,  $10^{-3}$  and  $10^{-1}$  mm/s. Before loading applied the specimen is under hydrostatic condition. The maximum principal stresses ( $\sigma_1$ ) are increased until peak shear stress occurs. Digital pressure gages measure oil pressure in the hydraulic cylinders that apply the normal and shear stresses to the rock specimens. The peak and residual shear strengths are recorded. The test is terminated when a total shear displacement of 8 mm is reached. After shearing the test fractures are examined and photographed.

### **1.3.4 Development of mathematical relations**

Results from laboratory measurements in terms of major principal stresses ( $\sigma_1$ ) corresponding to the peak shear strength as a function of shear displacement ( $d_s$ ), peak shear strength ( $\tau$ ) as a function of normal stress ( $\sigma_n$ ) and peak shear strength ( $\tau$ ) as a function of shearing velocity ( $\dot{d}_s$ ) for various confining pressures. The testing results have been used to develop relations between basic friction angle ( $\phi_b$ ), normal stress ( $\sigma_n$ ), joint roughness coefficients (JRC) and shear

stress ( $\tau$ ) for deriving a new failure criterion that can incorporate effect of shear velocity on joint shear strength under confinements.

### **1.3.5 Conclusions and thesis writing**

All study activities, methods, and results are documented and compiled in the thesis. The contents or findings are published in the conference, proceedings or journals.

## **1.4 Scope and limitations**

The scope and limitations of the research include as follows.

1. All Laboratory tests are performed on Tak granite, Lopburi marl and Phra Wihan sandstone specimens.
2. The applied axial displacement rates vary from  $10^{-5}$ ,  $10^{-4}$ ,  $10^{-3}$  to  $10^{-2}$  mm/s with the confining pressures varying from 1, 3, 7, 12 to 18 MPa.
3. All tests are performed using a polyaxial load frame.
4. All tested fractures are artificially made in the laboratory by tension-inducing methods.
5. The specimens are prepared with nominal dimensions of  $50 \times 50 \times 87$  mm<sup>3</sup> with the nominal fracture areas of  $50 \times 100$  mm<sup>2</sup>.
6. Up to 50 samples are tested for each rock type.
7. All tests are conducted under dry and ambient temperature.

## **1.5 Thesis contents**

This first chapter introduces the thesis by briefly describing the rationale and background. The second section identifying the research objectives. The third

section identifies the research methodology. The fourth section describes scope and limitations. The fifth section gives a chapter by chapter overview of the contents of this thesis.

The second chapter summarizes results of the literature review. Chapter three describes samples preparation. The laboratory tests are described in chapter four. The results of all tests and development of mathematical relations are presented in chapter five. Chapter six provides the conclusion and recommendations for future research studies.



## **CHAPTER II**

### **LITERATURE REVIEW**

#### **2.1 Introduction**

This chapter summarizes the results of literature review carried out to improve an understanding of the effects of shear velocity on rock fractures and new equations development. The topics reviewed here include fundamentals of joint shear strength criteria, joint shear strength testing, joint shear strength under confinement, effect of temperature on rock joints and effect of shear velocity.

#### **2.2 Joint shear strength criteria**

Jaeger et al. (2007) state that in order to derive the laws that govern the transformation of stress components under a rotation of the coordinate system, one should consider a small triangular element of rock, as shown in Figure 2.1. The following equations are obtained for the normal and shear stresses acting on a plane whose outward unit normal vector is rotated counter clockwise from the x direction by an angle  $\theta$ :

$$\sigma = \frac{1}{2} (\tau_{xx} + \tau_{yy}) + \frac{1}{2} (\tau_{xx} - \tau_{yy}) \cos 2\phi + \tau_{xy} \sin 2\phi \quad (1)$$

$$\tau = \frac{1}{2} (\tau_{yy} - \tau_{xx}) \sin 2\phi + \tau_{xy} \cos 2\phi \quad (2)$$

An interesting question to pose is whether or not there are planes on which the shear stress vanishes, and where the stress therefore has purely a normal component. The answer follows directly from setting  $\tau = 0$ , and solving for

$$\tan 2\phi = (2\tau_{xy}) / \tau_{yy} - \tau_{xx} \quad (3)$$

A simple graphical construction popularized by Mohr (1914) can be used to represent the state of stress at a point. Recall that equations (1) and (2) give expressions for the normal stress and shear stress acting on a plane whose unit normal direction is rotated from the  $x$  direction by a counterclockwise angle  $\theta$ . Imagine that the principal coordinate system is used, in which the shear stresses are zero and the normal stresses are the two principal normal stresses. In this case we replace  $\tau_{xx}$  with  $\sigma_1$ , replace  $\tau_{yy}$  with  $\sigma_2$ , replace  $\tau_{xy}$  with 0, and interpret  $\theta$  as the angle of counterclockwise rotation from the direction of the maximum principal stress.

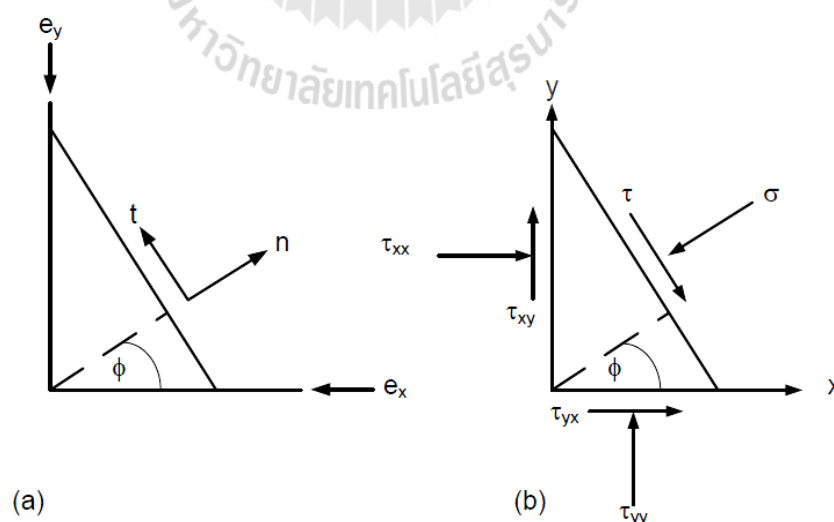


**Figure 2.1** Small triangular slab of rock used to derive the stress transformation equations (Jaeger et al., 2007).

The following equations give the normal and shear stresses on a plane whose outward unit normal vector is rotated by  $\theta$  from the first principal direction:

$$\sigma = \frac{(\sigma_1 + \sigma_2)}{2} + \frac{(\sigma_1 - \sigma_2)}{2} \cos 2\beta \quad (4)$$

$$\tau = \frac{(\sigma_1 - \sigma_2)}{2} \sin 2\beta \quad (5)$$

The rock has a pre-existing plane of weakness whose outward unit normal vector makes an angle  $\beta$  with the direction of the maximum principal stress,  $\sigma_1$  (Figure 2.2).

The Coulomb criterion for slippage to occur along this plane is assumed to be

$$|\tau| = S_o + \mu\sigma \quad (6)$$

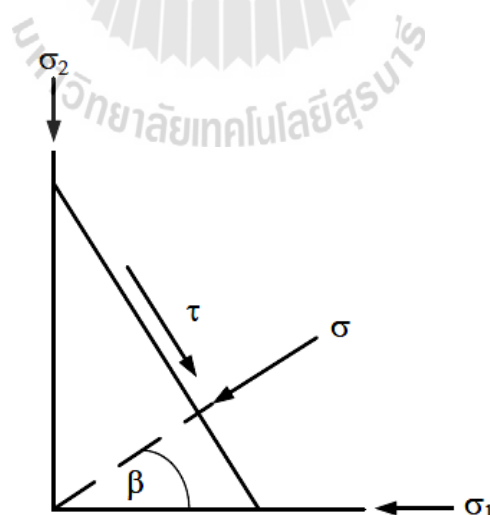


**Figure 2.2** Plane of weakness with outward normal vector oriented at angle  $\beta$  to the direction of maximum principal stress (Jaeger, et al., 2007).

where  $\sigma$  is the normal traction component acting along this plane,  $\tau$  is the shear component,  $S_o$  is called the cohesion of the surface, and  $\mu$  the coefficient of friction.

By equations (4) and (5),  $\sigma$  and  $\tau$  are given by

$$\sigma = \frac{1}{2} (\sigma_1 + \sigma_2) + \frac{1}{2} (\sigma_1 - \sigma_2) \cos 2\beta \quad (7)$$

$$\tau = -\frac{1}{2} (\sigma_1 - \sigma_2) \sin 2\beta \quad (8)$$

Shrivastava and Rao (2009) propose the criteria for the shear behavior of joint under constant normal load (CNL) condition. In the past several researchers have attempted to explain the shear strength of rock discontinuities under CNL boundary conditions. Linear failure criteria provided by Mohr-Coulomb:

$$\tau_f = c_a + \sigma_n \tan \phi_r \quad (9)$$

where  $\tau_f$  is maximum (peak) shear strength at failure,  $\sigma_n$  is stress normal to the shear plane (discontinuity),  $c_a$  is the apparent cohesion (shear strength intercept) derived from the asperities and  $\phi_r$  = the residual friction angle of the material comprising the asperities.

Bilinear failure criterion proposed by Patton (1966), offer a more realistic representation of the shear stress that can be developed along clean (unfilled) discontinuities. These criteria divide a typical curved envelope into two linear segments. The maximum shear strength that can be developed at failure is approximated by the following equations for low normal stress:

$$\tau_f = \sigma_n \tan \phi_u + i \quad (10)$$

where  $\phi_u$  is the basic friction angle on smooth planar sliding surface and  $i$  is angle of inclination of the first order (major) asperities.

It must be recognized that failure envelopes developed from shear tests on rock are generally curved. However, at high normal stress failure envelopes can be closely approximated by the linear Coulomb equation, equation (9).

Barton and Choubey (1977) propose empirical non-linear equation for peak shear strength of rough unfilled joints based on the results of direct shear tests performed on a wide variety of model tension fractures. The proposed equation for peak shear strength is as follows, which is sensitive both to variable joint roughness and compressive strength for the rock or joint walls:

$$\tau = \sigma_n \tan [JRC \log_{10} (JRC / \sigma_n) + \phi_b] \quad (11)$$

where  $\tau$  is shear strength at failure,  $\sigma_n$  is stress normal to the shear plane,  $\phi_b$  is the basic friction angle on smooth planar sliding surface, JRC is the joint roughness coefficient and JCS is the joint wall compressive strength.

Homand et al. (1999) propose three new peak shear stress criteria to predict the variation of shear strength with the normal stress for dilatant and non-dilatant rock joints under both constant normal stress and constant normal stiffness loading.

Most of the existing shear strength criteria in the literature are developed to predict the peak shear stress of initially mated and interlocked joints displaying some dilatant behavior. If the majority of these models into account some aspects of joint initial roughness (Ladanyi and Archambault, 1969; Jaegger, 1971; Barton, 1973;

Swan and Zongqi, 1985; Saeb, 1990), very few models take into account the effect of both surface anisotropy (Kulatilake et al., 1995) and progressive degradation of joint surfaces during the course of shearing (Homand-Etienne et al., 1999). In the present approach, authors suppose that there mainly exist two type of joint: (i) non-dilatant joints (isotropic surfaces) and (ii) dilatant joints (isotropic/ anisotropic surfaces).

The new peak shear stress criterion for non-dilatant joints exhibiting a high potential of degradation is given as follow:

$$\tau_p = \sigma_n \tan \left( \phi_r + \theta_s \left( 1 + \frac{\sigma_n}{\sigma_c} \left[ \frac{a_0}{u_s^0} \times \frac{2k_n}{DR_r^0} \times \log \left( \frac{u_s^{\max}}{a_0} \right) \right] \right) \right) \quad (12)$$

This peak shear stress criterion take into account surface angularity ( $\theta_s$ ), surface anisotropy isotropy ( $k_a$ ), strength of sample material ( $\sigma_c$ ), surface second-order roughness ( $DR_r^0$ ) and first-order roughness ( $a_0$ ) and finally, maximum cumulated shear displacement,  $u_s^{\max}$  (or number of cycles of shearing).

The new peak shear stress criterion for dilatant joints which includes the influence of dilatancy, asperities degradation and the number of cycles of shearing is given as follow:

$$\tau_p = \sigma_n \tan \left( \phi_b + 2\theta_s^n \exp \left( -\frac{\sigma_n}{\sigma_c} \times \frac{u_t^0}{a_0} \left[ \frac{u_s^0}{u_t^{\max}} + \left( \frac{2(k_a)^2}{3 DR_r^0} \right) \right] \right) \right) \quad (13)$$

The generalized shear strength criterion can be derived for both constant normal stress and constant normal stiffness loading is given as follow:

$$\tau_p|_{\text{CNS,CNK}} = \sigma_{ni} \tan(\phi_b + i_d) + K_n (u_t^0 \times \tan(i_p)) \tan(\phi_b + i_d) \quad (14)$$

where  $i_d$  is consequently angle and  $i_p = i_{p\_CNK}$ . It was found from our experimental investigations that for a give  $\sigma_{ni}$ , peak dilatancy angle observed for the constant normal stress loading ( $i_{p\_CNS}$ ) is always greater than the peak dilatancy angle for the constant normal stiffness loading ( $i_{p\_CNK}$ ) due to the effect of the normal stiffness  $K_n$ . The constant normal stiffness peak dilatancy angle can be predicted by the following relationship:

$$i_{p\_CNK} = \theta_s^0 \exp\left(-\frac{(k_a)^2}{DR_r^0} \times \frac{K_n u_s^0}{\sigma_{ni} + \sigma_c}\right) \quad (15)$$

Grasselli and Egger (2003) propose a new constitutive criterion, relating stress and displacements, is proposed to model the shear resistance of joints under constant normal load conditions. It is based on an empirical description of the surface, and on the results from more than 50 constant normal-load direct-shear tests performed on replicas of tensile joints and on induced tensile fractures for seven rock types. This constitutive model is able to describe experimental shear tests conducted in the laboratory. Moreover, the parameters required in the model can be easily measured through standard laboratory tests. The proposed criterion was also used to estimate the joint roughness coefficient (JRC) value. The predicting values were successfully correlated with JRC values obtained by back analysis of shear tests.

Babanouri et al. (2011) state that although many researchers have studied the normal and shear behavior of fractures under stresses, the over-consolidation effect on the slip/shear behavior of discontinuities has not been considered. The over -

consolidation behavior of non-planar rock fractures should be considered when deposition-consolidation-erosion (or excavation) sequences occur. Plaster replicas of representative natural rock joint surfaces were prepared for this study. In this case, the surface roughness and other geometrical properties remain constant during the laboratory direct shear tests. It was observed that the shear strength within a large range of roughness, joint wall strength and normal stress values significantly increases with increasing over-consolidation ratio. According to the test results, a new model is developed as an extended form of Barton's shear failure criterion for rock joints. This model considers the effect of various paths of normal loading/unloading before shearing and over-consolidation ratio (OCR) in a fracture. A new joint over-closure (JOC) parameter is also introduced as the ratio of closure in over- closed to normally closed conditions.

### **2.3 Joint shear strength testing**

Understanding the shear behavior of rock discontinuities is critical for understanding mechanical behavior of rock mass, because the shear movement of rock mass occurs mainly along the discontinuities such as faults, joints and fissures. Direct shear tests on the rock discontinuities can be divided into two types: 1). Constant normal load (CNL) direct shear test, where the normal load on the discontinuity remains constant during the shear test, and 2). Constant normal stiffness (CNS) direct shear test, where the normal load varies according to the normal dilation. The CNL direct shear test can be applied to predict the shear behavior of a rock slope, where the normal load on the discontinuities is relatively small and constant. The CNL direct shear test, however, has been used also for many

underground rock joint shear tests, just because of neglect of the difference between rock slope and underground, or because CNL test equipment is simpler and easier to set up than CNS test equipment (Rim, et al., 2005; Morris, 2003). Figure 2.3 shows schematically two general types of shear test.

Olsson and Barton (2001) obtained cores of granite drilled parallel to a joint plane in a naturally occurring joint rock mass. They performed shear tests under both constant normal load (CNL) and constant normal stiffness (CNS). They provide shear stress versus shear displacement and normal displacement versus shear displacement data.

Obert et al. (1976) considered intact, induced-fractured and sawed samples of granite and sandstone. Tests were performed under variable constant normal stiffness (CNS). The results provided are somewhat limited however, with only detailed shear stress versus normal displacement results for two tests and peak shear versus peak normal stress for all tests.

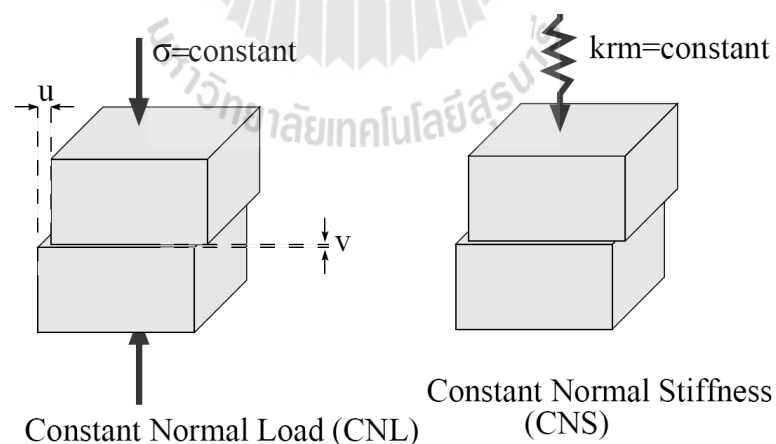


**Figure 2.3** Constant Normal Load (CNL) and Constant Normal Stiffness (CNS) joint shear tests (Morris, 2003).

Lee et al. (2001) obtained measurements of dilation under CNL for multiple cycles of shear loading. Figure 2.4 shows results for cyclic loading of rough granite joints. Consistent with the results obtained by Olsson and Barton (2001), Lee et al. (2001) found that the majority of the observed dilation occurs after the initial peak shear stress is reached. The same type of behavior (without the initial peak shear stress) is observed upon sufficient shear in the opposite direction and for subsequent cycles of shear loading. In addition, the joint exhibits little dilation upon initial shear loading. Dilation becomes significant as the joint approaches peak shear stress. Similar tests and conclusions have also been obtained by Kamonphet and Fuenkajorn (2013)

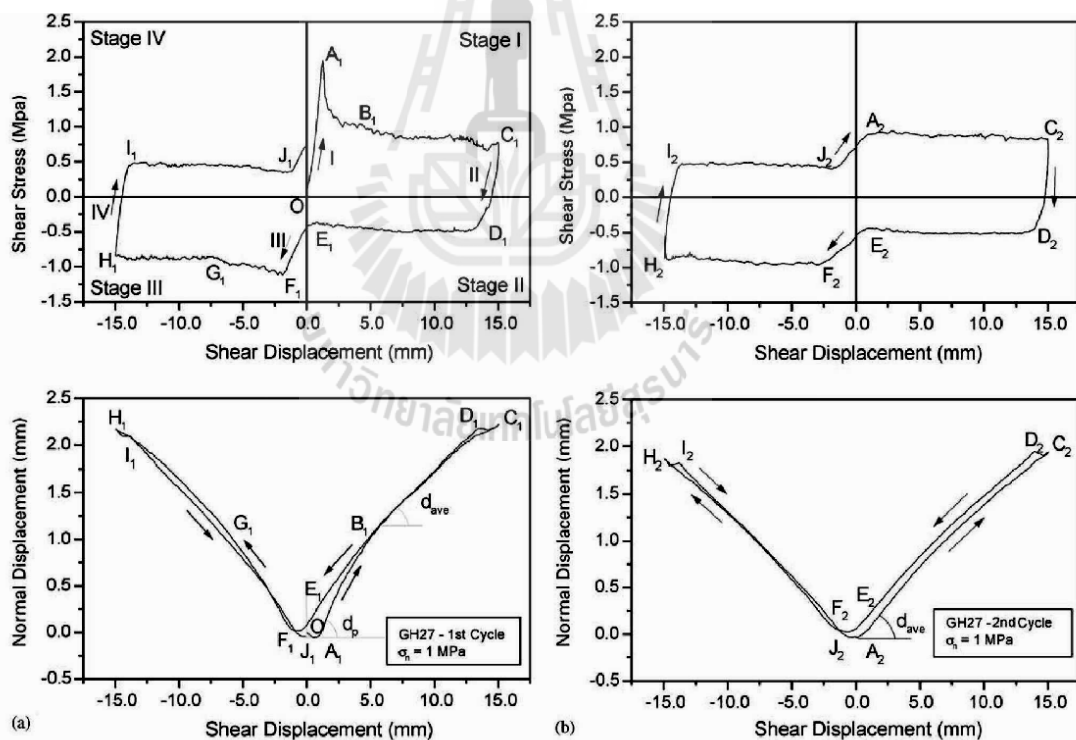


**Figure 2.4** Shear behaviors of rough granite joints for the first two cycles: (a) first cycle and (b) second cycle (Lee et al., 2001).

## 2.4 Joint shear strength under confinement

Kapang et al. (2013) perform the true triaxial shear tests to determine the peak shear strengths of tension-induced fractures in three Thai sandstones. The specimens used for the true triaxial shear tests are prepared from the Phu Kradung, Phu Phan and Phra Wihan sandstones (hereafter designated as PKSS, PPSS and PWSS). They are cut to obtain rectangular blocks with nominal dimensions of 76 x 76 x 126 mm<sup>3</sup>. The normal to the fracture plane makes an angle of 59.1° with the axial (major principal) stress. Dead weights are placed on the two lower bars to obtain the pre-defined magnitude of the lateral stresses ( $\sigma_o$  and  $\sigma_p$ ) on the specimen. Simultaneously the axial (vertical) stress is increased to the same value with so to obtain the condition where both shear and normal stresses are zero on the fracture plane. This is set as an initial stress condition. The test is started by increasing the axial stress at a constant rate using the electric oil pump while  $\sigma_p$  and  $\sigma_o$  are maintained constant. The specimen deformations in the three loading directions are monitored. The readings are recorded every 10 kN of the axial load increment until the peak shear stress is reached. Figure 2.5 shows the directions of the applied stresses with respect to the fracture orientation.

Four test series are performed: (1) true triaxial shear tests of tension-induced fractures under constant  $\sigma_p/\sigma_o$  ratio, (2) true triaxial shear tests of tension-induced fractures under constant  $\sigma_p$ , (3) true triaxial shear tests of smooth surfaces under constant  $\sigma_p$ , and (4) direct shear tests of tension-induced fractures.

The peak shear strengths are determined for lateral stress ratios ( $\sigma_p/\sigma_o$ ) of 0, 0.5, 1, 2, 3 and 4. The conditions where  $\sigma_p/\sigma_o$  is 0 and 1 are equivalent to the direct

shear testing and the triaxial shear testing, respectively. The configurations of the sandstone specimens and test procedure for this test series are identical to those mentioned above. Here  $\sigma_p$  is maintained constant at 1, 2 or 3 MPa while  $\sigma_o$  is varied from 1.5 to 6 MPa. The results are presented in the forms of  $\tau$ - $\sigma_n$  diagrams in Figure 2.6. For a comparison the true triaxial testing results at  $\sigma_p = 0$  are also incorporated into the figure. It is found that the lateral stress  $\sigma_p$  can notably decrease the fracture shear strengths.

From the results of this study it can be concluded that the lateral stress ( $\sigma_p$ ) parallel to the sliding plane and perpendicular to the sliding direction can significantly reduce the cohesion and friction angle of the fractures. The greater magnitudes of the lateral stress  $\sigma_p$  result in larger sheared off areas and larger dilations. In general the decrease of the fracture cohesion with increasing confining pressures (for the case of lateral stress ratio  $\sigma_p/\sigma_o = 1$ ) as observed here agrees reasonably well with the

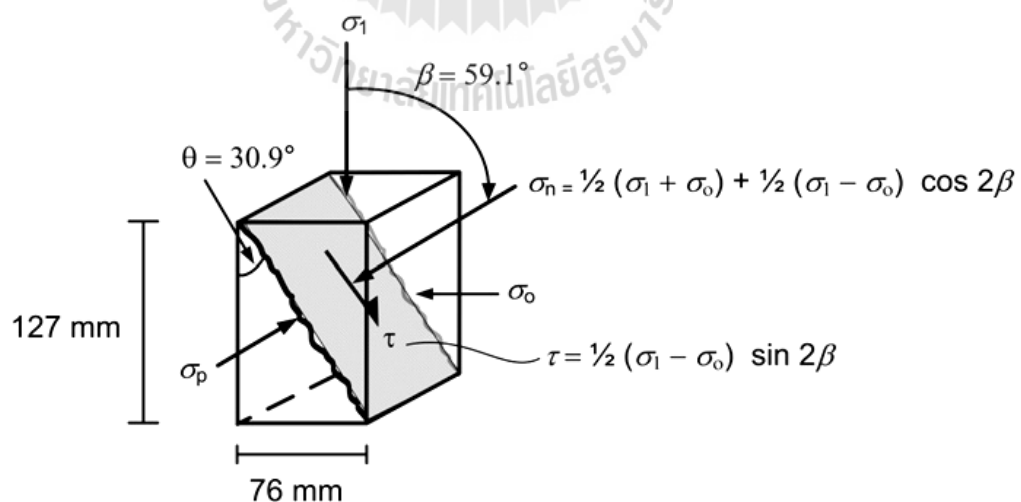


**Figure 2.5** Shear ( $\tau$ ) and normal ( $\sigma_n$ ) stresses calculated from the applied axial stress ( $\sigma_1$ ) and lateral stress on the fracture plane ( $\sigma_o$ ) (Kapang et al., 2013).

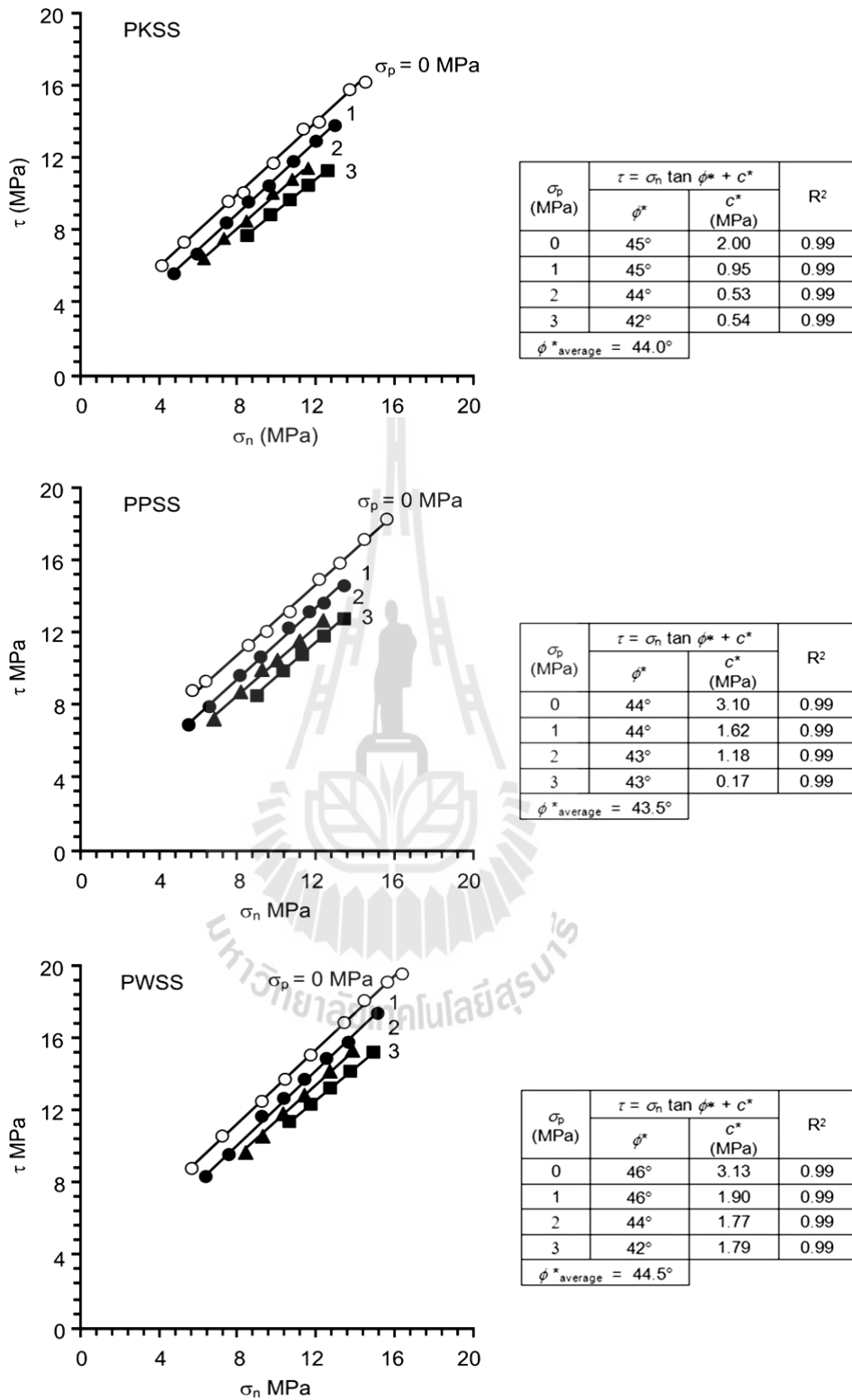


**Figure 2.6** Peak shear strength ( $\tau$ ) as a function of normal stress ( $\sigma_n$ ) for various  $\sigma_p$

(Kapang et al., 2013).

experimental results obtained by Ramamurthy and Arora (1994). This means that the fracture shear strengths from the (unconfined) direct shear testing may not truly represent the fault or fracture shear strengths under the multi-axial stresses of in-situ conditions.

## **2.5 Effect of temperature on joints**

Mitchell et al. (2013) state that temperature is believed to have an important control on frictional properties of rocks, yet the amount of experimental observations of time-dependent rock friction at high temperatures is rather limited. They investigated frictional healing of Westerly granite in a series of slide-hold-slide experiments using a direct shear apparatus at ambient temperatures between 20°C and 550°C. They observe that at room temperature coefficient of friction increases in proportion to the logarithm of hold time at a rate consistent with findings of previous studies. For a given hold time, the coefficient of friction linearly increases with temperature, but temperature has little effect on the rate of change in static friction with hold time. They used a numerical model to investigate whether time-dependent increases in real contact area between rough surfaces could account for the observed frictional healing. The model incorporates fractal geometry and temperature-dependent viscoelastoplastic rheology. They explored several candidate rheologies that have been proposed for steady state creep of rocks at high stresses and temperatures. None of the tested laws could provide an agreement between the observed and modeled healing behavior given material properties reported in the bulk creep experiments. An acceptable fit to the experimental data could be achieved with modified parameters. In particular, for the power-law rheology to provide a

reasonable fit to the data, the stress exponent needs to be greater than 40. Alternative mechanisms include time-dependent gouge compaction and increases in bond strength between contacting asperities.

Stesky (1978) studies the mechanical properties of faulted and jointed rock under pressure and temperature and in the presence of water. At low effective confining pressures (below about 1 kilobar), the friction strength is quite variable and depends on the frictional resistance between gouge particles or asperities and on the dilatancy of the fault. At higher pressures the friction strength is nearly independent of mineralogy, temperature, and rate, at least for rocks whose friction strength is less than the failure strength. Water tends to slightly weaken the fault. The type of sliding motion, whether stick-slip or stable sliding, is much more affected by environmental and mineralogical factors. In general, stick-slip is dominant at high pressures and low temperatures, in the presence of strong minerals such as quartz and feldspar, in the absence of gouge, for lower surface roughness, and perhaps in the presence of water. The microscopic deformation mechanisms are poorly understood. At low temperatures, cataclasis dominates in rocks containing mostly quartz or feldspar, and plastic deformation in rocks containing mostly calcite or platy silicates. At high temperature most minerals deform plastically, producing a greater temperature and rate-dependence of the friction strength. Glass has been found in some sliding surfaces in sandstone.

Naphudsa et al. (2013) perform the triaxial shear tests to experimentally determine the shear strength of fractures in granite under elevated temperatures. Triaxial shear tests are performed using a polyaxial load frame. The specimens are prepared from Tak granite with nominal dimensions of  $5.0 \times 5.0 \times 8.7 \text{ cm}^3$  and the

fracture area of  $5 \times 10 \text{ cm}^2$ . The normal of fracture plane makes an angle of  $60^\circ$  with the axial (major principal) stress. The testing is subjected to constant temperatures ranging from 303 (ambient temperature), 373, 573 to 773 Kelvin with confining stresses from 1, 3, 7, 12 to 18 MPa.

The results indicate that the shear strength decreases with increasing temperature, which can be best described by an empirical equation:

$$\tau = \alpha \cdot \sigma_n^b \cdot \exp(-\lambda/T) \quad (16)$$

where  $\alpha$ ,  $\beta$ ,  $\lambda$  are empirical constants. Regression analysis on the test data using SPSS statistical software (Wendai, 2000) these parameters are defined as:  $\alpha = 2.02$ ,  $\beta = 0.79$ , and  $\lambda = -199.1$ . Figure 2.7 compares the test data with the curves fit of the proposed equation. This equation can be used to predict shear strength of fractures granite under elevated temperatures.

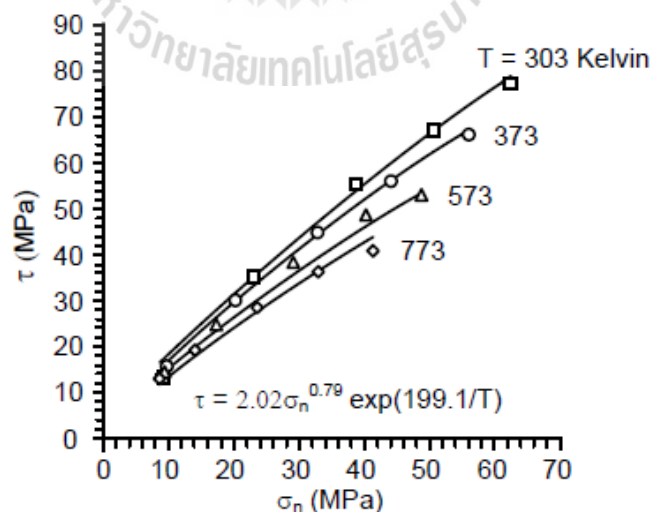


**Figure 2.7** Comparison between tests results (point) and curves fit (lines) (Naphudsra et al., 2013).

## 2.6 Effect of shear velocity

Kemeny (2003) propose a fracture mechanics model is developed to illustrate the importance of time-dependence for brittle fractured rock. In particular a model is developed for the time dependent degradation of rock joint cohesion. Degradation of joint cohesion is modeled as the time-dependent breaking of intact patches or rock bridges along the joint surface. A fracture mechanics model is developed utilizing subcritical crack growth, which results in a closed-form solution for joint cohesion as a function of time. A simple fracture mechanics model for the rock bridge is shown in Figure 2.8.

In this paper a model was developed for the time-dependent degradation of rock joint cohesion. Degradation of joint cohesion was modeled as the time-dependent breaking of intact patches or rock bridges along the joint surface. A fracture mechanics model was developed utilizing subcritical crack growth, which

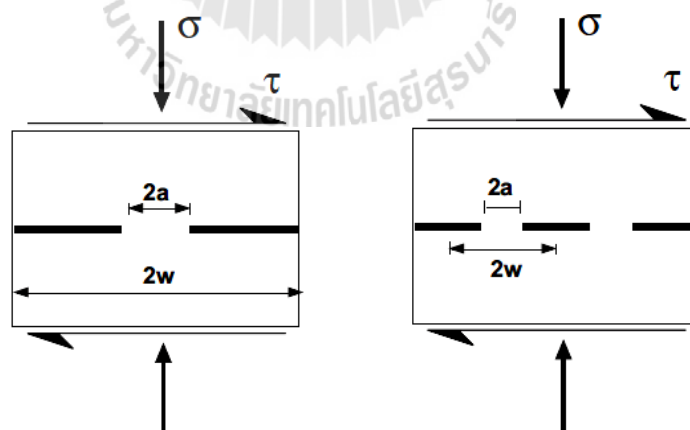


**Figure 2.8** Fracture mechanics models, a) single rock bridge under far field normal and shear stresses, b) multiple rock bridges under far field normal and shear stresses (Kemeny, 2003).

results in a closed-form solution for joint cohesion as a function of time. As an example, a rock block subjected to plane sliding was analyzed. The cohesion was found to continually decrease, at first slowly and then more rapidly. At a particular value of time the cohesion reduced to value that resulted in slope instability. A second example was given where a variation in some of the material parameters was assumed. A probabilistic slope analysis was conducted, and the probability of failure as a function of time was predicted. The probability of failure was found to increase with time, from an initial value of 5% to a value at 100 years of over 40%. These examples show the importance of being able to predict the time-dependent behavior of a rock mass containing discontinuities, even for relatively short-term rock structures. In the future some actual field case studies using the model will be conducted, to evaluate the usefulness of the simple model for actual engineering design.

Li et al. (2012) perform the repeated shear tests on artificial rock fracture samples conducted with shear velocities ranging from 0.5 mm/min to 50 mm/min to estimate the effects of surface roughness, shear velocity and shear history on the shear behavior of rock fractures. A servo-controlled direct shear apparatus for rock fractures using virtual instrument (VI) software was used in this study (Jiang et al. 2004). The rock fracture sample used in this study, labeled as J10, was created by splitting a granite block, and was used as prototype to produce artificial replicas of rock fractures. The samples (replicas) are 100 mm in width, 200 mm in length and 100mm in height, and are made of mixtures of plaster, water and retardant with weight ratios of 1:0.2:0.005. The experimental cases (15 cases in total) are summarized in Table 1. The tests were conducted under CNL boundary conditions

**Table 2.1** Test cases and boundary conditions.

Sample	Shear velocity (mm/min)	Boundary condition	
		Normal stresses $\delta_n$ (MPa)	Normal stiffness $k_n$ (GPa/m)
J10	0.5→5→10→20→50		
	5→10→20→50	1.0	0
	10→20→50	2.0	0
	20→50	4.0	0
	50		

with different normal stresses, so as to obtain the mechanical properties of rock fracture like cohesion and friction angle. The shear test results under normal stresses of 1, 2 & 4MPa, with shear velocity of 0.5 mm/min are shown in Figure 9. During the CNL tests, the normal stress is maintained constant, consequently, the shear stress firstly increases linearly to reach a maximum (shear strength) and then decreases to the residual strength. The slope of the increasing portion of the curve is the shear stiffness  $k_s$  of the fracture. The peak shear stress increases proportionally with the normal stress (Figure. 2.9a). As shown in Figure 2.9b, the normal displacement increases fast in the initial stage of shear, then continues to increase but with smaller gradient. The dilation of fracture is restricted under larger  $\delta_n$  stress.

The repeated shear results of the 3 cases sheared with 5 kinds of shear velocities, under normal stresses of 1, 2 and 4MPa, the residual normal stress and residual normal displacement were obtained as shown in Figure 2.10. The peak shear stress has no obvious relation with the shear velocity due to the complex failure mode of the major asperities. In the residual stage, the shear stress increases and the normal displacement decreases proportionally with the increase of shear velocity. The cohesion only exists in the first shear loop, and trends to 0 in the later loops. In a

repeated shear, the friction angle increases with the shear velocity in the first few loops, then the friction angle trends to a constant value.

Singh et al. (2011) study the influence of shear velocity on frictional characteristics of rock surface. Strain-rate dependence on friction is investigated in relation to sliding behavior under normal load. The phenomenon of stick-slip of granite and shaly sandstone with a tribometer at constant rate of strain under normal loads was observed.

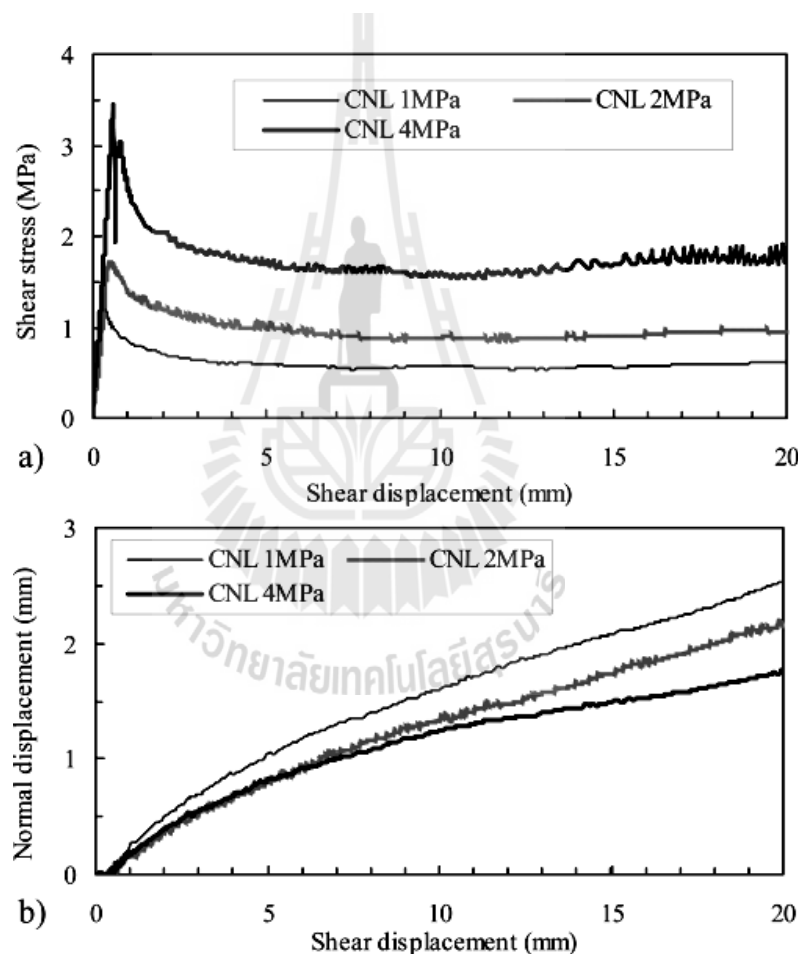


**Figure 2.9** Shear test results of J10 with normal stresses of 1, 2 and 4MPa, with shear velocity of 0.5 mm/min. a) Shear stress vs. shear displacement; b) Normal displacement vs. shear displacement (Li et al., 2012).

The friction value is governed by two factors, i.e., shear velocity and the state parameters such as grain size, roughness, cohesive strength, nature and thickness of gouge present between the sliding surfaces. The friction may also decrease and is called the velocity

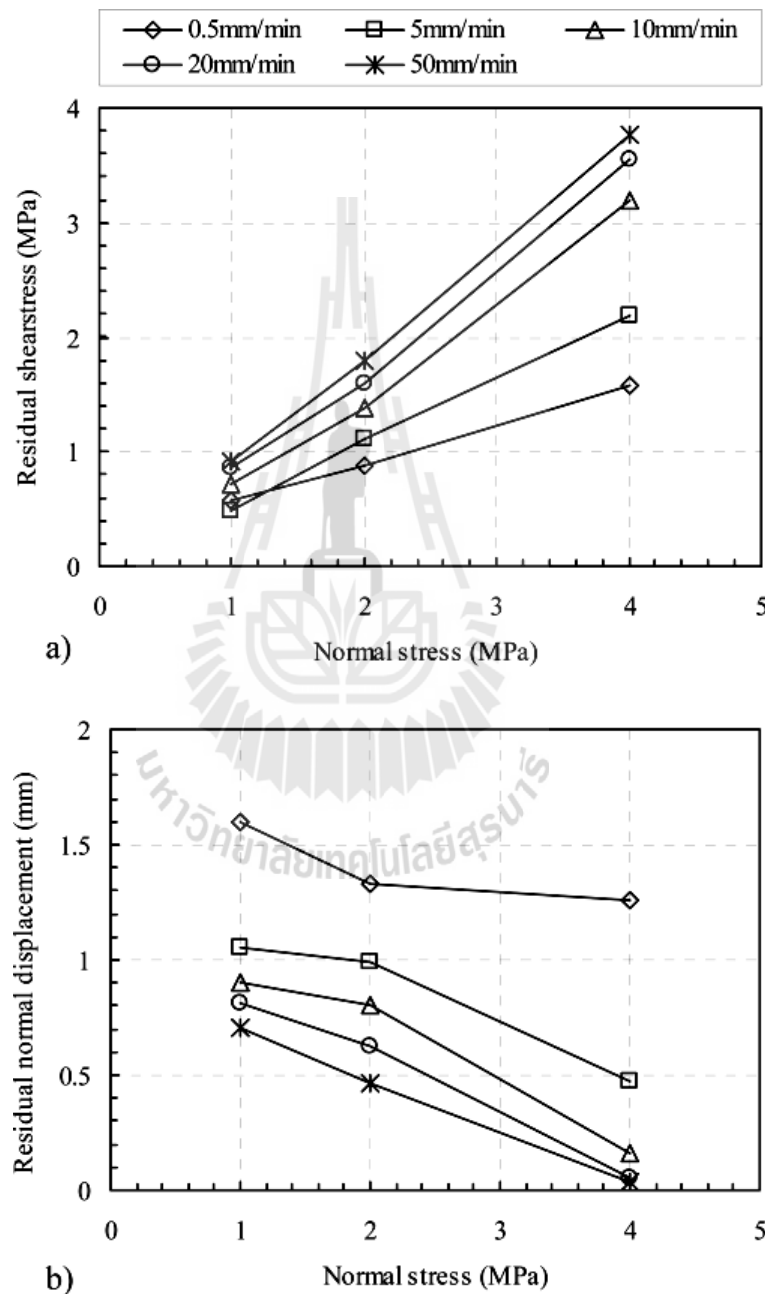


**Figure 2.10** a) The relation of residual shear stress with normal stress; b) The relation of residual normal displacement with normal stress (Li et al., 2012).



$\theta$  the 'state' variables,  $D_c$  the critical slip distance and  $V_0$  the initial displacement rate (m/s).

Friction at the interface of the rock samples was developed by increasing shear strain at a constant rate by applying constant velocity using the tribometer. For shaly sandstone, state parameters (a and b) played a major role in determining the friction values and roughness of the contact surfaces as well. Higher values of b for shaly sandstone may be attributed to the fact that its surface had a greater number of pronounced asperities. Rubbing between the surfaces does not mean that surface becomes smoother. This is because of variation of friction between surfaces.

Rong-Qiang and Shao-Xian (2006) studies the effects of the temperature and strain rate on the brittle fracture strength for rocks in the lithosphere. The effects of the confining pressure, size of the rock sample, temperature and strain rate are taken into account in the new formula. The empirical formula can be used in the study of the rheological structure of the lithosphere. It can be found that the rheological strength decreases obviously when the new empirical formula is used because the temperature and strain rate effect is taken into account. However, it should be pointed out that the strain rate in the experiment is in the range  $10^{-7} \text{ s}^{-1}$  to  $10^{-2} \text{ s}^{-1}$ , while the strain rate in the lithosphere can reach  $10^{-16} \text{ s}^{-1}$ . The empirical formula for fracture strength of rocks in the lithosphere can be written as:

$$(\sigma_1 - \sigma_3)_b = B_0 \left[ 1 + K \left( \frac{\sigma_c}{B_0} \right) \right]^n \left[ 1 + \alpha \left( \log \frac{T}{T_0} \right)^\beta \right] \left[ 1 + \gamma \log \left( \frac{\dot{\varepsilon}}{\varepsilon_0} \right) \right] \quad (18)$$

where  $B_0$  is the uniaxial compressive strength of rocks (meter scale),  $\sigma_c$  is the confining pressure  $T_0$  is the room temperature,  $T$  is the temperature,  $\dot{\epsilon}$  is the strain rate,  $\dot{\epsilon}_0$  is the reference strain rate ( $10^{-5}\text{s}^{-1}$ ) and  $K$ ,  $n$ ,  $\beta$ ,  $\gamma$  and  $\alpha$  are dimensionless constants.

Dieterich (1972) studies the time-dependent friction in rock on porous sandstone, quartzite, greywacke, and granite in the 20- to 850-bar normal stress range. Figure 2.12 schematically illustrates the apparatus. This apparatus is similar to but somewhat smaller than the direct shear apparatus. With this apparatus an inner block with planar and parallel faces is pushed between two outer blocks. The blocks have dimensions of up to  $6.0 \times 6.0$  cm and a thickness of 1.5 cm. Figure 2.13 shows the variation of the coefficient of static friction with the duration of stick on surfaces with gouge for the sandstone. Similar results were obtained for the quartzite, greywacke, and granite. The coefficient of static friction of surfaces with gouge exhibits a highly

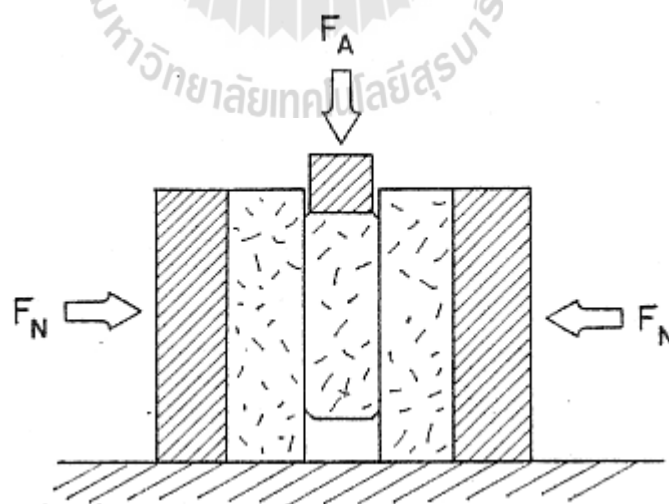


**Figure 2.12** Schematic diagram of apparatus (Dieterich, J.H., 1972).

time-dependence behavior. This behavior may be significant in understanding the mechanisms of earthquake foreshocks, aftershocks, and fault creep.

Curran and Leong (1983) propose the rate-dependent behavior of rock joints by a dynamic direct shear machine. A test black quartz syenite specimen consists of two blocks. The size of the upper surface was either  $200 \times 200$  mm and the lower

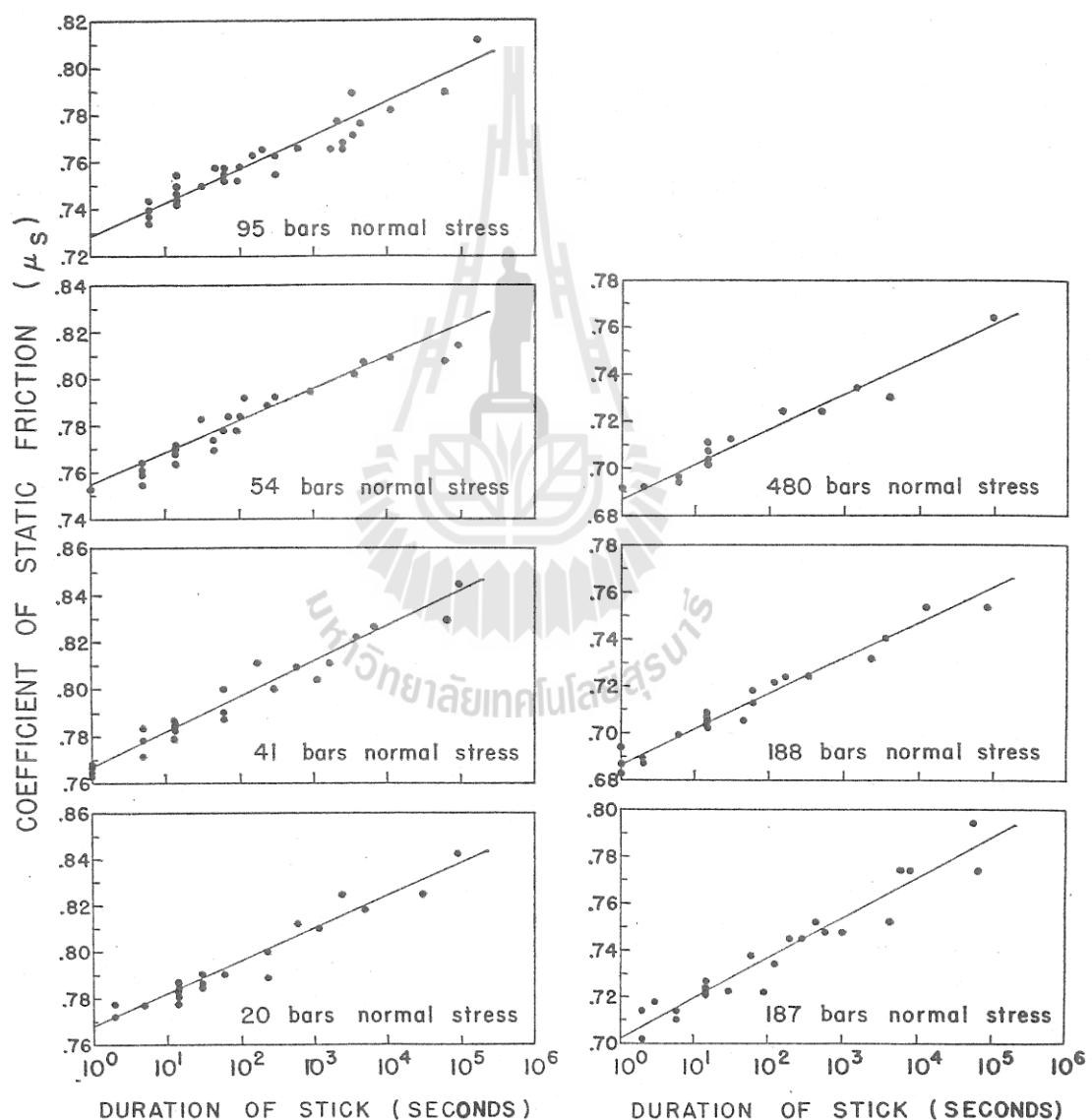


**Figure 2.13** The time-dependence of the coefficient of static friction for the sandstone

(Dieterich, J.H., 1972).

surface was  $310 \times 210$  mm. Two servo-controlled actuators, each with a force capacity of 250 kN and a maximum stroke of 250 mm, react against a braced portal frame to provide the loading in the normal and shear directions. The experiments consistently showed that the frictional resistance is dependent on the slip velocity. This rate-dependency was observed within a certain rate of shear velocities below and above which the frictional resistance was essentially independent of the rate of shear displacement.

ASTM (D5607-08) specifies the performing of the direct shear strength tests on rock specimens in laboratory. It includes procedures for both intact rock strength and sliding friction tests which can be performed on specimens that are homogeneous, or have planes of weakness, including natural or artificial discontinuities. Examples of an artificial discontinuity include a rock-concrete interface or a lift line from a concrete pour. Only one discontinuity per specimen can be tested. The height of specimen shall be greater than the thickness of the shear (test) zone and sufficient to embed the specimen in the holding rings. Specimens may have any shape such that the cross-sectional areas can be readily determined. In most cases the least cross-sectional dimension of the specimen should be at least 10 times the largest grain size in the specimen. The test plane should have a minimum area of  $1900 \text{ mm}^2$  ( $3 \text{ in}^2$ ).

Direct shear test can be performed by loading device to apply and register normal and shear forces on the specimens. It must have adequate capability to apply the shear force at a rate conforming to the specified requirements. Apply a small seating normal load on the order of 450 to 900 N (100 to 200 lb), depending on specimen size. Account for the mass of the normal load system when placing a specified normal stress on the specimen. After the selected normal load has been

stabilized, apply the shear load continuously at the selected rate of shear displacement. A minimum of 10 sets of readings is suggested to be taken before reaching the peak shear strength. After reaching the peak shear strength, loading should continue and readings taken until a residual shear strength is established. Measurements of normal displacements by measure normal displacements with the four vertical displacement measuring devices at each shear load observation. Compare the four readings and determine possible specimen rotation which would be indicated by differences in the readings of the four devices. Measurements of shear displacements by measure and record shear displacement at suitable intervals, that is, 0.025 or 0.05 mm (0.001 or 0.002 in.), with the horizontal displacement measuring device mounted on the shear box. For the direct shear strength tests under the controlled displacement rate, the ISRM suggested method (Muralha et al., 2013) specifies the rate of shear displacement of the shear strength tests on rock fracture specimens in laboratory around 0.1–0.2 mm/minute ( $2.5 \times 10^{-3}$  mm/s) which are usually suitable for most conditions.

Chokchai and Fuenkajorn (2013) perform the direct shear tests to experimentally determine the effects of loading rate on shearing resistance of tension-induced fracture in sandstone specimens. The applied shear stresses are controlled at constant rates of 0.00002, 0.0002, 0.002, 0.02 and 0.2 MPa/s. The normal stresses are varied from 0.2, 1, 2, 3 to 4 MPa. The results indicate that for all sandstone types the peak and residual shear strengths and joint shear stiffness increase exponentially with loading rate, particularly under high normal stresses. The shear rate has no effect on the basic friction angle of the smooth saw-cut surfaces. An empirical relation has

been developed to represent the shear strengths of the rough fractures under various loading rates, which can be best described by an empirical equation:

$$\tau = [ X \cdot \ln(\delta\tau/\delta t) + Y ] + \sigma_n \tan [ Z \cdot \ln(\delta\tau/\delta t) + B ] \quad (19)$$

where X, Y, Z and B are empirical constants.  $\delta\tau/\delta t$  is shear rates. Figure 2.14 compares the test data with the curves fit of the proposed equation. This equation can be used to predict the shear strengths of fractures under various loading rates and normal stresses.

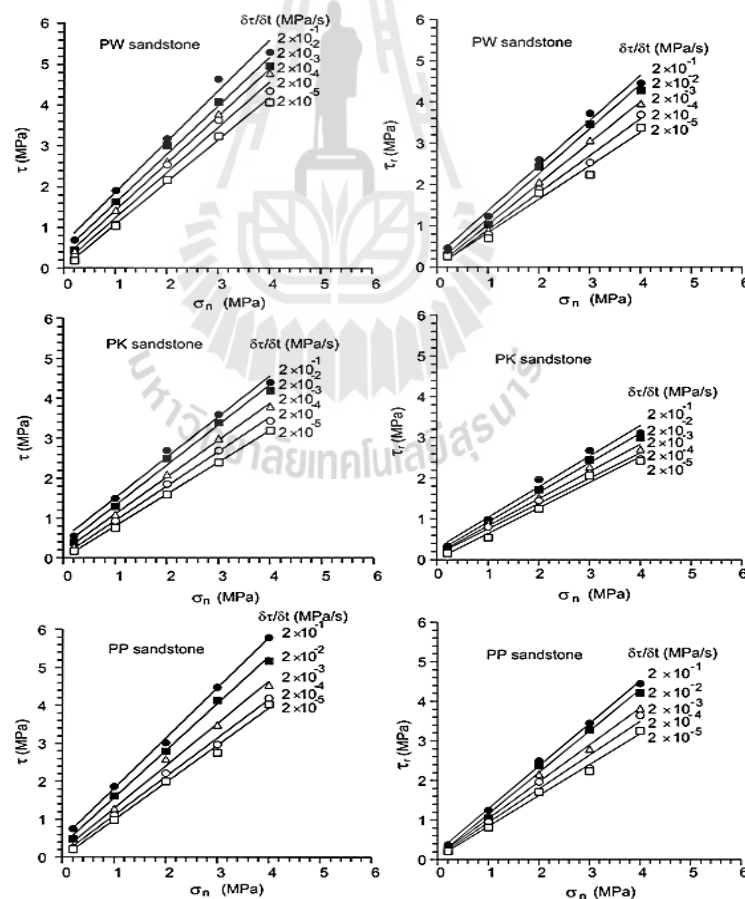


**Figure 2.14** Peak (left) and residual (right) shear strengths under various shear rates (Chokchai and Fuenkajorn, 2013).

# **CHAPTER III**

## **SAMPLE PREPARATION**

### **3.1 Introduction**

This chapter describes the sample preparation and specifications for 1) the triaxial shear tests on tension-induced fracture and smooth saw-cut surface 2) direct shear tests on tension-induced fractures. The sources rock types used to prepare the sample are also identified.

### **3.2 Sample preparation**

The specimens used for the triaxial shear tests and direct shear tests are prepared from the Tak granite (Mahawat et al., 1990), Lopburi marl (Bunopas, 1992) and Phra Wihan sandstone (Boonsener and Sonpiron, 1997) which were from different parts of Thailand (Figure 3.1). The mechanical properties for all rock types as shown in Table 3.1.

#### **3.2.1 Sample preparation for tension-induced fracture and smooth saw-cut surface**

The rock are prepared to obtain rectangular block specimens with nominal dimensions of  $50 \times 50 \times 87 \text{ mm}^3$ . The fractures having nominal areas of  $50 \times 100 \text{ mm}^2$ , as shown in Figure 3.2. The fractures are artificially made in the laboratory by tension inducing method (Figure 3.3). The normal to the fracture plane makes an angle  $60^\circ$  with the axis of the specimens. All fractures are clean and well mated. The asperity amplitudes on the fracture planes are measured from the laser-scanned

profiles along the shear direction. The readings are made to the nearest 0.01 mm. Figure 3.4 shows laser scanned images of a tension-induced fracture for the three rock types. The maximum amplitudes are used to estimate the joint roughness coefficients (JRC) of each fracture based on Barton's chart (Barton, 1982). The joint roughness coefficients are averaged as 15, 6 and 8 for the Tak granite, Phra Wihan sandstone and Lopburi marl, respectively. Figure 3.5 shows examples of the laser scanned profiles for the three rock types. For the specimens with the saw-cut surface, two specimen blocks of each rock types are used to form a complete pair of specimens primarily to avoid the effect of the groove caused by the cutting blade (Figure 3.6). Each block is cut diagonally and hence obtaining the smooth fractures with the normal making an angle of  $60^\circ$  with the major axis of the specimen for the true triaxial shear tests. Table 3.2 - 3.10 shows physical properties of specimen for all rock types.



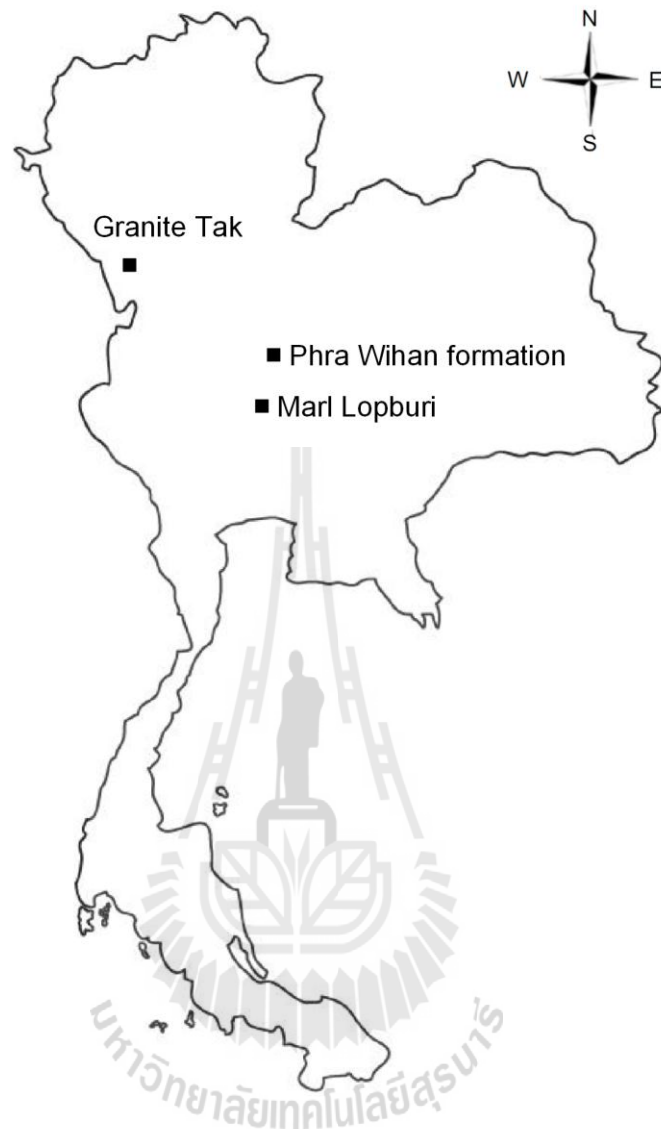


**Figure 3.1** Area of rock tested in this study.

**Table 3.1** Summary of the mechanical properties for all rock types.

Rock Type	Average Density (g/cc)	Uniaxial Compressive Strength, $\sigma_c$ (MPa)	Triaxial Compressive Strength Test (MPa)		Average JRC
			c (MPa)	$\phi$ (degrees)	
Tak Granite	$2.65 \pm 0.18^{[3]}$	$119. \pm 8.8^{[1]}$	$21.6^{[1]}$	$55.0^{[1]}$	$14 \pm 2^{[3]}$
Phra Wihan Sandstone	$2.21 \pm 0.25^{[1]}$	$71.3 \pm 9.0^{[1]}$	$8.0^{[1]}$	$47.0^{[1]}$	$6 \pm 2^{[1]}$
Lopburi Marl	$2.35 \pm 0.13^{[1]}$	$53 \pm 2.5^{[2]}$	$10.4^{[2]}$	$43.2^{[2]}$	$10 \pm 2^{[1]}$

<sup>[1]</sup>Kemthong (2006), <sup>[2]</sup>Khamrat and Fuenkajorn (2015), <sup>[3]</sup>Naphudsa and Fuenkajorn (2015)



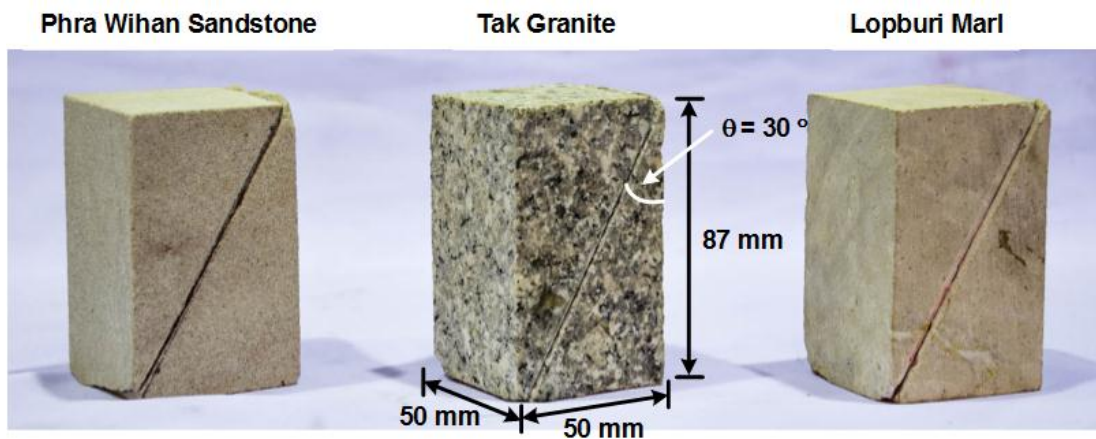


**Figure 3.2** Some specimens for the three rock types.

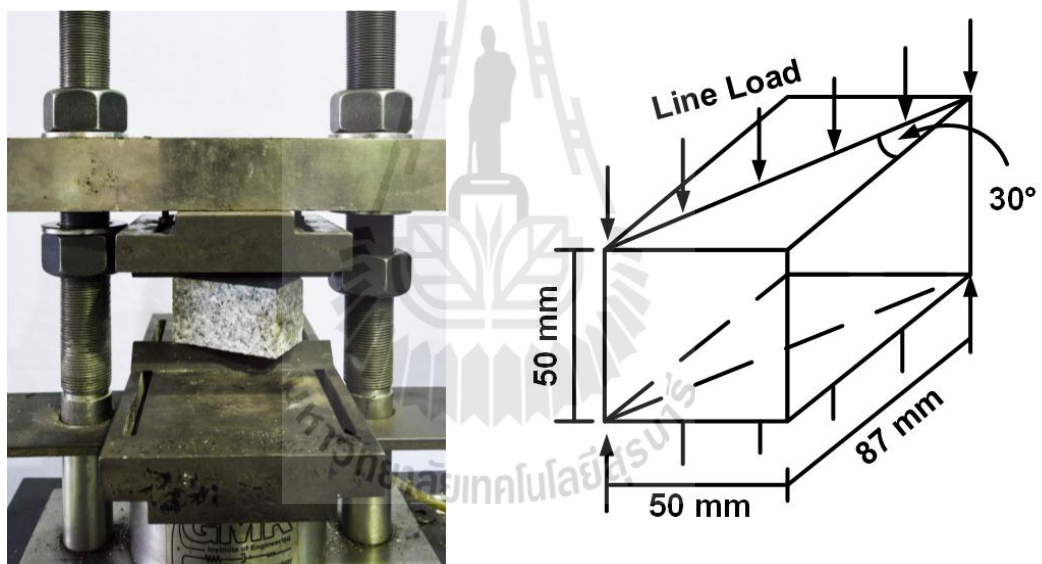


**Figure 3.3** Tension-induced fractures by line loading technique.

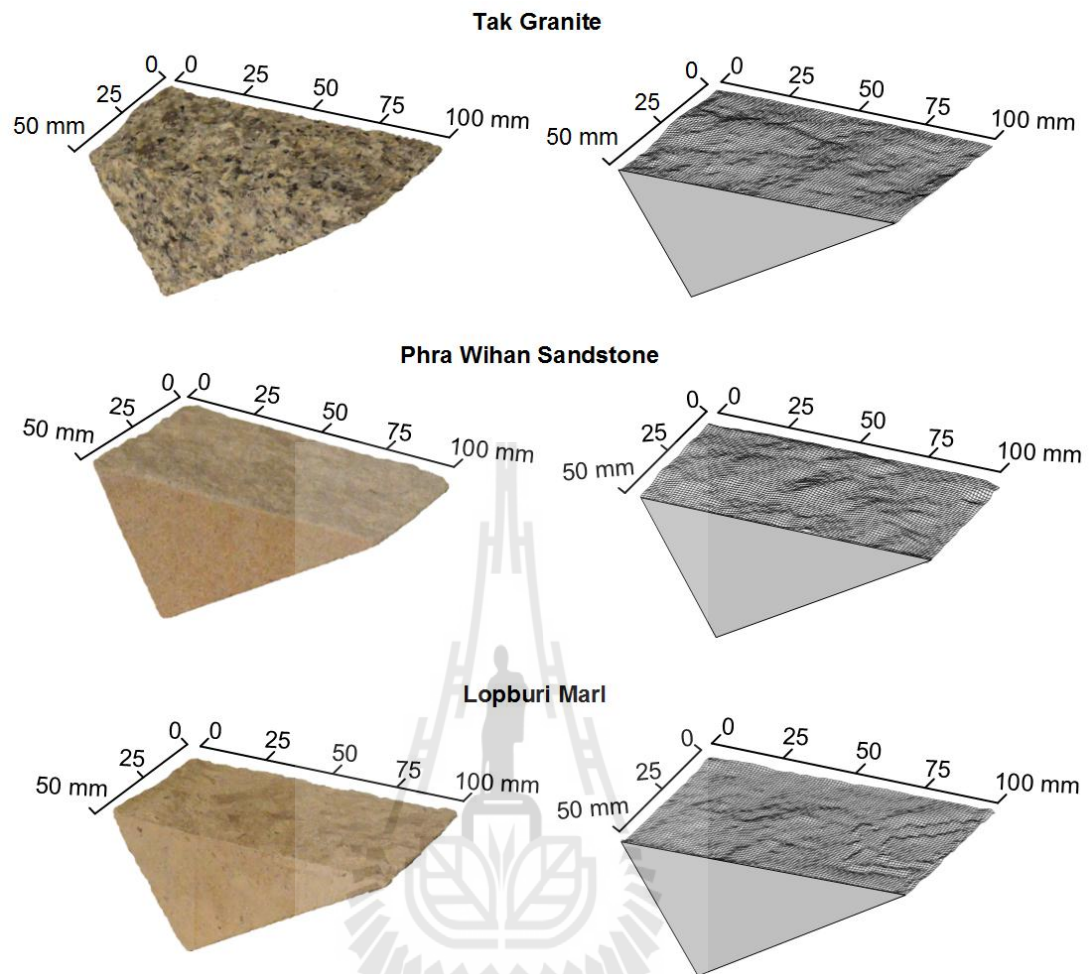


**Figure 3.4** Some tension-induced fractures and their laser scanned images.

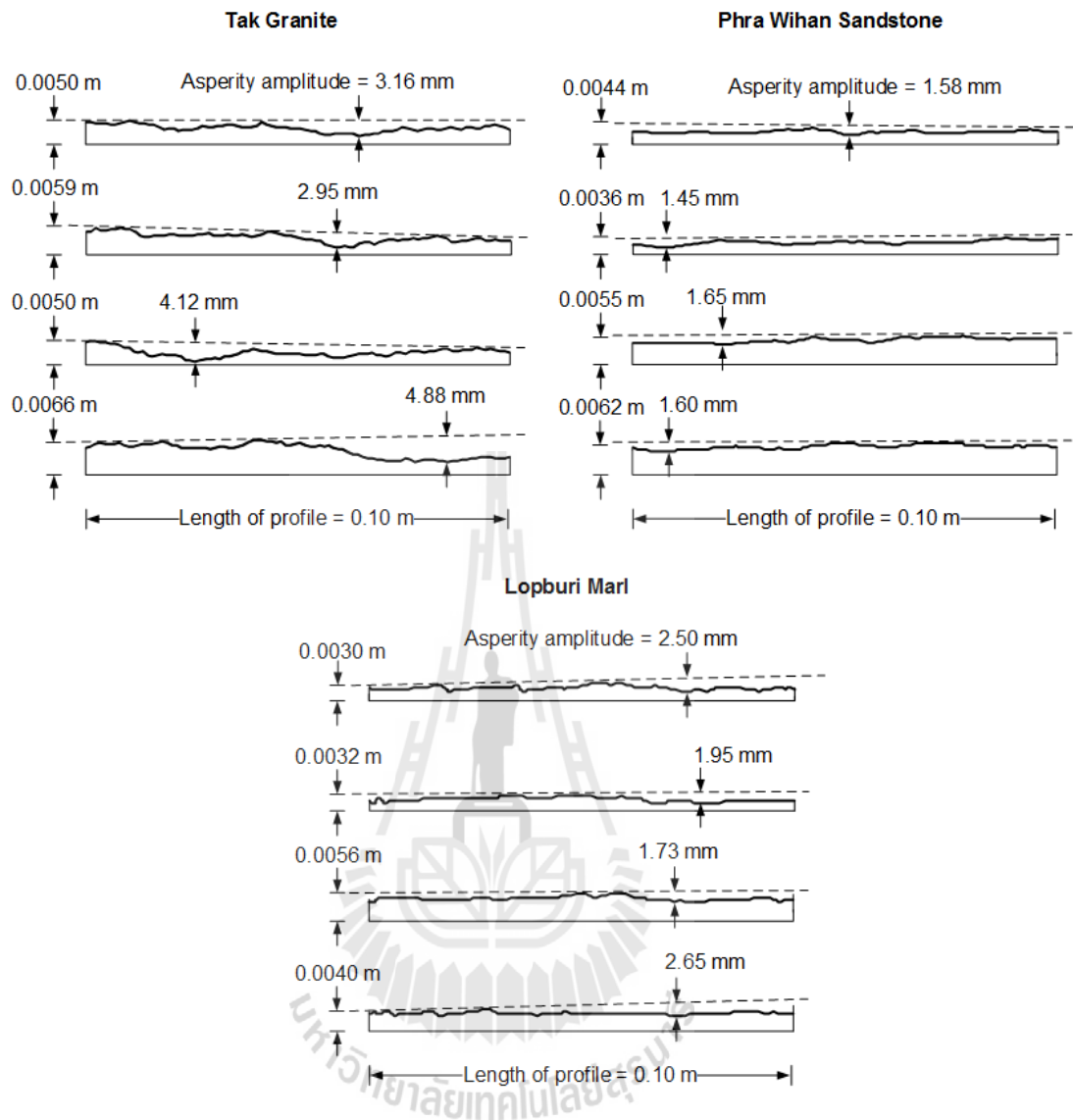


**Figure 3.5** Examples of laser-scanned profiles to measure the maximum asperity amplitude to estimate the joint roughness coefficient (JRC).

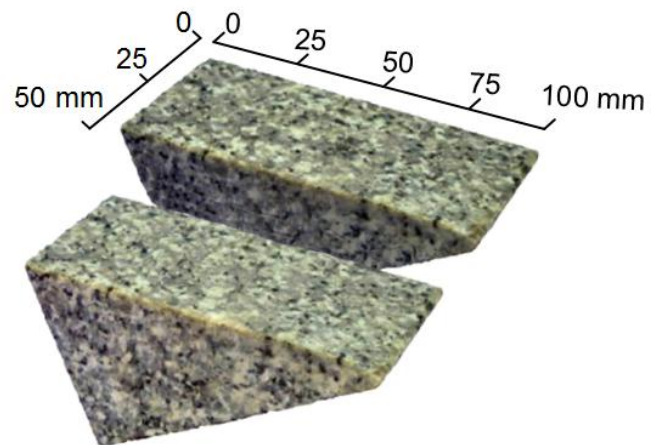


**Figure 3.6** Some specimens prepared for shear strength of saw-cut surfaces.



**Table 3.2** Summary of granite sample dimensions of the tension-induced fractures.

<b>Specimen No.</b>	<b>Dimension (mm<sup>3</sup>)</b>	<b>Density (g/cc)</b>	<b>JRC</b>
GR-01	50.05×49.50×87.20	2.74	12
GR-02	50.25×50.55×89.11	2.70	12
GR-03	49.83×51.15×88.25	2.71	11
GR-04	50.05×49.50×87.23	2.75	12
GR-05	51.02×50.53×89.03	2.72	16
GR-06	49.85×51.05×88.15	2.76	14
GR-07	50.15×50.50×88.21	2.75	14
GR-08	51.02×50.53×89.03	2.73	15
GR-09	50.05×49.50×87.24	2.74	18
GR-10	49.83×51.15×88.25	2.76	18
GR-11	50.05×49.50×87.21	2.73	13
GR-12	50.25×50.55×89.11	2.72	12
GR-13	50.05×49.50×87.22	2.82	12
GR-14	50.15×50.50×88.21	2.74	11
GR-15	51.02×50.53×89.03	2.73	12
GR-16	51.02×50.53×89.03	2.73	16
GR-17	48.95×50.55×87.96	2.75	19
GR-18	50.15×50.50×88.21	2.73	18
GR-19	48.95×50.55×87.96	2.78	15
GR-20	49.83×51.15×88.25	2.75	18
GR-21	50.05×49.50×87.22	2.85	18
GR-22	50.05×49.50×87.23	2.90	13
GR-23	48.95×50.55×87.96	2.72	13
GR-24	51.02×50.53×89.03	2.71	12
GR-25	50.25×50.55×89.11	2.61	16
GR-26	49.83×51.15×88.25	2.73	13
GR-27	50.15×50.50×88.21	2.73	19
GR-28	51.02×50.53×89.03	2.67	12
GR-29	49.85×51.05×88.17	2.79	18
GR-30	48.95×50.55×87.96	2.88	15

**Table 3.3** Summary of granite sample dimensions of the tension-induced fractures

(continue).

<b>Specimen No.</b>	<b>Dimension (mm<sup>3</sup>)</b>	<b>Density (g/cc)</b>	<b>JRC</b>
GR-31	50.15×50.50×88.21	2.68	15
GR-32	48.95×50.55×87.96	2.80	19
GR-33	49.83×51.15×88.25	2.69	12
GR-34	50.15×50.50×88.21	2.77	16
GR-35	50.25×50.55×89.11	2.69	14
GR-36	48.95×50.55×87.96	2.82	15
GR-37	48.95×50.55×87.96	2.88	15
GR-38	50.25×50.55×89.11	2.77	18
GR-39	51.02×50.53×89.03	2.61	18
GR-40	50.15×50.50×88.21	2.73	18



**Table 3.4** Summary of sandstone sample dimensions of the tension-induced fractures.

<b>Specimen No.</b>	<b>Dimension (mm<sup>3</sup>)</b>	<b>Density (g/cc)</b>	<b>JRC</b>
PW-01	50.05×49.50×87.22	2.19	6
PW-02	50.05×49.50×87.23	2.17	7
PW-03	48.95×50.55×87.96	2.18	5
PW-04	51.02×50.53×89.03	2.20	5
PW-05	50.25×50.55×89.11	2.20	6
PW-06	49.83×51.15×88.25	2.23	6
PW-07	50.15×50.50×88.21	2.22	6
PW-08	51.02×50.53×89.03	2.20	5
PW-09	49.85×51.05×88.17	2.18	7
PW-10	48.95×50.55×87.96	2.23	6
PW-11	50.15×50.50×88.21	2.18	6
PW-12	48.95×50.55×87.96	2.19	6
PW-13	49.83×51.15×88.25	2.27	6
PW-14	50.15×50.50×88.21	2.21	5
PW-15	50.25×50.55×89.11	2.20	5
PW-16	48.95×50.55×87.96	2.20	5
PW-17	48.95×50.55×87.96	2.20	6
PW-18	50.25×50.55×89.11	2.19	6
PW-19	51.02×50.53×89.03	2.23	5
PW-20	50.15×50.50×88.21	2.21	5
PW-21	50.05×49.50×87.20	2.29	7
PW-22	50.25×50.55×89.11	2.34	6
PW-23	49.83×51.15×88.25	2.17	6
PW-24	50.05×49.50×87.23	2.18	6
PW-25	51.02×50.53×89.03	2.08	5
PW-26	49.85×51.05×88.15	2.20	6
PW-27	50.15×50.50×88.21	2.19	5
PW-28	51.02×50.53×89.03	2.15	7
PW-29	50.05×49.50×87.24	2.26	5
PW-30	49.83×51.15×88.25	2.32	6

**Table 3.5** Summary of sandstone sample dimensions of the tension-induced fractures  
(continue).

<b>Specimen No.</b>	<b>Dimension (mm<sup>3</sup>)</b>	<b>Density (g/cc)</b>	<b>JRC</b>
PW-31	50.05×49.50×87.21	2.14	6
PW-32	50.25×50.55×89.11	2.25	6
PW-33	50.05×49.50×87.22	2.16	6
PW-34	50.15×50.50×88.21	2.23	6
PW-35	51.02×50.53×89.03	2.16	7
PW-36	51.02×50.53×89.03	2.27	5
PW-37	48.95×50.55×87.96	2.32	5
PW-38	50.15×50.50×88.21	2.24	7
PW-39	48.95×50.55×87.96	2.08	7
PW-40	49.83×51.15×88.25	2.19	6



**Table 3.6** Summary of marl sample dimensions of the tension-induced fractures.

<b>Specimen No.</b>	<b>Dimension (mm<sup>3</sup>)</b>	<b>Density (g/cc)</b>	<b>JRC</b>
MA-01	51.02×50.53×89.03	2.33	8
MA-02	50.05×49.50×87.24	2.31	9
MA-03	49.83×51.15×88.25	2.31	7
MA-04	50.05×49.50×87.21	2.34	7
MA-05	50.25×50.55×89.11	2.33	8
MA-06	50.05×49.50×87.22	2.36	8
MA-07	50.15×50.50×88.21	2.35	8
MA-08	51.02×50.53×89.03	2.34	7
MA-09	51.02×50.53×89.03	2.32	9
MA-10	48.95×50.55×87.96	2.36	8
MA-11	50.15×50.50×88.21	2.31	8
MA-12	48.95×50.55×87.96	2.32	8
MA-13	49.83×51.15×88.25	2.41	8
MA-14	50.25×50.55×89.11	2.34	7
MA-15	48.95×50.55×87.96	2.34	7
MA-16	48.95×50.55×87.96	2.34	7
MA-17	50.25×50.55×89.11	2.33	8
MA-18	51.02×50.53×89.03	2.33	8
MA-19	50.15×50.50×88.21	2.37	7
MA-20	50.15×50.50×88.21	2.35	7
MA-21	50.05×49.50×87.20	2.43	9
MA-22	50.25×50.55×89.11	2.48	8
MA-23	49.83×51.15×88.25	2.31	8
MA-24	50.05×49.50×87.23	2.31	8
MA-25	51.02×50.53×89.03	2.21	7
MA-26	49.85×51.05×88.15	2.33	8
MA-27	50.15×50.50×88.21	2.33	7
MA-28	50.05×49.50×87.22	2.28	9
MA-29	50.05×49.50×87.23	2.39	7
MA-30	48.95×50.55×87.96	2.46	8

**Table 3.7** Summary of marl sample dimensions of the tension-induced fractures  
(continue).

<b>Specimen No.</b>	<b>Dimension (mm<sup>3</sup>)</b>	<b>Density (g/cc)</b>	<b>JRC</b>
MA-31	51.02×50.53×89.03	2.27	8
MA-32	50.25×50.55×89.11	2.39	8
MA-33	49.83×51.15×88.25	2.29	8
MA-34	50.15×50.50×88.21	2.36	8
MA-35	51.02×50.53×89.03	2.30	9
MA-36	49.85×51.05×88.17	2.40	7
MA-37	48.95×50.55×87.96	2.46	7
MA-38	50.15×50.50×88.21	2.37	9
MA-39	48.95×50.55×87.96	2.21	9
MA-40	49.83×51.15×88.25	2.33	8



**Table 3.8** Summary of granite sample dimensions of the saw-cut surfaces.

<b>Specimen No.</b>	<b>Dimension (mm<sup>3</sup>)</b>	<b>Density (g/cc)</b>
GR-41	50.05×49.50×87.21	2.73
GR-42	50.25×50.55×89.11	2.72
GR-43	50.05×49.50×87.22	2.82
GR-44	50.15×50.50×88.21	2.74
GR-45	51.02×50.53×89.03	2.73
GR-46	51.02×50.53×89.03	2.73
GR-47	48.95×50.55×87.96	2.75
GR-48	50.15×50.50×88.21	2.73
GR-49	48.95×50.55×87.96	2.78
GR-50	49.83×51.15×88.25	2.75
GR-51	50.05×49.50×87.22	2.85
GR-52	50.05×49.50×87.23	2.90



**Table 3.9** Summary of sandstone sample dimensions of the saw-cut surfaces.

<b>Specimen No.</b>	<b>Dimension (mm<sup>3</sup>)</b>	<b>Density (g/cc)</b>
PW-41	50.15×50.50×88.21	2.21
PW-42	50.05×49.50×87.20	2.29
PW-43	50.25×50.55×89.11	2.34
PW-44	49.83×51.15×88.25	2.17
PW-45	50.05×49.50×87.23	2.18
PW-46	51.02×50.53×89.03	2.08
PW-47	49.85×51.05×88.15	2.20
PW-48	50.15×50.50×88.21	2.19
PW-49	51.02×50.53×89.03	2.15
PW-50	50.05×49.50×87.24	2.26
PW-51	49.83×51.15×88.25	2.32
PW-52	50.05×49.50×87.21	2.14



**Table 3.10** Summary of marl sample dimensions of the saw-cut surfaces.

<b>Specimen No.</b>	<b>Dimension (mm<sup>3</sup>)</b>	<b>Density (g/cc)</b>
MA-41	48.95×50.55×87.96	2.32
MA-42	49.83×51.15×88.25	2.41
MA-43	50.25×50.55×89.11	2.34
MA-44	48.95×50.55×87.96	2.34
MA-45	48.95×50.55×87.96	2.34
MA-46	50.25×50.55×89.11	2.33
MA-47	51.02×50.53×89.03	2.33
MA-48	50.15×50.50×88.21	2.37
MA-49	50.15×50.50×88.21	2.35
MA-50	50.05×49.50×87.20	2.43
MA-51	50.25×50.55×89.11	2.48
MA-52	49.83×51.15×88.25	2.31



### 3.2.2 Direct shear tests on tension-induced fractures

The samples for the direct shear test are prepared to have fractures area of  $100 \times 50 \text{ mm}^2$ . The fractures are artificially made in the laboratory by tension inducing and saw cut methods. Figure 3.7 shows examples of rock fractures prepared in the three rock types. Table 3.11 - 3.13 shows physical properties of specimen for all rock types. The estimate joint roughness coefficients (JRC) of each fracture for the direct shear testing are identical to those of the triaxial shear testing on tension-induced fractures. The joint roughness coefficients are averaged as 13, 6 and 7 for the Tak granite, Phra Wihan sandstone and Lopburi marl, respectively.



**Figure 3.7** Some specimens prepared for direct shear tests.

**Table 3.11** Sample dimensions of granite prepared for the direct shear tests.

<b>Specimen No.</b>	<b>Dimension (mm<sup>3</sup>)</b>	<b>Density (g/cc)</b>	<b>JRC</b>
GR-53	50.15×50.50×100.21	2.68	14
GR-54	49.95×50.55×99.96	2.80	13
GR-55	49.83×51.15×100.25	2.69	12
GR-56	50.15×50.50×100.21	2.77	13
GR-57	50.25×50.55×100.11	2.69	13
GR-58	49.95×50.55×99.96	2.82	14
GR-59	49.95×50.55×99.96	2.88	15
GR-60	50.25×50.55×100.11	2.77	13



**Table 3.12** Sample dimensions of sandstone prepared for the direct shear tests.

<b>Specimen No.</b>	<b>Dimension (mm<sup>3</sup>)</b>	<b>Density (g/cc)</b>	<b>JRC</b>
PW-53	50.15×50.50×100.21	2.18	7
PW-54	49.95×50.55×99.96	2.19	6
PW-55	49.83×51.15×100.25	2.27	6
PW-56	50.15×50.50×100.21	2.21	5
PW-57	50.25×50.55×100.11	2.20	5
PW-58	49.95×50.55×99.96	2.20	5
PW-59	49.95×50.55×99.96	2.20	7
PW-60	50.25×50.55×100.11	2.19	6



**Table 3.13** Sample dimensions of marl prepared for the direct shear tests.

<b>Specimen No.</b>	<b>Dimension (mm<sup>3</sup>)</b>	<b>Density (g/cc)</b>	<b>JRC</b>
MA-53	51.02×50.53×100.03	2.34	7
MA-54	51.02×50.53×100.03	2.32	6
MA-55	49.95×50.55×99.96	2.36	8
MA-56	50.15×50.50×100.21	2.31	8
MA-57	49.95×50.55×99.96	2.32	8
MA-58	49.83×51.15×100.25	2.41	8
MA-59	50.25×50.55×100.11	2.34	7
MA-60	49.95×50.55×99.96	2.34	7



## **CHAPTER IV**

### **LABORATORY TESTING**

#### **4.1 Introduction**

The objective of this section is to describe the method to determine the shear resistance of fractures in three rock types under triaxial stresses. The laboratory tests are divided into two series; 1) triaxial shear test on tension-induced fractures and smooth saw-cut surface and 2) direct shear test on tension-induced fractures.

#### **4.2 Triaxial shear test on tension-induced fractures and smooth saw-cut surface**

A polyaxial load frame (Fuenkajorn et al., 2012) is used to apply triaxial stresses to the specimens because the cantilever beams with pre-calibrated dead weight can apply a truly constant lateral stress (confining pressure) to the specimen. The lateral stresses are applied by two pairs of 152 cm long cantilever beams set in mutually perpendicular directions. The outer end of each beam is pulled down by a dead weight placed on a lower steel bar linking the two opposite beams underneath. The beam inner end is hinged by a pin mounted between vertical bars on each side of the frame. During testing all beams are arranged nearly horizontally, and hence a lateral compressive load results on the specimen placed at the center of the frame. Using different distances from the pin to the outer weighting point and to the inner loading point, a load magnification of 12 to

1 is obtained. This loading ratio is also used to determine the lateral deformation of the specimen by monitoring the vertical movement of the two steel bars below. Figure 4.1 shows the polyaxial load frame used. The lateral stresses is parallel to the strike of the fracture plane which is designated as equal with the normal to the strike of the fracture plane for confinement condition. The rock is installed into the polyaxial load frame. Neoprene sheets are used to minimize the friction at all interfaces between the loading platen and the rock surface. Dead weights are placed on the two lower bars to obtain the pre-defined magnitude of the lateral stresses on the specimen. Simultaneously the axial (vertical) stress is increased to the same value with lateral stresses. The specimen is first loaded under hydrostatic condition. The test is started by increasing the axial displacement at a constant rate ranging from  $10^{-5}$  to  $10^{-2}$  mm/s using the electric oil pump while lateral stresses are maintained constant. The lateral stresses are from 1, 3, 7, 12 to 18 MPa for tension-induced fractures and up to 12 MPa for smooth saw-cut surfaces. The axial and lateral displacements are recorded. The test is terminated when a total axial displacement of 8 mm is reached. After shearing the fractures are examined and photographed. Figure. 4.2 shows the directions of the applied stresses with respect to the fracture orientation.

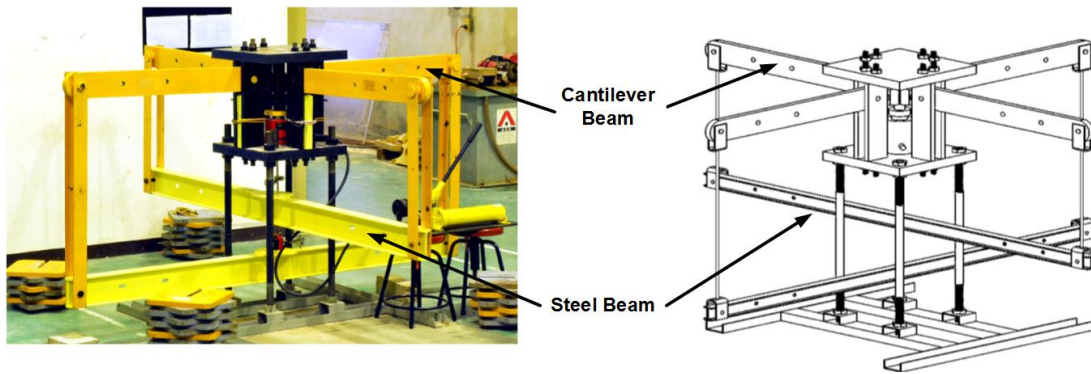


**Figure 4.1** Polyaxial load frame (Fuenkajorn et al., 2012).

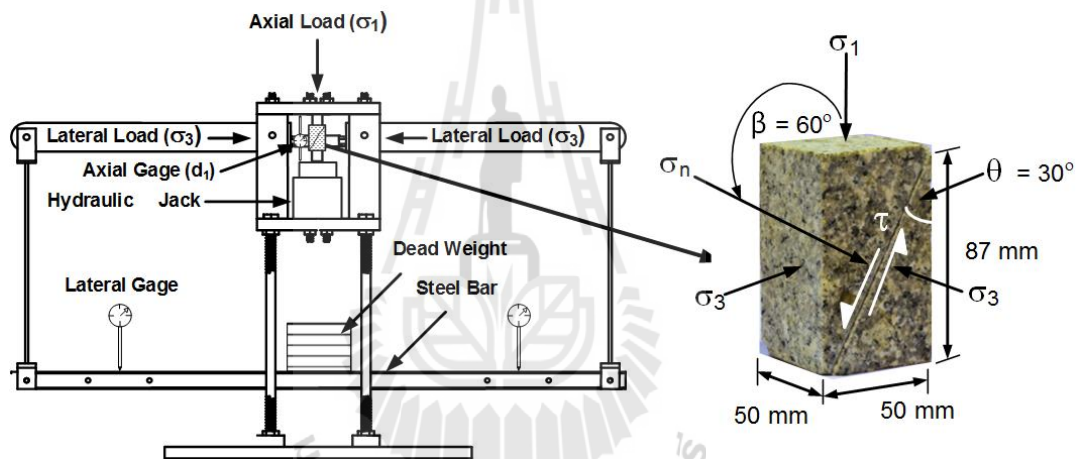


**Figure 4.2** Directions of applied stresses with respect to the fracture orientation.

The shear stress ( $\tau$ ) and its corresponding normal stress ( $\sigma_n$ ) can be determined from the applied principal stresses ( $\sigma_1$  and  $\sigma_3$ ) as follows (Jaeger et al., 2007; Barton, 2013):

$$\tau = \frac{1}{2}(\sigma_1 - \sigma_3) \cdot \sin 2\beta \quad (4.1)$$

$$\sigma_n = \frac{1}{2}(\sigma_1 + \sigma_3) + \frac{1}{2}(\sigma_1 - \sigma_3) \cdot \cos 2\beta \quad (4.2)$$

where  $\beta$  is the angle between  $\sigma_1$  and  $\sigma_n$  directions. The shear and normal displacements can be calculated from. The shear displacements can be:

$$d_s = d_1 \cdot \cos \theta + d_3 \cdot \sin \theta \quad (4.3)$$

$$d_n = d_3 \cdot \cos \theta - d_1 \cdot \sin \theta \quad (4.4)$$

$$d_3 = \text{Vertical movement of steel beam} / 12 \quad (4.5)$$

where  $\theta$  is the angle between  $\sigma_1$  and fracture plane (i.e.  $\theta = 90 - \beta$ ). For all specimens the angle  $\beta$  and  $\theta$  are equal to 60 and 30 degrees, respectively. The fracture displacements,  $d_1$ , and  $d_3$  are monitored in the axial ( $\sigma_1$ ) direction and the lateral ( $\sigma_3$ ) direction (normal to the strike of the fracture) during the test. The lateral displacement  $d_3$  is calculated by dividing the vertical movement by of steel beam by 12 (Eq. (4.5))

From Eq. (4.3) the rate of shear displacements or shear velocity ( $\dot{d}_s$ ) that are equivalent to axial displacement rate ( $\dot{d}_1$ ) can be calculated as  $1.15 \times 10^{-5}$  to  $1.15 \times 10^{-2}$  mm/s. Figure. 4.3 show the direction relations of the fracture displacements.

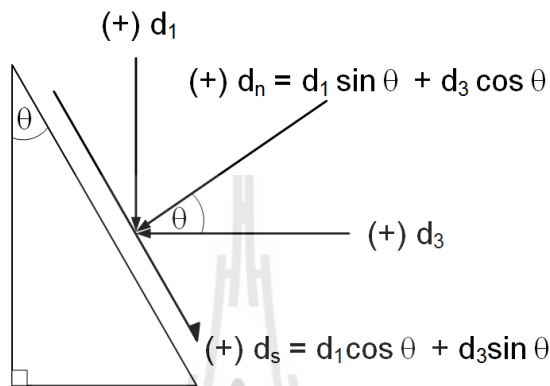


**Figure. 4.3** Direction relations of the fracture displacements.

### 4.3 Direct shear test on tension-induced fractures

The direct shear tests are performed on the tension-induced fractures of the three rock types to verify the reliability of the triaxial shear test results above and to correlate the fracture shear strengths obtained from the tests. The test method and calculation for the direct shear test follow the ASTM (D5607-08) standard and the ISRM suggested method (Brown, 1981), as much as practical. Figure 4.4 shows the direct shear device used in this test. A shear direction is pre-defined. The selected normal stresses ( $\sigma_n$ ) are 1, 2, 3 and 4 MPa (for  $50 \times 100 \text{ mm}^2$  fracture area). These normal stresses are lower than those used in the triaxial shear test primarily due to the load limitations of the direct shear device. Each specimen is sheared only once for each normal stress using a constant shearing rate of  $2.5 \times 10^{-3}$  mm/s. Shear force is continuously applied until a total shear displacement of 8 mm is

reached. Figure 4.5 shows the displacement dial gages used to measure the shear displacement and fracture dilation. The peak and residual shear loads are monitored. The shear strength ( $\tau$ ) is calculated by the equation;

$$\tau = P / A \quad (4.4)$$

where  $P$  is the shear force and  $A$  is the contact area between both specimens. It is assumed here that since the total displacement is small (less than 1 cm), the contact area ( $A$ ) is taken as constant during the shear test. The normal displacements ( $d_n$ ) is recorded. The test is terminated when a total shear displacement ( $d_s$ ) of 8 mm is reached.



**Figure 4.4** Direct shear device used in this study.

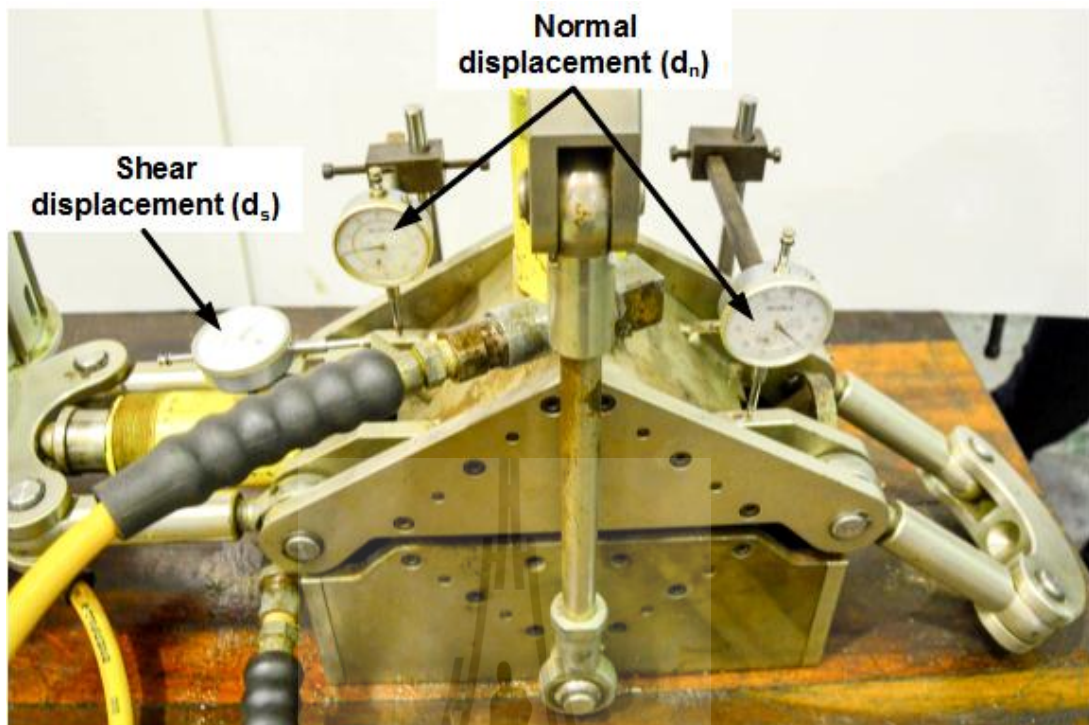
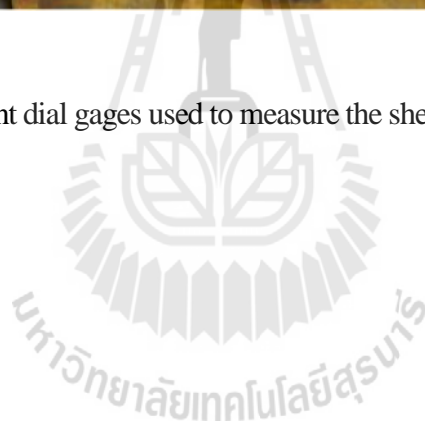


**Figure 4.5** Displacement dial gages used to measure the shear displacement and fracture dilation.



# **CHAPTER V**

## **TEST RESULTS**

Three test series are performed as follows: (1) triaxial shear tests on tension-induced fractures, (2) triaxial shear tests on smooth saw-cut surfaces, and (3) direct shear tests on tension-induced fractures. This section describes the test results.

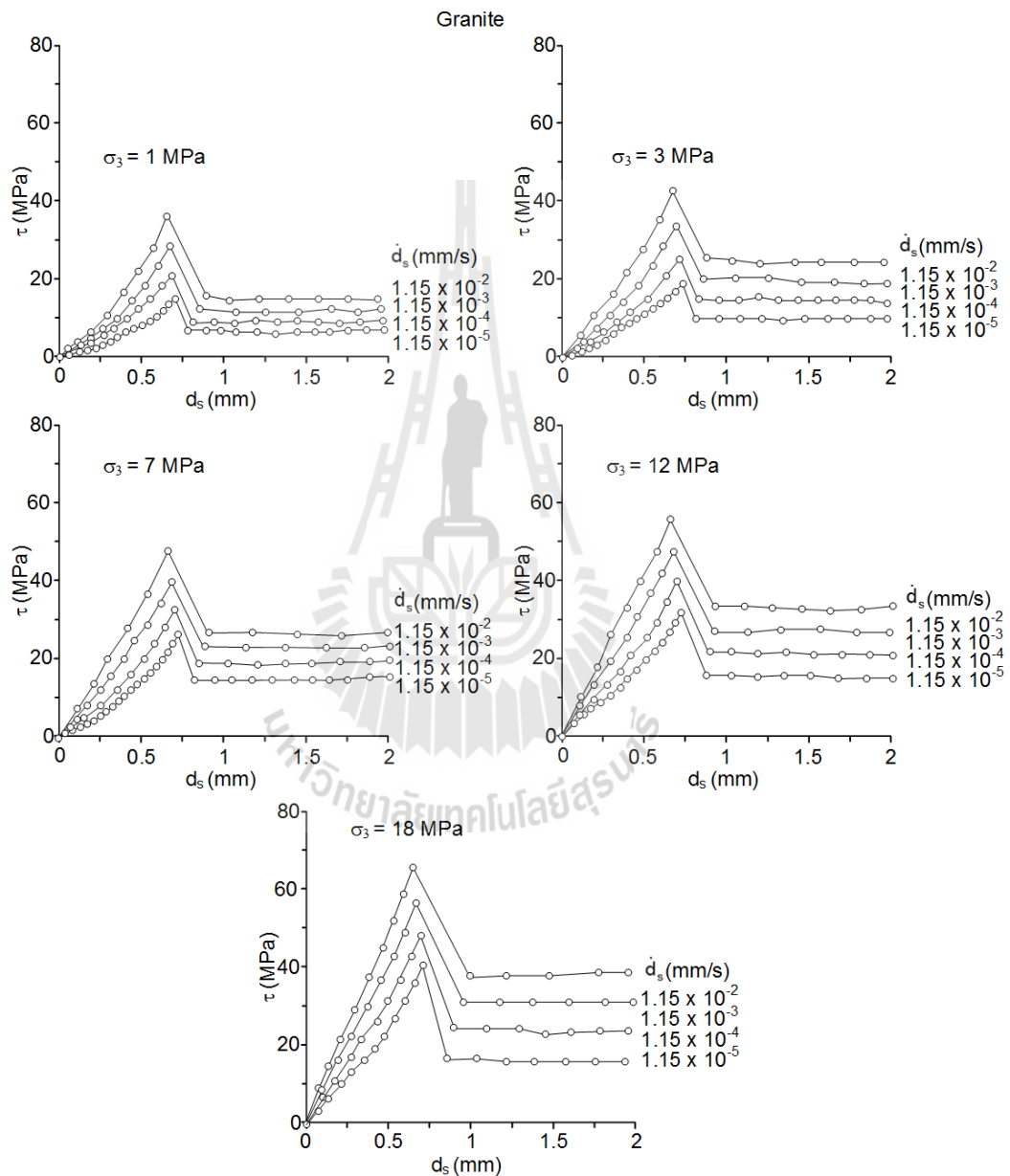
### **5.1 Triaxial shear test on tension-induced fractures**

For this test series the shear strengths are determined for shear velocities varying from  $1.15 \times 10^{-5}$  to  $1.15 \times 10^{-2}$  mm/s with the constant confining pressures ( $\sigma_3$ ) from 1, 3, 7, 12 to 18 MPa. The results are presented in forms of shear stress-displacement curves, shear strengths as a function of normal stress and dilation of the fractures during shearing.

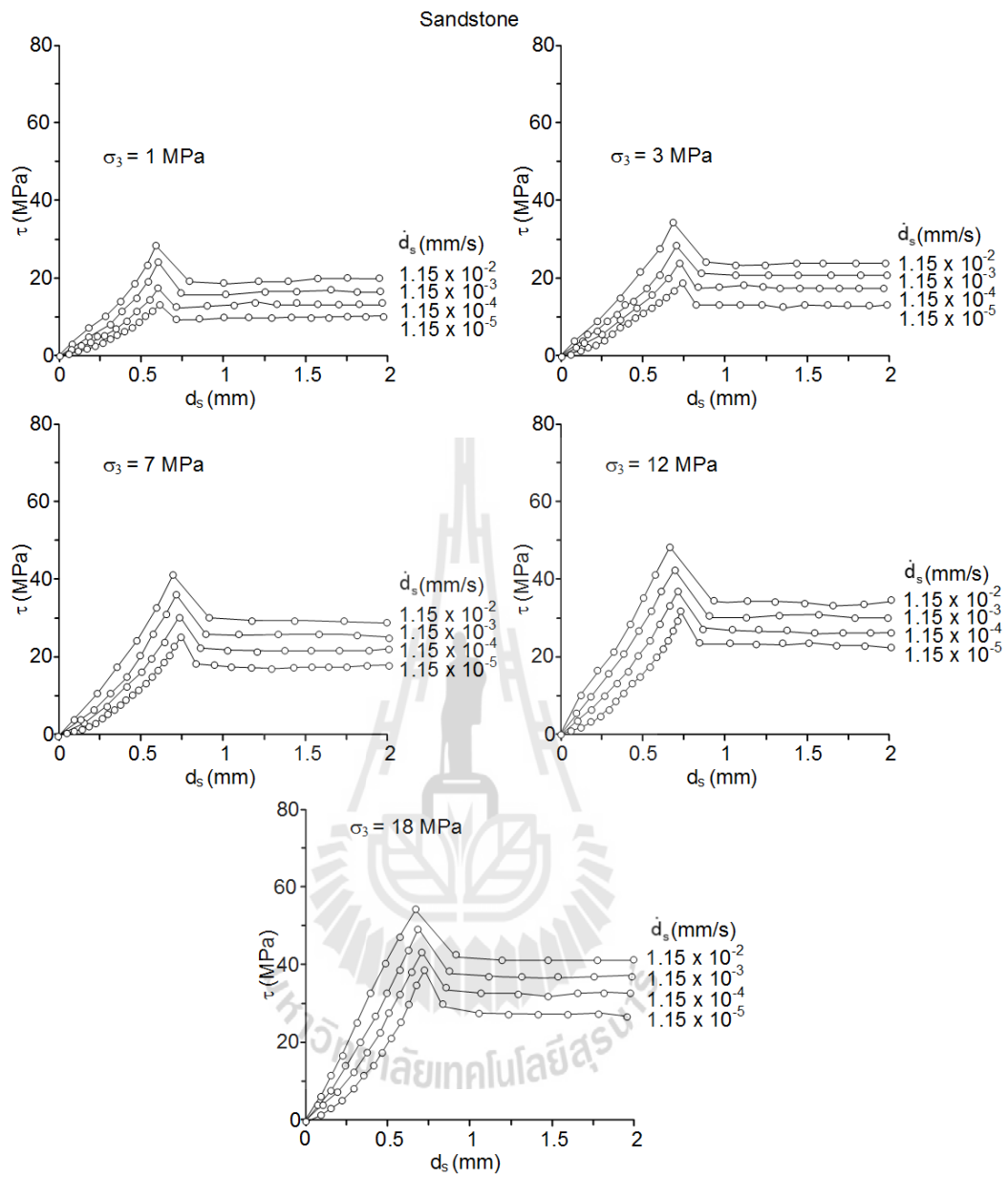
#### **5.1.1 Shear stress-displacement curves**

The shear stress-displacement ( $\tau$ - $d_s$ ) curves for the three rock types are shown in Figures 5.1 through 5.3. It is clear that the shear strengths increase with the shear velocities. For all rock types the peak and residual stresses can be detected. The effects of shear velocity tend to be enhanced under larger confining pressures. This is suggested by that the difference of the peak shearing resistance among different shear velocities tend to increase when the confining pressures are increased. This holds true for all rock types. Nevertheless, such phenomenon can be only seen for the fractures in granite. The mechanisms governing such behavior probably relate to the fracture roughness and the mineral compositions of the rocks. In additions the differences between the peak and residual shear stresses are notably reduced when the fractures are

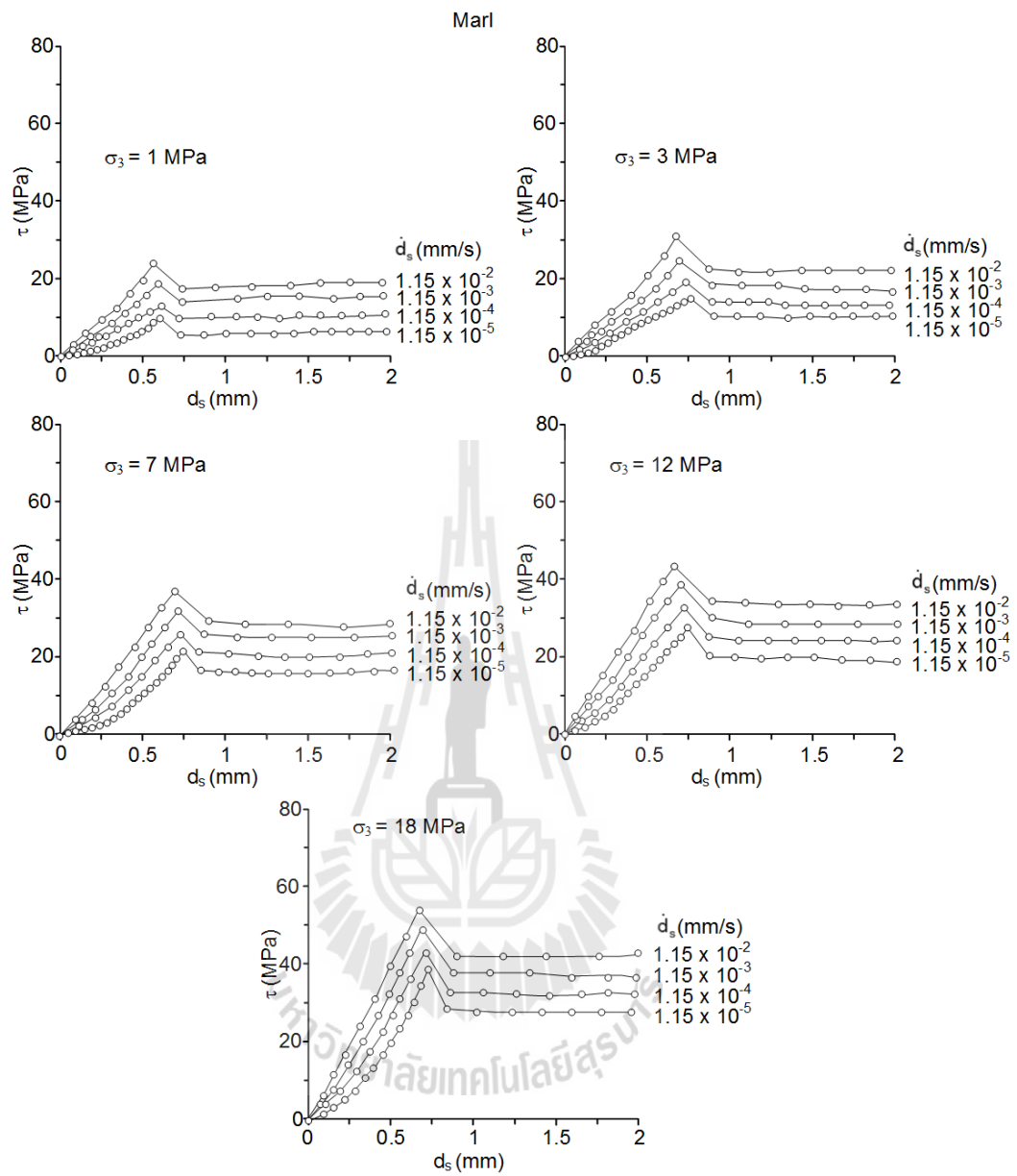
subjected to low shear velocities. The fractures with lower JRC values (i.e., marl and sandstone) also shear smaller differences of the peak and residual shear stresses as compared to those with greater JRC values (i.e. granite).



**Figures 5.1** Shear stresses ( $\tau$ ) as a function of shear displacement ( $d_s$ ) for granite.



**Figures 5.2** Shear stresses ( $\tau$ ) as a function of shear displacement ( $d_s$ ) sandstone.



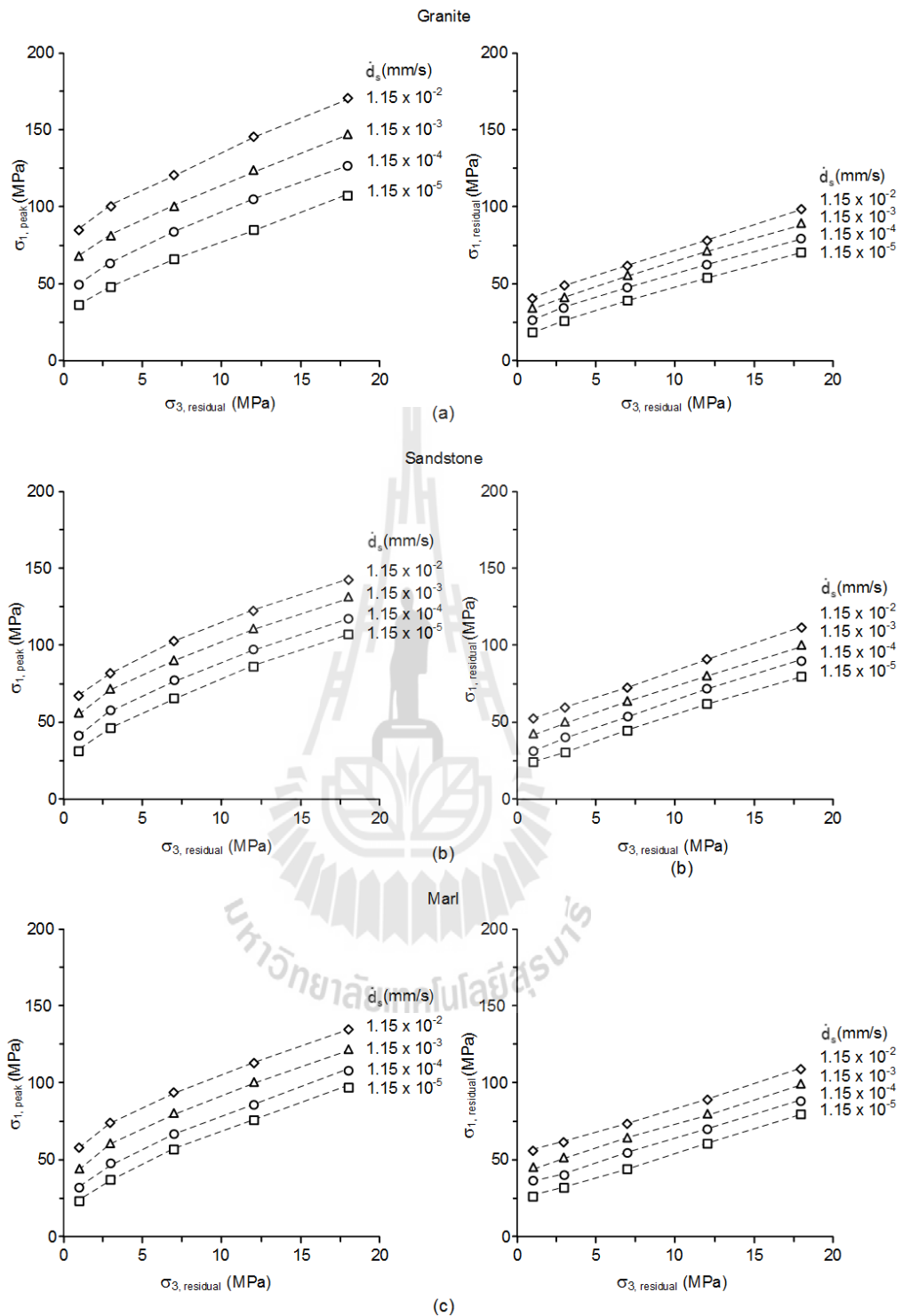
**Figures 5.3** Shear stresses ( $\tau$ ) as a function of shear displacement ( $d_s$ ) for marl.

### 5.1.2 Principal stress at peak and residual regions

Figure 5.4 shows the major principal stresses at peak and residual for the three rock types as a function of the confining stress ( $\sigma_3$ ) under various shear velocities. The major principle stresses for both peak and residual increase with confining pressures. The lower shear velocity induces lower peak and residual stresses. Such effect pronounces more for the fractures in granite when its fractures have the greatest JRC values. The decreasing rate of the peak and residual stresses tend to be uniform with the changes of the order of the shear velocities.

### 5.1.3 Shear-normal stresses diagrams

The results of the triaxial shear tests performed here can be presented in the forms of the shear-normal stresses diagram. The stresses can be calculated from Eqs. (4.1) and (4.2) in chapter IV. Tables 5.1 through 5.3 show the calculation results for the three rock types. Figure 5.5 plots the shear stresses as a function of normal stresses for both peak and residual. Non-linear behavior of the  $\tau$ - $\sigma_n$  relation is observed. Again the effects of the shear velocity can be seen by the reduction of the shear stresses as the shear velocities decrease. It should be noted that the  $\tau$ - $\sigma_n$  curves prior to the peak stress obtained from the triaxial shear testing will be different from those obtained from the conventional direct shear test. This is primary due to the fact that the normal stress for the triaxial shear testing continuously increase as the axial and shear stresses increase. This results in an continuously increase of the  $\tau$ - $\sigma_n$  slope prior to the peak stress. As a result the continuous changing of the  $\sigma_n$  during shearing makes it impossible to determine the joint shear stiffness for the triaxial shear testing.



**Figures 5.4** Major principle stress ( $\sigma_1$ ) as a function of the confining stress ( $\sigma_3$ ) under various shear velocities. Peak (left) and residual (right) stresses are shown.

**Table 5.1** Summary of peak and residual shear strengths and their corresponding normal stresses for granite.

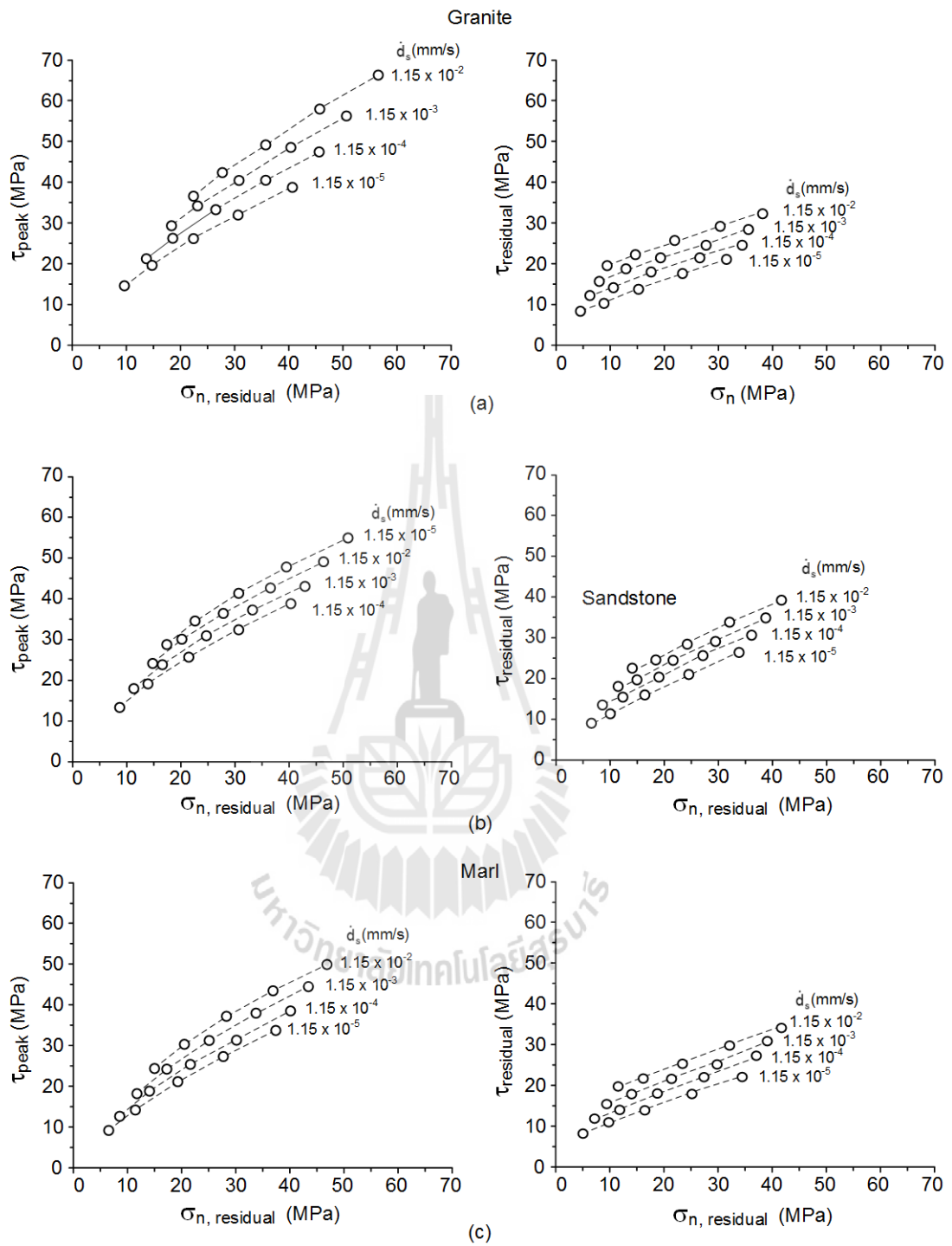
$\dot{d}_s$ (mm/s)	$\sigma_3$ (MPa)	Peak shear strength			Residual shear strength		
		$\sigma_{1, \text{peak}}$ (MPa)	$\sigma_{n, \text{peak}}$ (MPa)	$\tau_{\text{peak}}$ (MPa)	$\sigma_{1, \text{residual}}$ (MPa)	$\sigma_{n, \text{residual}}$ (MPa)	$\tau_{\text{residual}}$ (MPa)
$1.15 \times 10^{-2}$	1	84.32	21.33	36.08	40.12	10.75	16.89
	3	99.44	26.61	41.76	49.58	14.50	19.92
	7	119.6	34.65	48.76	61.15	20.50	23.38
	12	144.8	44.70	57.50	78.55	28.50	28.58
	18	170	55.50	65.82	98.23	38.00	34.64
$1.15 \times 10^{-3}$	1	67.52	17.13	28.80	33.17	9.00	13.86
	3	80.96	21.99	33.76	42.19	12.75	16.89
	7	99.44	29.61	40.03	56.28	19.25	21.22
	12	122.96	39.24	48.05	70.34	26.50	25.11
	18	146.48	49.62	55.63	90.25	36.00	31.18
$1.15 \times 10^{-4}$	1	49.04	12.51	20.80	26.31	7.25	10.83
	3	62.48	17.37	25.76	34.33	10.75	13.42
	7	82.64	25.41	32.75	48.35	17.25	17.75
	12	104.48	34.62	40.05	62.37	24.50	21.65
	18	126.32	44.58	46.90	80.39	33.50	26.85
$1.15 \times 10^{-5}$	1	35.936	8.48	15.13	19.41	5.50	7.79
	3	47.36	13.59	19.21	26.43	8.75	9.96
	7	66.008	21.25	25.55	39.45	15.00	13.86
	12	84.32	29.58	31.32	54.47	22.50	18.19
	18	106.16	39.54	38.17	71.49	31.25	22.95

**Table 5.2** Summary of peak and residual shear strengths and their corresponding normal stresses for sandstone.

$\dot{d}_s$ (mm/s)	$\sigma_3$ (MPa)	Peak shear strength			Residual shear strength		
		$\sigma_{1, \text{peak}}$ (MPa)	$\sigma_{n, \text{peak}}$ (MPa)	$\tau_{\text{peak}}$ (MPa)	$\sigma_{1, \text{residual}}$ (MPa)	$\sigma_{n, \text{residual}}$ (MPa)	$\tau_{\text{residual}}$ (MPa)
$1.15 \times 10^{-2}$	1	67.32	17.58	28.72	52.27	13.75	22.08
	3	82.32	22.83	34.35	60.27	17.25	24.68
	7	102.04	30.76	41.15	75.28	24.00	29.44
	12	122.24	39.56	47.74	92.28	32.00	34.64
	18	142.44	49.11	53.88	112.29	41.50	40.70
$1.15 \times 10^{-3}$	1	56.28	14.82	23.94	42.29	11.25	17.75
	3	72.32	20.33	30.02	50.29	14.75	20.35
	7	90.64	27.91	36.22	65.03	21.43	25.00
	12	110.41	36.60	42.61	81.62	29.32	30.00
	18	131.23	46.31	49.03	100.25	38.50	35.51
$1.15 \times 10^{-4}$	1	42.06	11.27	17.78	31.16	8.50	12.99
	3	57.90	16.73	23.77	39.07	12.00	15.59
	7	77.74	24.69	30.63	55.35	19.00	20.78
	12	97.24	33.31	36.91	72.37	27.00	25.98
	18	117.52	42.88	43.09	90.39	36.00	31.18
$1.15 \times 10^{-5}$	1	31.52	8.63	13.22	23.41	6.50	9.53
	3	46.69	13.92	18.92	31.15	9.93	12.00
	7	65.84	21.71	25.48	45.45	16.50	16.45
	12	86.73	30.68	32.36	62.47	24.50	21.65
	18	107.20	40.30	38.62	80.49	33.50	26.85

**Table 5.3** Summary of peak and residual shear strengths and their corresponding normal stresses for marl.

$\dot{d}_s$ (mm/s)	$\sigma_3$ (MPa)	Peak shear strength			Residual shear strength		
		$\sigma_{1, \text{peak}}$ (MPa)	$\sigma_{n, \text{peak}}$ (MPa)	$\tau_{\text{peak}}$ (MPa)	$\sigma_{1, \text{residual}}$ (MPa)	$\sigma_{n, \text{residual}}$ (MPa)	$\tau_{\text{residual}}$ (MPa)
$1.15 \times 10^{-2}$	1	58.24	15.31	24.79	55.14	14.50	23.38
	3	74.22	20.81	30.84	60.17	17.25	24.68
	7	93.50	28.63	37.46	73.19	23.50	28.58
	12	112.88	37.22	43.68	89.21	31.25	33.34
	18	134.40	47.10	50.40	108.24	40.50	38.97
$1.15 \times 10^{-3}$	1	44.26	11.82	18.73	45.26	12.00	19.05
	3	60.53	17.38	24.91	51.28	15.00	20.78
	7	80.44	25.36	31.80	64.30	21.25	24.68
	12	100.23	34.06	38.20	80.34	29.00	29.44
	18	121.23	43.81	44.70	100.34	38.50	35.51
$1.15 \times 10^{-4}$	1	31.92	8.73	13.39	35.36	9.50	14.72
	3	47.82	14.21	19.41	40.38	12.25	16.02
	7	66.86	21.97	25.92	54.39	18.75	20.35
	12	85.68	30.42	31.90	70.41	26.50	25.11
	18	107.52	40.38	38.76	88.42	35.50	30.31
$1.15 \times 10^{-5}$	1	23.50	6.63	9.74	25.44	7.00	10.39
	3	37.70	11.68	15.03	32.45	10.25	12.56
	7	56.80	19.45	21.56	44.42	16.24	16.00
	12	76.27	28.07	27.83	60.48	24.00	20.78
	18	96.80	37.70	34.12	78.50	33.00	25.98



**Figures 5.5** Peak and residual shear stresses as a function of normal stress for granite

(a), sandstone (b) and marl (c).

#### 5.1.4 Fracture dilation

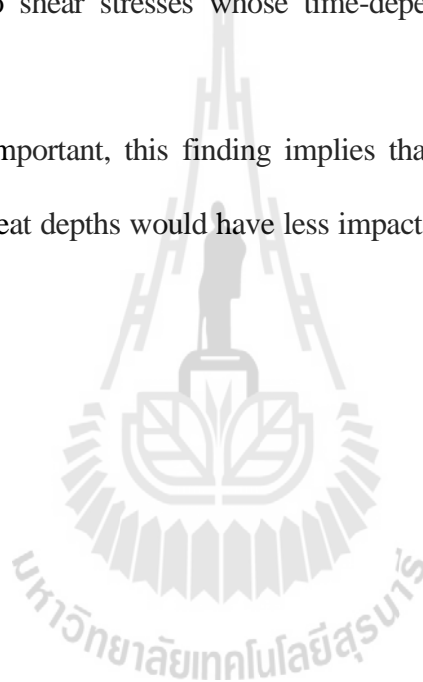
Dilation is the normal separation of the fractures walls, induced by the shearing movement of the fracture. The amount of dilation is governed by the fracture roughness, joint wall strength and the applied normal stresses. Here an assessment of the shear velocity effect on the fracture dilation has been made. In principle the normal and shear displacements of the triaxial shear test as performed in this study can be calculated from the relative vertical and lateral displacements of the two wedge blocks. Figures 5.6 through 5.8 shows the lateral-axial displacement ( $d_3-d_1$ ) curves monitored during the test. Using Eqs. (4.3) and (4.4) the normal and shear displacements of the tested fractures can be calculated, as shown in Figures 5.9 through 5.11. The effects of the confining stress (or normal stress) and shear velocity can be revealed from the  $d_3-d_1$  diagrams (Figures 5.6 through 5.8) and from the  $d_n-d_s$  diagrams (Figures 5.9 through 5.11).

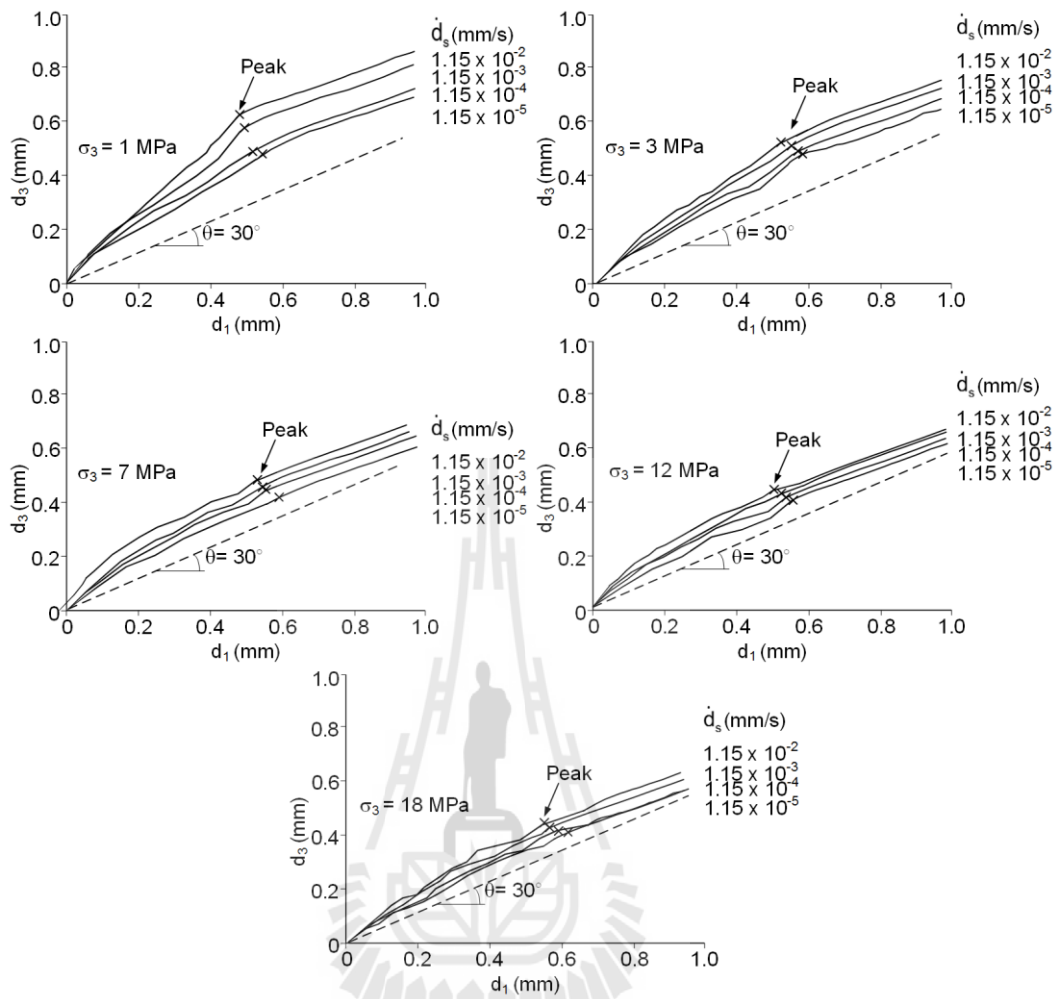
For all rock types and shear velocities the dilations tend to increase with the shearing displacement ( $d_3$ ) until the peak stresses have been reached. After the peak the dilations tend to remain constant. The angle ( $\theta$ ) in Figure 5.6 through 5.8 represents the angle between the applied major principal (axial) stresses and the fracture plane.

The amount of dilation significantly decreases as the confining stresses increase and the shear velocity decrease. This holds true for all rock types even with different JRC values. The fractures with larger JRC values (granite) however tend to show larger dilation, as compared to those with the smaller JRC values (sandstone and marl), particularly under low confining stresses. This is presumably because the joint walls climb over the asperities while shearing under low confining stresses. They however tends to shear through the asperities under high confining stresses. As a result the higher or steeper asperities of the high JRC fractures (granite - Figures 5.6 and 5.9)

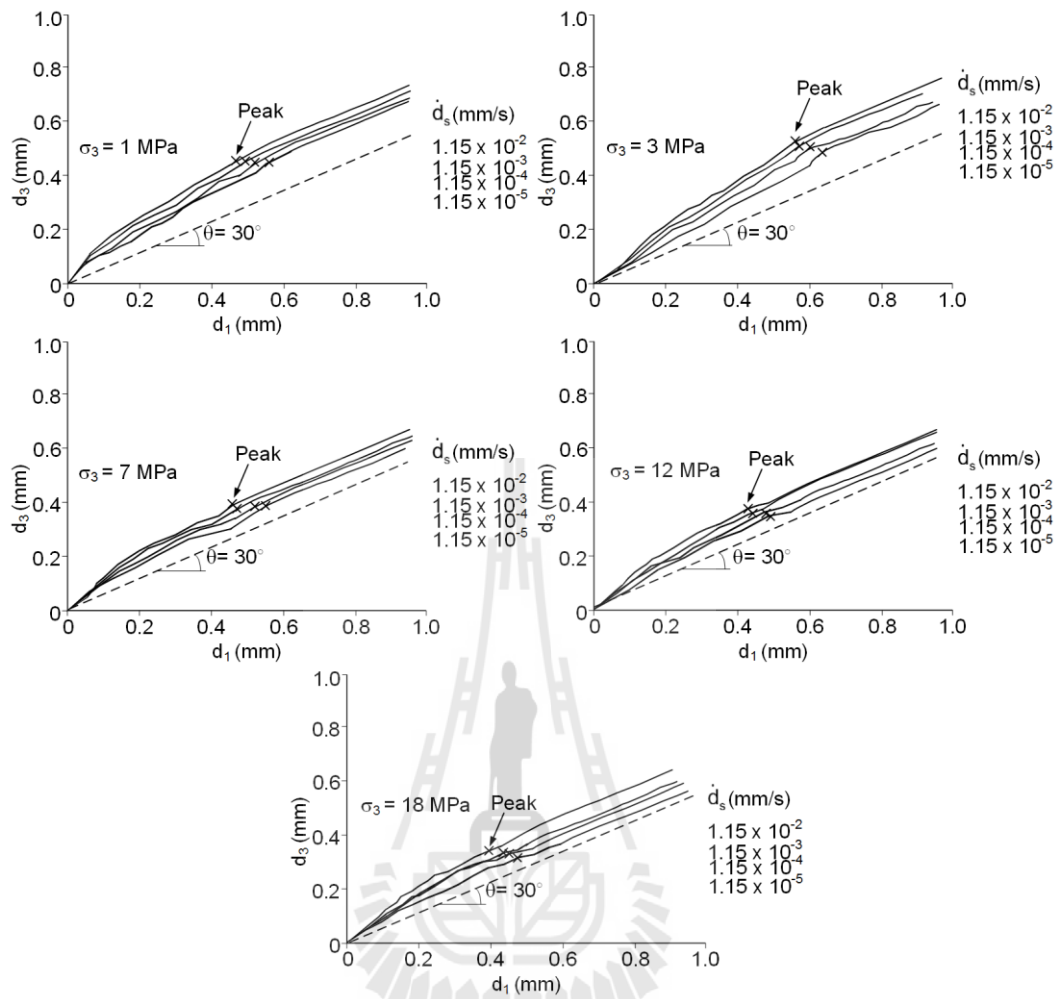
will yield larger dilation, as compared to those with the smaller asperities or low JRC fractures (sandstone and marl – Figures 5.7, 5.8, 5.10 and 5.11). The effects of the shear velocity act more on the low confining stress fractures than on the high confining stress ones. This could be explained by the fact that under high confining stresses most asperities would be sheared off during shearing, and hence the time-dependent strength of the asperities is diminished. On the other hand under low confining stresses the asperities would be subjected to shear stresses whose time-dependency can be revealed more clearly.

More important, this finding implies that the relative displacements of fractures or faults at great depths would have less impact from the shear velocity in term of the fracture dilation.

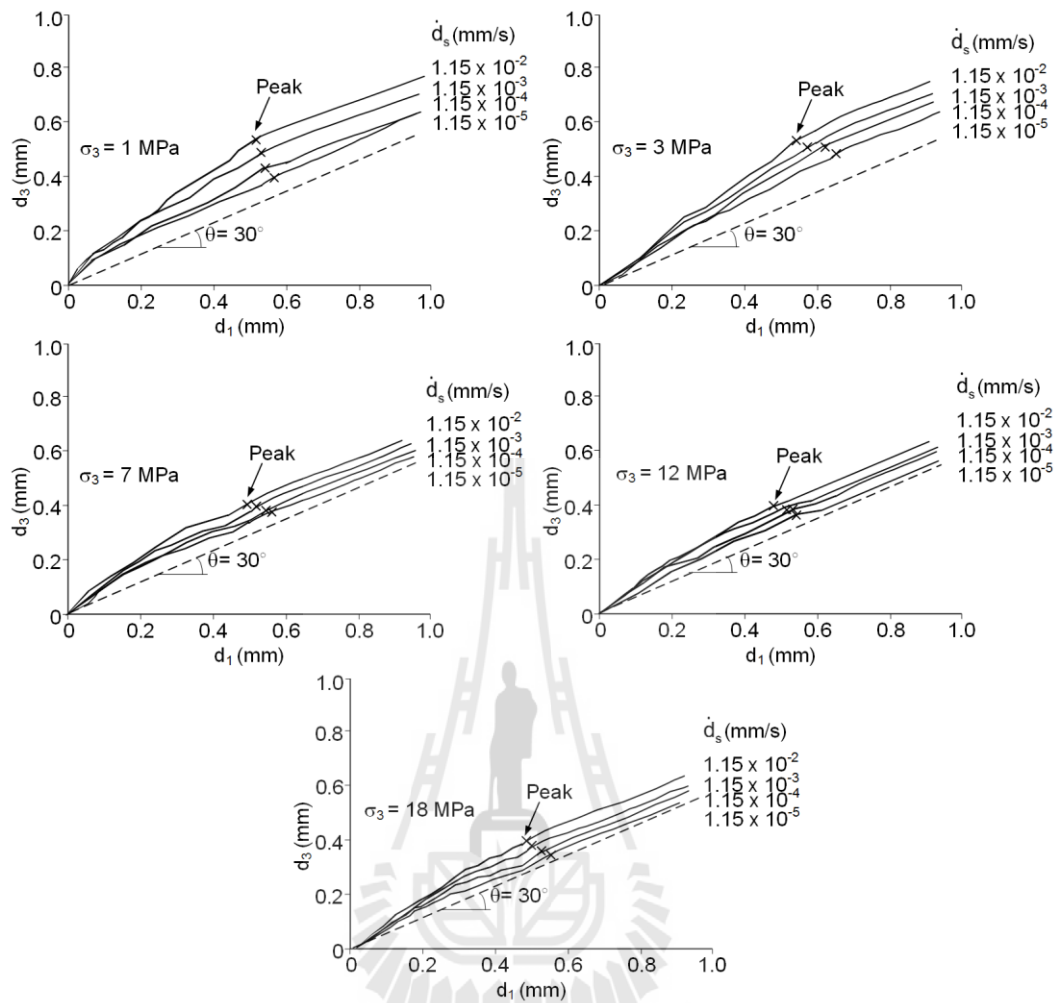




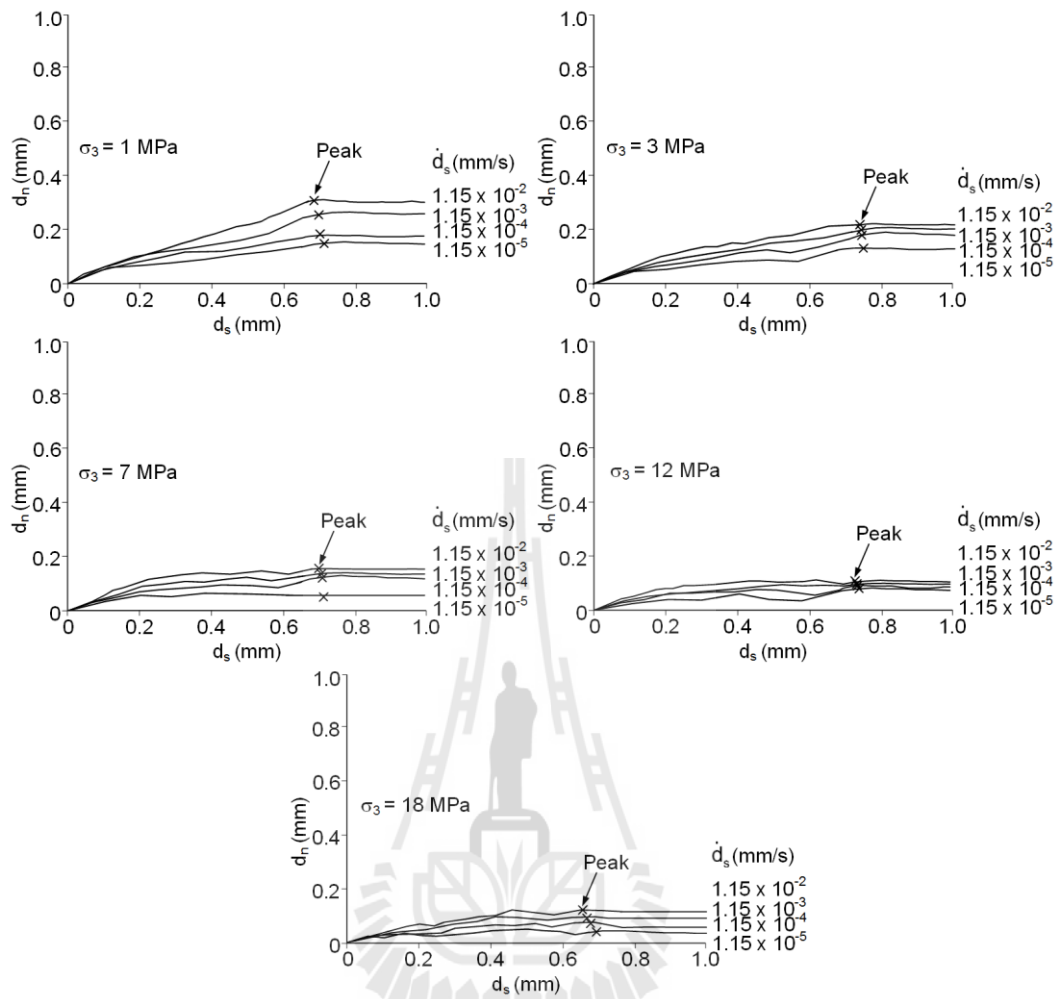
**Figures 5.6** Lateral-axial displacement ( $d_3$ - $d_1$ ) curves of tension-induced fractures for granite. Angle  $\theta$  represents the angle between axial direction ( $d_1$ ) and fracture plane ( $d_s$ ) used in all test specimens. The cross signs ( $\times$ ) represent the dilations that correspond to the peak stress.



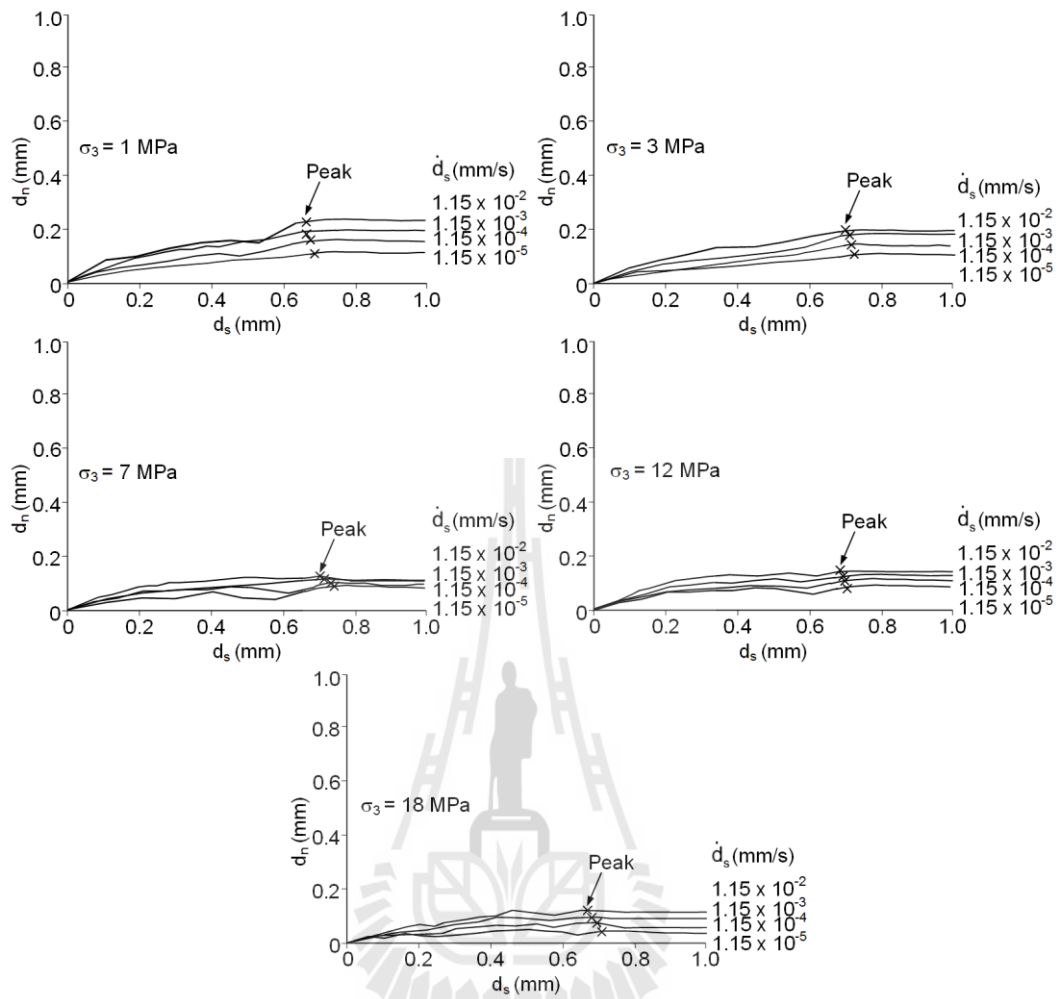
**Figures 5.7** Lateral-axial displacement ( $d_3$ - $d_1$ ) curves of tension-induced fractures for sandstone. Angle  $\theta$  represents the angle between axial direction ( $d_1$ ) and fracture plane ( $d_s$ ) used in all test specimens. The cross signs ( $\times$ ) represent the dilations that correspond to the peak stress.



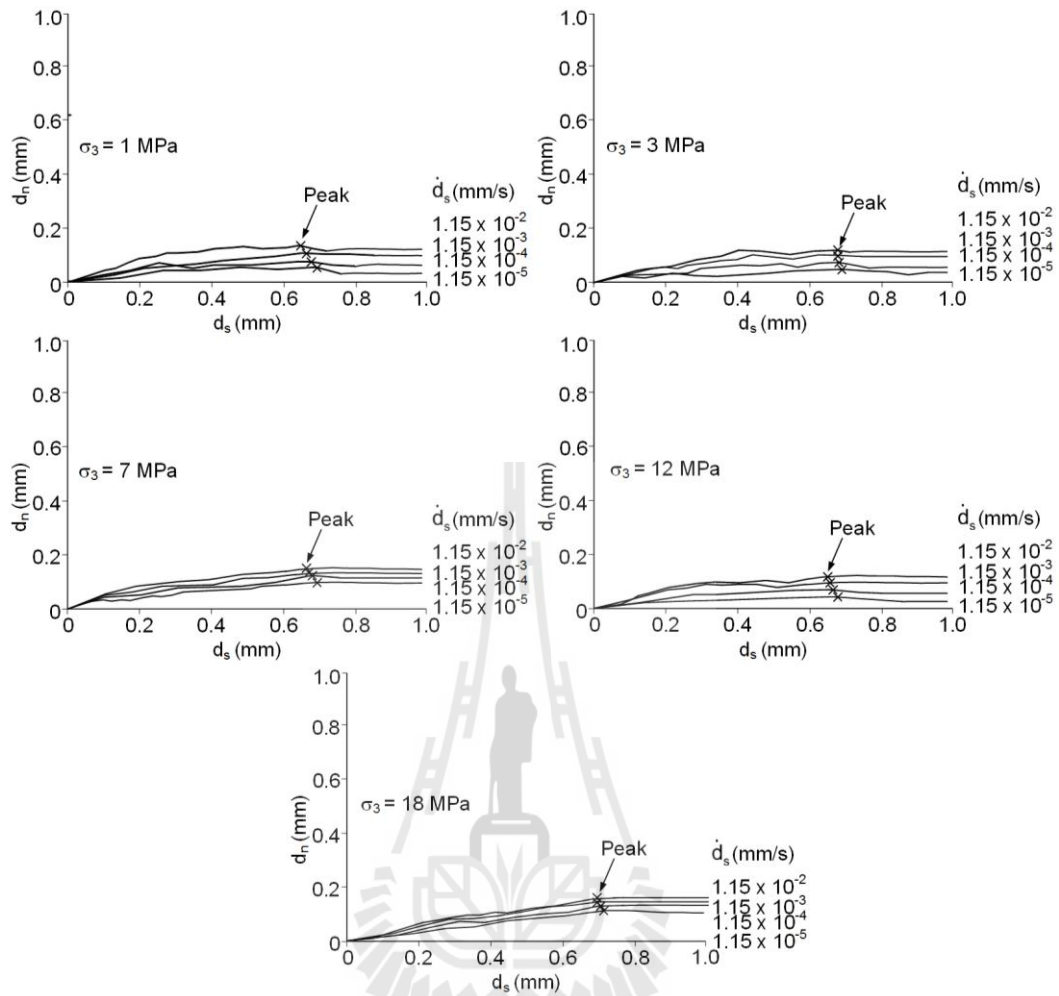
**Figures 5.8** Lateral-axial displacement ( $d_3$ - $d_1$ ) curves of tension-induced fractures for marl. Angle  $\theta$  represents the angle between axial direction ( $d_1$ ) and fracture plane ( $d_3$ ) used in all test specimens. The cross signs ( $\times$ ) represent the dilations that correspond to the peak stress.



**Figures 5.9** Normal displacement ( $d_n$ ) as a function of the shear displacement ( $d_s$ ) for granite. The cross signs ( $\times$ ) represent the dilations that correspond to the peak stress.



**Figures 5.10** Normal displacement ( $d_n$ ) as a function of the shear displacement ( $d_s$ ) for sandstone. The cross signs ( $\times$ ) represent the dilations that correspond to the peak stress.



**Figures 5.11** Normal displacement ( $d_n$ ) as a function of the shear displacement ( $d_s$ ) for marl. The cross signs ( $\times$ ) represent the dilations that correspond to the peak stress.

### 5.1.5 Post-test observations

Post-test fractures have been examined in attempt to qualitatively correlate the sheared-off areas with the confining stresses and shear velocities. A difficulty arises for this task. The post-test fractures are obscured by the deposition of the rock powder (gouges) resulting from the crushing of the asperities. Figure 5.12 shows some examples of the post-test fractures in the three tested rock types, for the highest and lowest shear velocities and confining stresses. In the figure the light areas represent the sheared-off asperities with slight amount of gouge deposition. The post-test specimens have usually been broken around the edges. Obtaining the laser scan results along the same profile as that obtained before testing is virtually impossible. This makes more difficult by the relatively poor precision of the setting procedure of the available surface scanner. Nevertheless, some conclusions can be drawn. As expected, the increase of the confining stresses significantly increase the sheared-off areas for all rock types. The reduction of the shear velocity also increase the sheared-off areas, particularly under large confining stresses. These agree reasonably well with the fracture dilation measured during the test (Figures 5.6 to 5.8) that both confining stresses and reduction of the shear velocity can clearly minimize the amount of dilation which results in an increase of the amount of the sheared asperities.

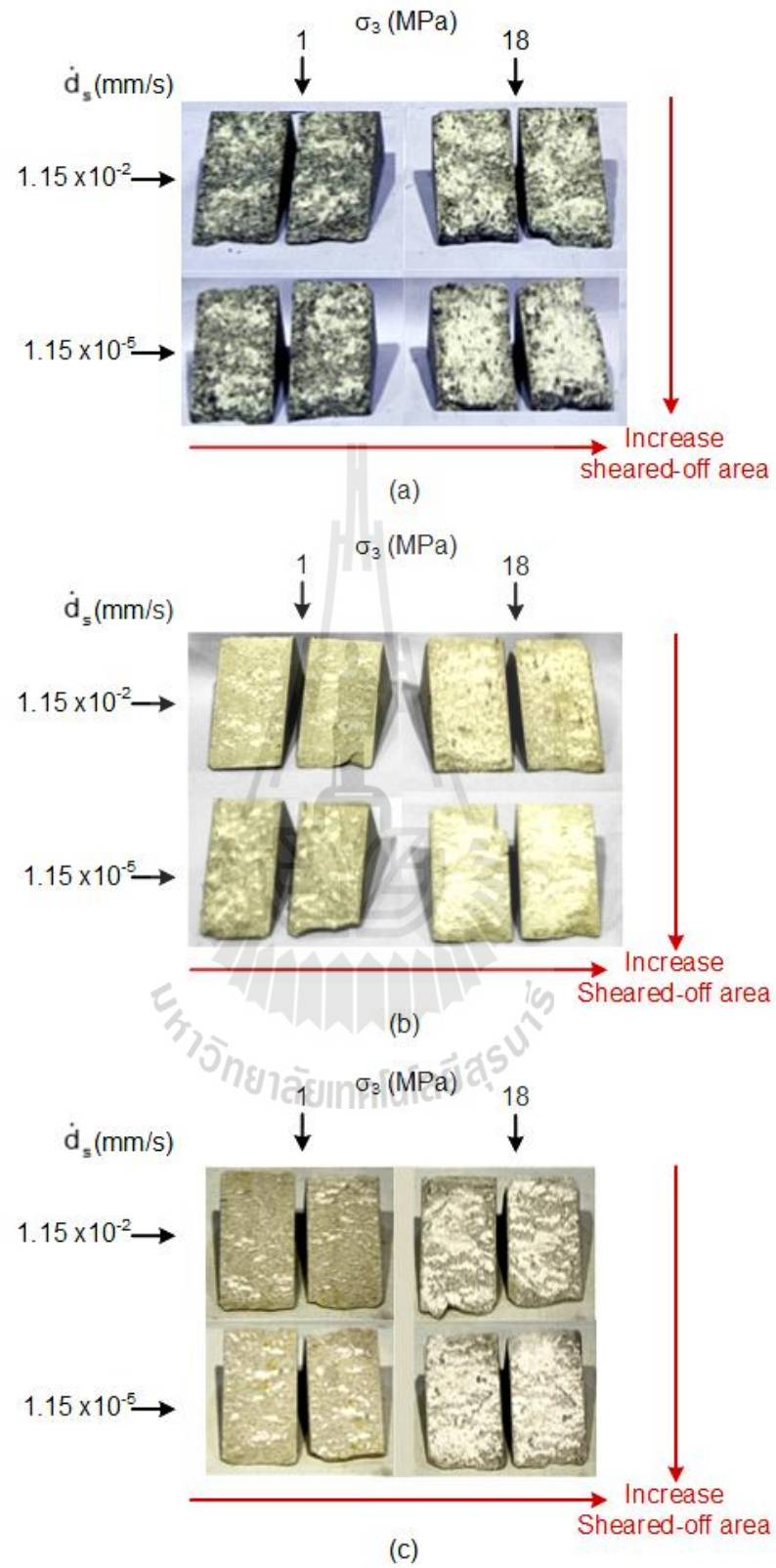


**Figure 5.12** Some post-test fractures of granite (a), sandstone (b) and marl (c).

## 5.2 Triaxial shear tests on smooth saw-cut surfaces

For this test series the shear strengths of smooth saw-cut surfaces are determined under the confining pressures of 1, 7, and 12 MPa with shear velocity varying from  $1.15 \times 10^{-5}$  to  $1.15 \times 10^{-2}$  mm/s. The test procedure and calculation method are identical to those of the tension-induced fractures. For the smooth saw-cut surface the Coulomb's criterion is used to represent the peak shear strengths under various shear velocities and confinements:

$$\tau = \sigma_n \cdot \tan (\phi^*) + c^* \quad (5.1)$$

where  $\phi^*$  and  $c^*$  are defined here as the apparent friction angle and apparent cohesion of the saw-cut surfaces. This is primarily to avoid confusing with the fracture cohesion ( $c$ ) and friction angle ( $\phi$ ) conventionally obtained from the direct shear test with constant normal stress. Table 5.4 summarizes the shear strength results of smooth saw-cut surfaces for the three rock types. The shear stress ( $\tau$ ) and normal stress ( $\sigma_n$ ) are calculated from the major principal ( $\sigma_1$ ) and confining ( $\sigma_3$ ) stresses, using Eqs. (4.1) and (4.2). The above equation (5.1) is fitted to the test results in the forms of  $\tau$ - $\sigma_n$  diagrams in Figure 5.13. The basic friction angle for granite, sandstone and marl are determined as  $30^\circ$ ,  $33^\circ$  and  $31^\circ$ , and the cohesions are 1.37, 1.49 and 1.23, respectively. The diagrams suggest that the shearing resistances for the smooth surfaces of the three rock types tend to be independent of the shear velocities  $\dot{d}_g$ , as evidenced by the similar values of  $\phi^*$  and  $c^*$  obtained under different shear velocities (Figure 5.13). In another word the effect of shear velocity on the fracture strength only pronounces on the rough fractures.

**Table 5.4** Summary of peak shear strengths and their corresponding normal stresses for smooth saw-cut surfaces.

$\dot{d}_s$ (mm/s)	$\sigma_3$ (MPa)	Granite			Sandstone			Marl		
		$\sigma_1$ (MPa)	$\sigma_n$ (MPa)	$\tau$ (MPa)	$\sigma_1$ (MPa)	$\sigma_n$ (MPa)	$\tau$ (MPa)	$\sigma_1$ (MPa)	$\sigma_n$ (MPa)	$\tau$ (MPa)
$1.15 \times 10^{-2}$	1	8.23	2.81	3.13	9.41	3.10	4.46	8.57	2.89	3.28
	3	30.91	15.81	9.45	45.36	15.34	14.44	35.28	11.82	10.08
	7	41.83	21.25	15.08	46.03	24.51	20.74	43.01	20.15	14.14
$1.15 \times 10^{-3}$	1	7.39	2.60	2.77	9.24	3.06	4.57	8.23	2.81	3.13
	3	30.11	15.01	8.53	44.56	14.54	13.64	34.48	11.62	9.98
	7	41.16	19.29	12.63	45.86	24.58	20.66	43.68	20.92	14.72
$1.15 \times 10^{-4}$	1	7.04	3.75	2.52	10.02	4.36	5.34	8.01	3.12	3.05
	3	29.82	14.32	7.49	43.82	14.67	12.75	34.31	11.93	9.89
	7	41.53	18.75	13.85	45.11	2.53	19.83	44.03	20.25	15.37



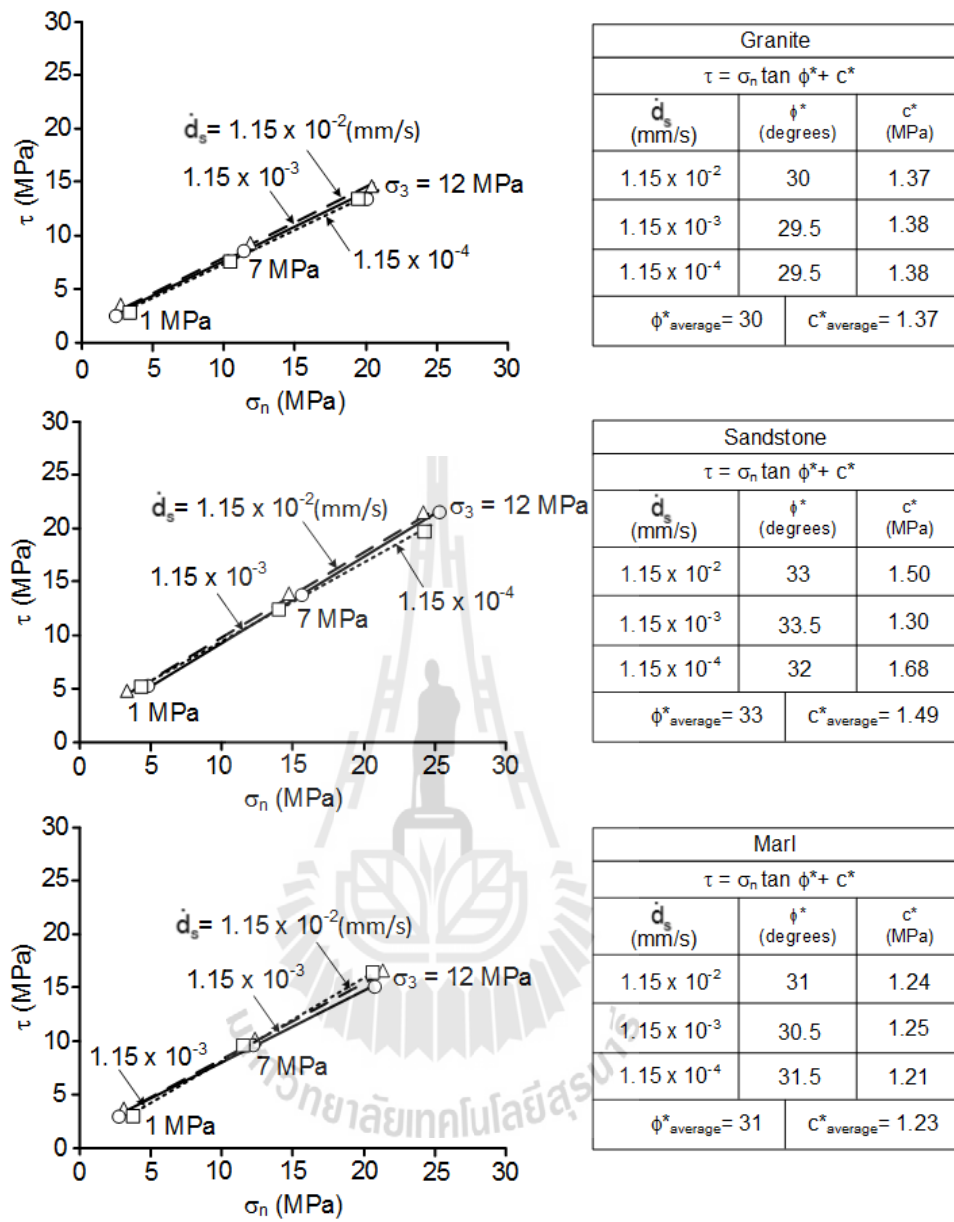


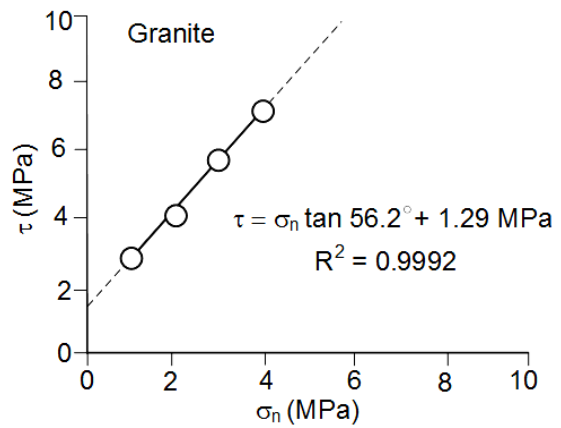
**Figure 5.13** Shear strengths of smooth saw-cut surfaces.

### 5.3 Direct shear tests on tension-induced fractures

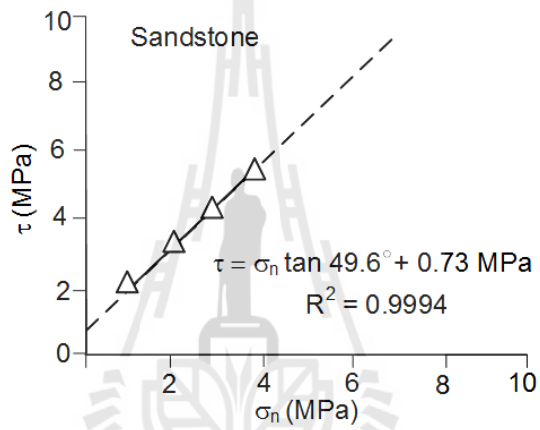
This test series involves the direct shear tests performed on the tension-induced fractures for the three rock types. The primary objective is to provide the shear strength results under the conventional method. The results will later be compared with those of the triaxial shear tests. The test method and calculation used here are in accordance with the ASTM (5607-08) standard practice. The fracture areas are  $100 \times 50 \text{ mm}^2$  which are similar to those of the triaxial shear testing. The normal stresses are 1, 2, 3 and 4 MPa with a constant shearing rate of  $2.5 \times 10^{-3} \text{ mm/s}$ . Table 5.5 summarizes the shear strength results. Figure 5.14 shows the peak shear stresses of the three rock types as a function of normal stress. The friction angle of the fractures ( $\phi$ ) for granite, sandstone and marl are  $56.2^\circ$ ,  $49.6^\circ$  and  $47.6^\circ$ , and the cohesions are 1.29, 0.73 and 0.47, respectively. Post-test observations of the sheared fractures suggest that the higher normal stresses are applied, that larger sheared areas are obtained, as shown in Figure 5.16. These findings are similar to those of the triaxial shear test specimens.

**Table 5.5** Summary of peak and residual shear strengths and their corresponding normal stresses of direct shear tests.

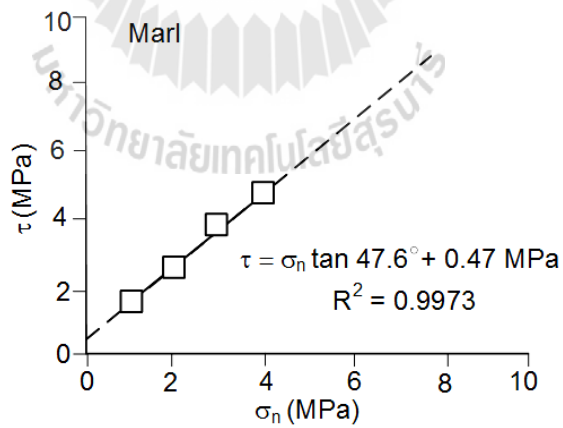
Granite			Sandstone			Marl		
$\sigma_{n, \text{ peak}}$ (MPa)	$\tau_{\text{ peak}}$ (MPa)	$\tau_{\text{ residual}}$ (MPa)	$\sigma_{n, \text{ peak}}$ (MPa)	$\tau_{\text{ peak}}$ (MPa)	$\tau_{\text{ residual}}$ (MPa)	$\sigma_{n, \text{ peak}}$ (MPa)	$\tau_{\text{ peak}}$ (MPa)	$\tau_{\text{ residual}}$ (MPa)
1	2.81	1.79	1	1.89	1.32	1	1.52	1.12
2	4.21	2.60	2	3.12	2.14	2	2.67	1.94
3	5.82	3.68	3	4.21	3.07	3	3.85	2.87
4	7.25	4.7	4	5.44	4.04	4	4.78	3.84



(a)



(b)



(c)

**Figure 5.14** Peak shear stresses as a function of normal stress for granite (a), sandstone (b) and marl (c).

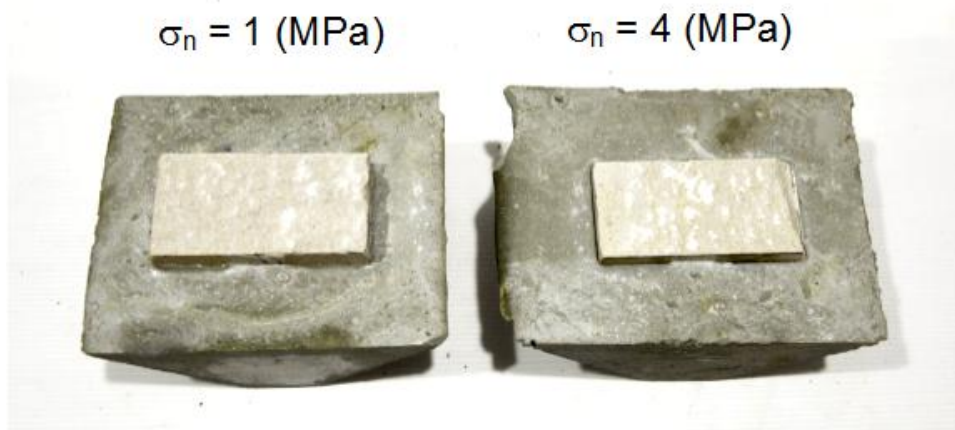


**Figure 5.15** Some post-test fractures of sandstone for the direct shear tests.



# CHAPTER VI

## SHEAR STRENGTH CRITERIA

### 6.1 Introduction

An attempt has been made to derive strength criteria that can explicitly the effects of confining pressures and shear velocities. Such criteria would be useful for the prediction of fracture shear strengths under the boundary conditions ( $\sigma_3$  and  $\dot{d}_s$ ) beyond those used in this study. This chapter describes the normalization of the shear displacement rate, derivative of the strength criteria for peak and residual regions, and verification of the proposed criteria by predicting the direct shear test results under no confining stress ( $\sigma_3=0$ ).

### 6.2 Normalization of shear displacement rate

The rate of shear displacements or shear velocity ( $\dot{d}_s$ ) that are equivalent to axial displacement rate ( $\dot{d}_1$ ) can be calculated using Eq. (4.3) as  $1.15 \times 10^{-5}$  to  $1.15 \times 10^{-2}$  mm/s. The ISRM suggested method (Muralha et al., 2013) specifies the shear velocity of the shear strength tests on rock fracture specimens in laboratory around 0.1–0.2 mm/minute ( $2.5 \times 10^{-3}$  mm/s) which are usually suitable for most conditions. To compare the strength results obtained under various shear rates with those of the ISRM suggested method. The defined shear velocities must be normalized to isolate the shear velocity effect. The normalization of shear velocity can be made by dividing the " $\dot{d}_s$ " by shear velocity defined from the ISRM suggested

method ( $2.5 \times 10^{-3}$  mm/s). The ratio of the shear velocity obtained in this study to the shear velocity defined from ISRM standard is designated as  $\dot{d}_s^*$ . Table 6.1 summarizes the normalized shear velocity results. These normalized values will be later used in the following section.

**Table 6.1** Summary of the normalize shear velocities.

$\dot{d}_1$ (mm/s)	$\dot{d}_s$ (mm/s)	$\dot{d}_s^*$
$1.0 \times 10^{-2}$	$1.15 \times 10^{-2}$	4.62
$1.0 \times 10^{-3}$	$1.15 \times 10^{-3}$	$4.62 \times 10^{-1}$
$1.0 \times 10^{-4}$	$1.15 \times 10^{-4}$	$4.62 \times 10^{-2}$
$1.0 \times 10^{-5}$	$1.15 \times 10^{-5}$	$4.62 \times 10^{-3}$

### 6.3 Criterion for peak shear strength

The test results from Chapter V indicate that the major principal stresses at peak shear strength under various shear velocities increase with confining stresses (Figure 5.4). The non-linear behavior of the fracture is reflected as a curvature of the major principal-confining stresses relation. An empirical equation is proposed to predict the major principal stresses at peak shear strength as a function of confining stresses:

$$\sigma_{1, \text{peak}} = A + \eta \sigma_3^\kappa \quad (6.1)$$

where  $\sigma_{1, \text{peak}}$  is the major principal stresses at peak,  $A$ ,  $\eta$  and  $\kappa$  are empirical constants. Regressions analysis is performed to determine these parameters from the test data. Table 6.2 summarizes the results. Good correlation is obtained ( $R^2 > 0.9$ ). The constants  $\eta$  and  $\kappa$  for each rock types tend to be independent of shear velocity.

The constant A represents intercept on  $\sigma_{1, \text{peak}}$  axis when the confining pressure is zero. After several trials the increased of the constant A with the shear velocity can be best described by a logarithmic equation:

$$A = \alpha + \lambda \ln(\dot{d}_s^*) \quad (6.2)$$

where  $\alpha$  and  $\lambda$  are empirical constants, and  $\dot{d}_s^*$  is the normalized shear velocity. Substituting Eq. (6.2) into (6.1) the major principal stresses at peak shear strength as a function of confining stresses under various shear velocities can be obtained:

$$\sigma_{1, \text{peak}} = \alpha + \lambda \ln(\dot{d}_s^*) + \eta \sigma_3^k \quad (6.3)$$

For the three rock types these constants can be defined by the regression analysis as shown in Table 6.3. Figure. 6.1 fits the major principal stresses at peak shear strength results with the proposed criterion (Eq. (6.3)). Good correlations are obtained ( $R^2 > 0.9$ ). The shear velocity that complies with the ISRM suggested method is also incorporated the figure for comparison ( $\dot{d}_s^* = 1 \text{mm/s}$ ).

From Eqs. (4.1) and (4.2) the proposed peak shear strength criteria can be presented in forms of  $\tau_{\text{peak}}$  and  $\sigma_{n, \text{peak}}$  as follows:

$$\tau_{\text{peak}} = \frac{1}{2} [(\alpha + \lambda \ln(\dot{d}_s^*) + \eta \sigma_3^k) - \sigma_3] \cdot \sin 2\beta \quad (6.4)$$

$$\begin{aligned} \sigma_{n, \text{peak}} = & \frac{1}{2} [(\alpha + \lambda \ln(\dot{d}_s^*) + \eta \sigma_3^k) + \sigma_3] \\ & + \frac{1}{2} [(\alpha + \lambda \ln(\dot{d}_s^*) + \eta \sigma_3^k) - \sigma_3] \cdot \cos 2\beta \end{aligned} \quad (6.5)$$

Figure 6.2 compares the test results with the peak strength criterion in forms of  $\tau_{\text{peak}}-\sigma_{n, \text{peak}}$  diagrams. The criterion agrees well with the test results. The figures show the upper and lower bounds of the peak shear strength that can be obtained from the triaxial shear test method. The upper bound is defined by the angle between the normal of fracture and the axial direction which is maintained constant at 60 degrees for all specimens. The lower bound is defined as the basic friction angle obtained from smooth saw-cut surfaces testing.

**Table 6.2** Empirical constants A,  $\eta$  and  $\kappa$ .

$\sigma_{1, \text{peak}} = A + \eta \sigma_3^\kappa$					
Rock Types	$d_s^*$	A	$\eta$	$\kappa$	$R^2$
Granite	4.62	72.39	10.32	0.77	0.999
	$4.62 \times 10^{-1}$	57.01	8.83	0.79	0.999
	$4.62 \times 10^{-2}$	35.80	11.23	0.72	0.994
	$4.62 \times 10^{-3}$	25.42	8.61	0.77	0.999
Sandstone	4.62	12.44	28.87	0.51	0.998
	$4.62 \times 10^{-1}$	10.11	23.81	0.51	0.999
	$4.62 \times 10^{-2}$	5.39	25.88	0.53	0.999
	$4.62 \times 10^{-3}$	4.10	19.84	0.58	0.999
Marl	4.62	24.62	17.04	0.65	0.999
	$4.62 \times 10^{-1}$	18.65	16.74	0.63	0.999
	$4.62 \times 10^{-2}$	13.60	15.43	0.62	0.999
	$4.62 \times 10^{-3}$	5.80	16.52	0.58	0.999

**Table 6.3** Constants  $\alpha$ ,  $\lambda$ ,  $\eta$  and  $\kappa$ .

$\sigma_{1, \text{peak}} = \alpha + \lambda \ln(\dot{d}_s^*) + \eta \sigma_3^\kappa$				
Rock Types	$\alpha$	$\lambda$	$\eta$	$\kappa$
Granite	63.19	8.06	9.71	0.76
Sandstone	45.07	5.24	14.62	0.63
Marl	35.86	5.33	14.28	0.63



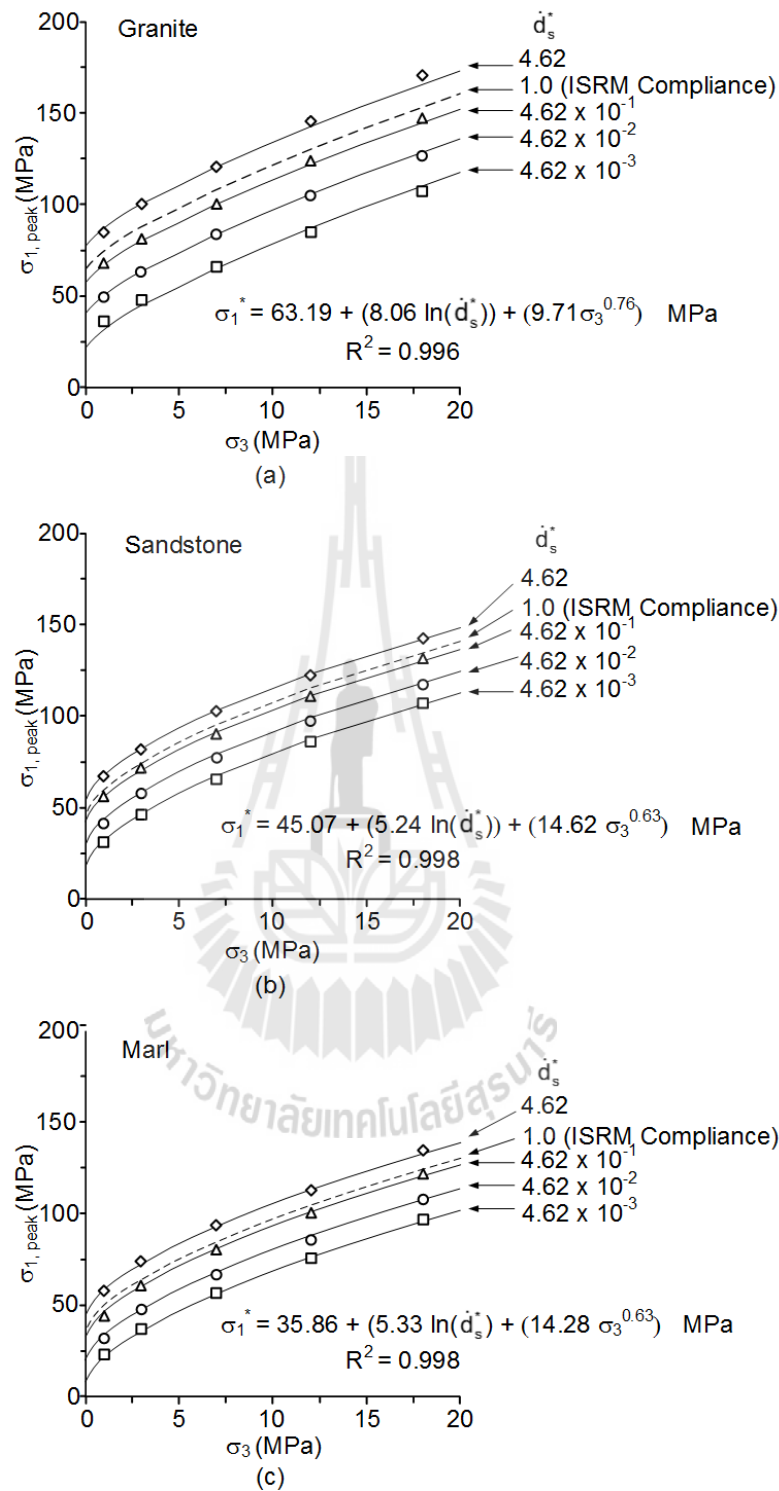


**Figure 6.1** Major principal stresses at peak shear strength as a function of confining stresses results with the strength criterion of granite (a), sandstone (b) and marl (c).

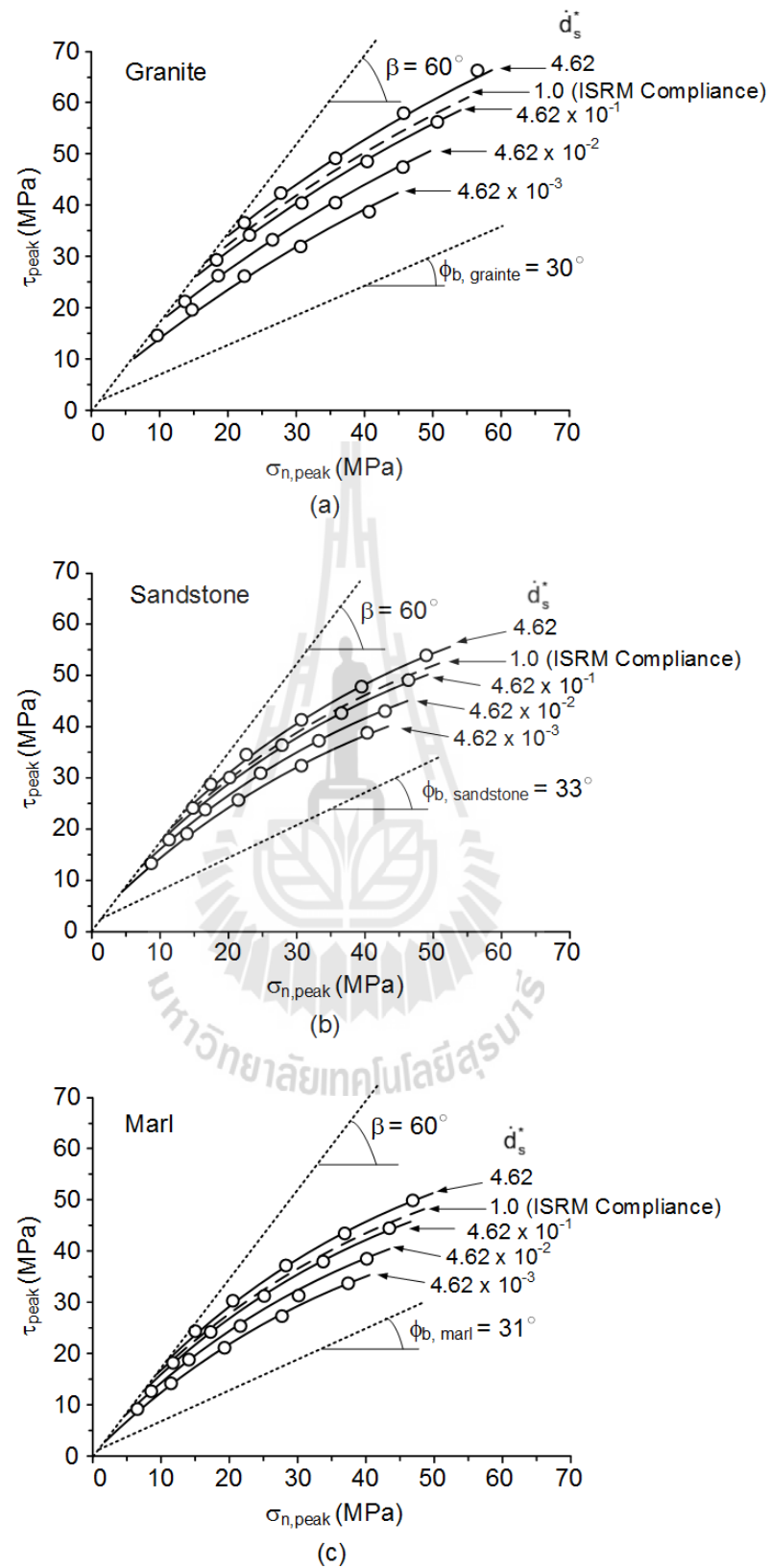


**Figure 6.2** Peak shear strength criterion compared with test data.

## 6.4 Criterion for residual shear strength

For the residual shear strength the Coulomb criterion is used to represent the residual shear strengths under various shear velocities and confinements:

$$\tau_{\text{residual}} = c^* + \sigma_n \cdot \tan(\phi^*) \quad (6.6)$$

where  $\phi^*$  and  $c^*$  are defined here as the apparent friction angle and apparent cohesion. This is primarily to avoid confusing with the fracture cohesion ( $c$ ) and friction angle ( $\phi$ ) conventionally obtained from the direct shear test with constant normal stress. The above equation is fitted to the experimental results in the forms of  $\tau$ – $\sigma_n$  diagrams in Figure 6.3. The average friction angles for granite, sandstone and marl are 32.12°, 35.03° and 33.06°, respectively. The  $\phi^*$  of the three rock types tend to be independent of the shear velocities  $\dot{d}_s^*$ , as evidenced by the similar values of  $\phi^*$  obtained under different shear velocities, while the  $c^*$  tends to increase with the shear velocity (Figure 6.3). The increasing of the  $c^*$  with the shear velocity can be best described by logarithmic equation:

$$c^* = c + m \cdot \ln(\dot{d}_s^*) \quad (6.7)$$

where  $c$  and  $m$  are empirical constants. From this equation,  $c^*$  will equal to  $c$  for the ISRM compliance shear velocity (or  $\dot{d}_s^*=1$ ). Based on the Coulomb criterion the linear law is proposed to represent the principal stresses by Jaeger (1959):

$$\sigma_1 = \left[ \frac{2 \cdot c + 2\mu\sigma_2}{(1 - \mu \cdot \cot \beta) \cdot \sin 2\beta} \right] + \sigma_3 \quad (6.8)$$

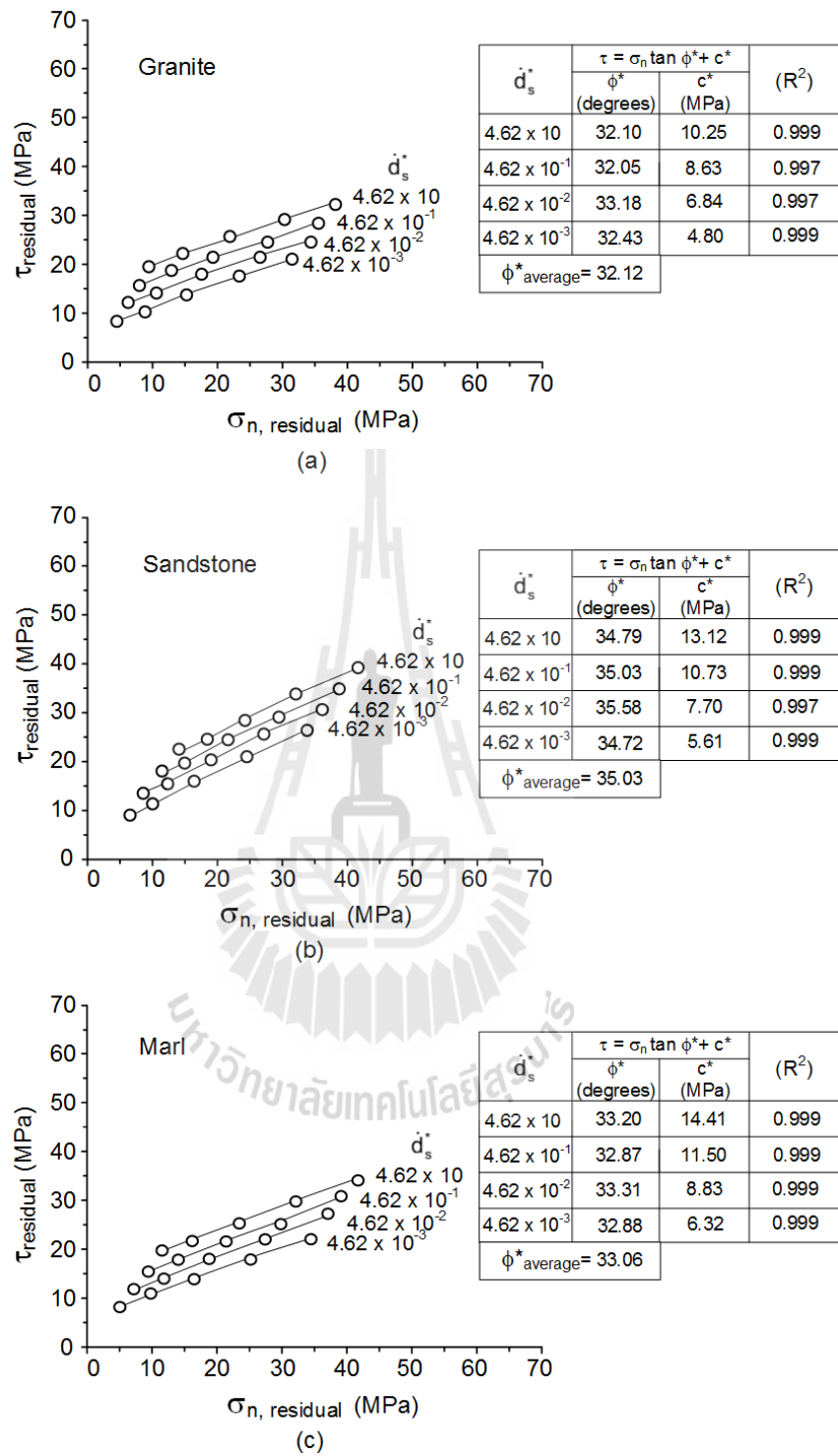


**Figure 6.3** Residual shear strengths as a function of normal stress for various shear velocities of granite (a), sandstone (b) and marl (c).

where  $c$  is the cohesion,  $\mu = \tan\phi$ , and  $\beta$  is the angle between  $\sigma_1$  and  $\sigma_n$  directions (equal  $60^\circ$ ). By substituting Eq. (6.7) into (6.8) the following relation is obtained:

$$\sigma_1 = \left[ \frac{2(c + m \cdot \ln(\dot{d}_s^*)) + 2\mu\sigma_3}{(1 - \mu \cdot \cot\beta) \cdot \sin 2\beta} \right] + \sigma_3 \quad (6.9)$$

Table 6.4 shows the empirical constants for the three rock types that can be obtained from the regression analysis.

**Table 6.4** Empirical constants  $\alpha$ ,  $\lambda$ ,  $\eta$  and  $\kappa$ .

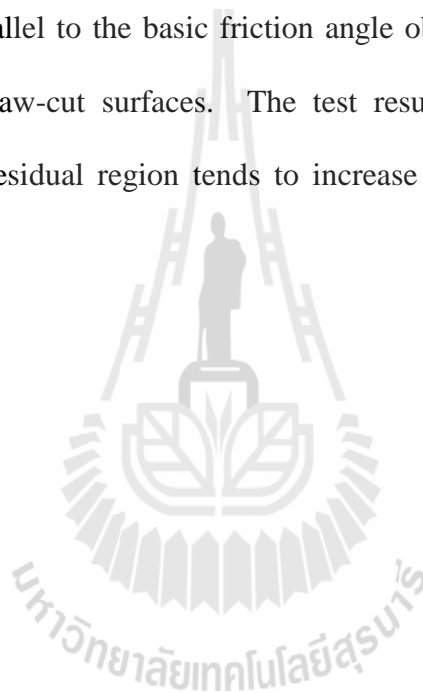
$\sigma_1 = \left[ \frac{2(c + m \cdot \ln(\dot{d}_s^*)) + 2\mu\sigma_3}{(1 - \mu \cdot \cot\beta) \cdot \sin 2\beta} \right] + \sigma_3$			
Rock Types	$c$	$m$	$\mu = \tan\phi^*$
Granite	63.19	8.06	0.63
Sandstone	45.07	5.24	0.70
Marl	35.86	5.33	0.65

From Eqs. (4.1) and (4.2) the residual shear strength criteria based on the Coulomb criteria can be presented in the forms of  $\tau_{\text{residual}}-\sigma_n$  diagrams, using the following relations:

$$\tau_{\text{residual}} = \frac{1}{2} \left[ \left[ \left( \frac{2(c + m \cdot \ln(\dot{d}_s^*)) + 2\mu\sigma_2}{(1 - \mu \cdot \cot\beta) \cdot \sin 2\beta} \right) + \sigma_3 \right] - \sigma_3 \right] \cdot \sin 2\beta \quad (6.10)$$

$$\sigma_n = \frac{\frac{1}{2} \left[ \left[ \left( \frac{2(c + m \cdot \ln(\dot{d}_s^*)) + 2\mu\sigma_2}{(1 - \mu \cdot \cot \beta) \cdot \sin 2\beta} \right) + \sigma_3 \right] + \sigma_3 \right]}{\frac{1}{2} \left[ \left[ \left( \frac{2(c + m \cdot \ln(\dot{d}_s^*)) + 2\mu\sigma_2}{(1 - \mu \cdot \cot \beta) \cdot \sin 2\beta} \right) + \sigma_3 \right] - \sigma_3 \right] \cdot \cos 2\beta} \quad (6.11)$$

Figure 6.4 compares the test results with the above residual strength criterion. The criterion agrees well with the measurements. The slope of the residual strength results tend to be parallel to the basic friction angle obtained from the triaxial shear test on the smooth saw-cut surfaces. The test results suggest that the cohesion obtained within the residual region tends to increase proportionally with the shear velocity.



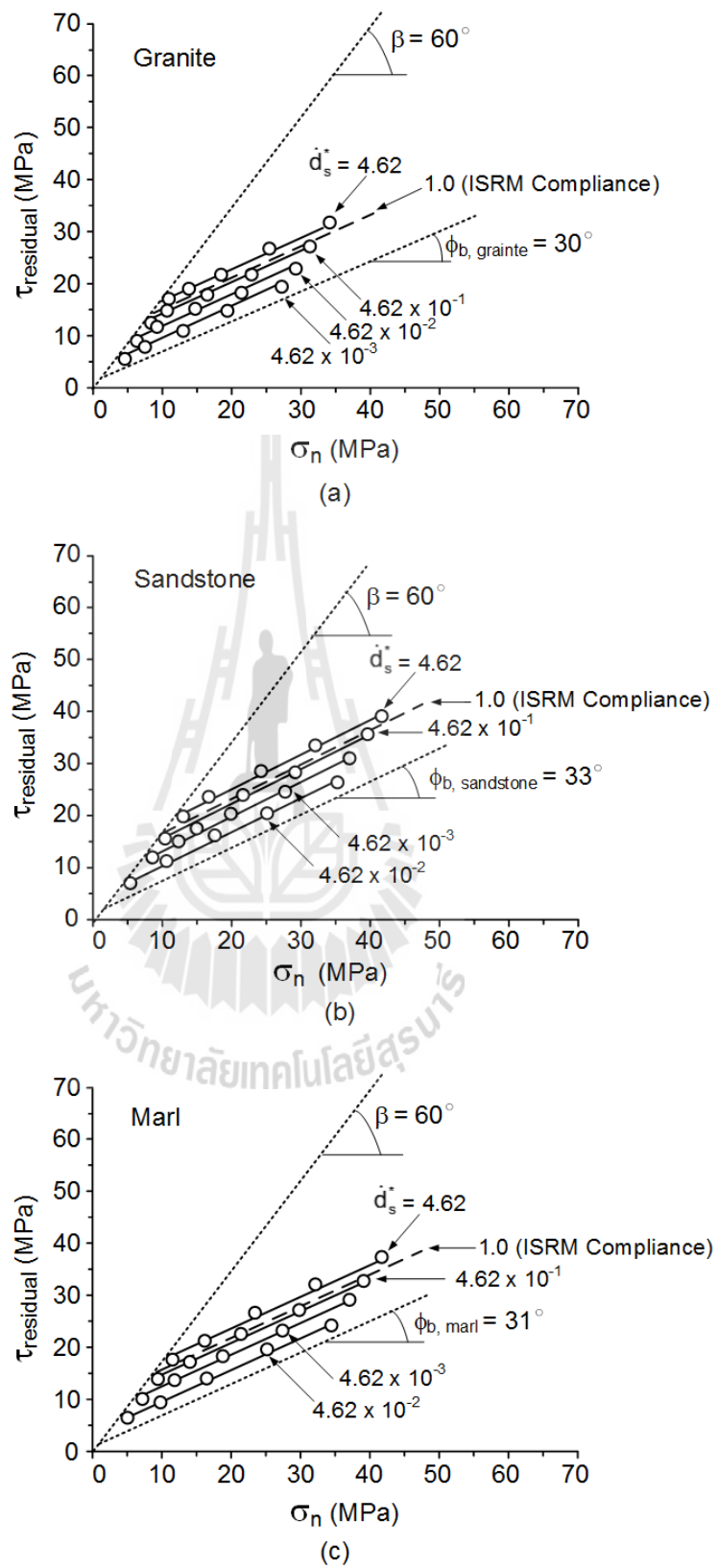


**Figure 6.4** Test results compared with residual strength criterion.

## 6.5 Verification of the proposed criterion

An attempt has been made to assess the reliability of the criterion for the triaxial peak shear strengths proposed earlier. The results of the direct shear testing in forms of the  $\tau$ - $\sigma_n$  diagrams for the tension-induced fractures are used here. To predict the fractures shear strength under no confinement as posed in the direct shear test configurations, the confining pressure ( $\sigma_3$ ) in the proposed shear strength criterion is set to zero. Comparisons of the predications with the actual direct shear test results are shown in Figure 6.5. They suggest that the predictions by the proposed triaxial shear strength criterion tend to slightly over-estimate the fracture shear strength under unconfined condition. Explanations on this discrepancy can be offered as follows:

(1) The shearing force configurations of the triaxial shear testing are different from those of the direct shear testing. The shear and normal stresses on the fractures of the triaxial shear test specimen are generated by the transforming of the major principal (axial) and minor principal stresses applied to the block specimen. For the fractures in the direct shear test specimen, the shear stress is directly applied parallel to the fractures. The analysis for both cases assumes that the fractures are planar. Depending the roughness of the fractures. The loading stress concentrates at the asperities may be different between the two test configurations.

(2) The normal stress on the fractures for the triaxial shear testing is not constant during the increase of the axial stress. This is evidenced by the fact that the  $\tau$ - $\sigma_n$  curve prior to the peak point tends to bend upward as the shear stress increases. The slow rises of the normal stresses may strengthen the asperities on the fracture walls, and hence resulting in a higher shear strength, compared to that of the direct shear test results. In another word the normal stresses that correspond to the peak shear strength

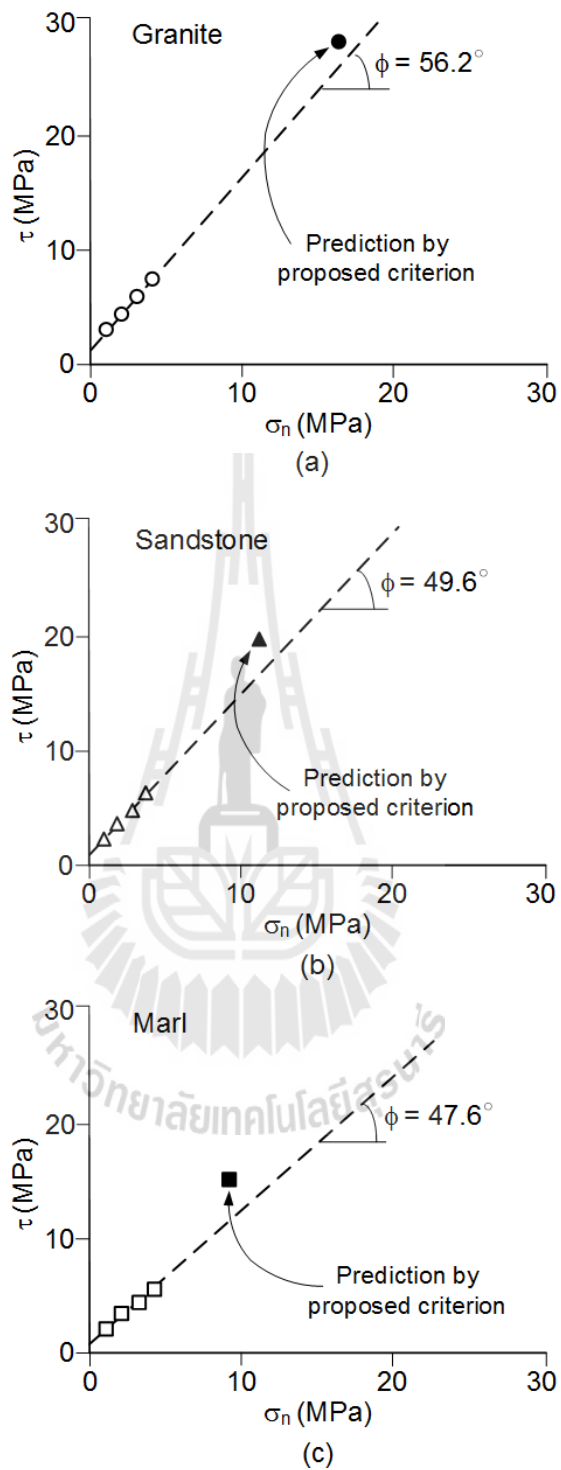


**Figure 6.5** Comparisons between direct shear test results with the prediction by proposed equation.

for the triaxial shear test condition may be lower than those of the direct shear test condition under the same peak shear stresses.

(3) The discrepancies may also be due to the fact that the data under lower  $\sigma_3$  for the triaxial shear test may not be sufficient. The power form representing the effect of  $\sigma_3$  on the shear strength of the proposed equation is statistically sensitive to the amount of the data under lower  $\sigma_3$ . The prediction above would be closer to the direct shear test results if more test data are available, particularly for the range of  $\sigma_3$  of less than 1 MPa. Due to the limitation of the cantilever beams of the poly-axial load frame such condition can not be achieved.

(4) The angle between the applied major principal stress and the fracture plane as maintained constant here at  $\beta=60^\circ$ , would also affect the triaxial shear strength when  $\sigma_3=0$ . It is believed that the discrepancy between the projection of the direct shear strength and the prediction from the triaxial shear test would be smaller if the angle  $\beta$  is larger, i.e. approaching the direct shear stress condition. In practice increasing this angle may not be a good alternative because the rock wedges on the opposite side of the fracture is likely to break during shearing, particularly under high  $\sigma_3$ . In addition preparation of the fractures (by tension-inducing method) is very difficult if the angle  $\beta$  is larger than  $60^\circ$  degrees. More discussions on the limitation of angle  $\beta$  are given in the next chapter.

# CHAPTER VII

## DISCUSSIONS, CONCLUSIONS AND RECOMMENDATIONS FOR FUTURE STUDIES

### 7.1 Discussions

This section discusses the key issues relevant to the reliability of the test schemes and the adequacies of the test results. Comparisons of the results and findings from this study with those obtained elsewhere under similar test conditions have also been made.

The angle  $\beta$  which is maintained constant at  $60^\circ$  seems to limit the lower ends of the  $\sigma_1$ - $\sigma_3$  curves and  $\tau$ - $\sigma_n$  curves for all test specimens. This angle is primarily set because it yields the length-to-width ratio of the block specimens of about 2.0. This sample shape is most suitable for the polyaxial loading device. Larger angles produce longer block specimen which can not be installed in the available device. It is recognized that if the angle  $\beta$  is larger, the applied stress condition on the triaxial shear test specimens would be closer to those of the direct shear test, and hence the prediction of the proposed criterion under  $\sigma_3=0$  would provide the shear strength results closer to the projection of the direct shear test results (see Figure 6.5). It is believed that if the angle is reduced to below  $45^\circ$  the shear sliding on the fractures may not occur, instead the compression failure of the intact rock wedge would taken place. In principle, the angle  $\beta$  should not affect the  $\sigma_1$ - $\sigma_3$  or  $\tau$ - $\sigma_n$  relations.

As evidenced by the good correlation coefficients obtained from the proposed empirical strength equation, the test results are believed to be highly reliable. This is true for all test series: triaxial shear test results on rough and smooth fractures and direct shear test results. The results obtained here agree reasonably well with those of Naphudsra and Fuenkajorn (2014) who conduct the triaxial shear test of fractures in Tak granite, and with Kapang et al. (2013) who conduct the test on fractures in Phawihan sandstone. The direct shear test results obtained here also agree with those of Kamonphet and Fuenkajorn (2013) who performs the tests on Tak granite.

It is however not intention here to claim that the proposed empirical form of the peak shear strength criterion is universally applicable to all rock types and all fracture characteristics. Different forms of the mathematical relation may be suitable for other rock types. The proposed equation however has obvious advantage that it can represent the fracture shear strengths under confinements and various shear velocities which can provide a transition to the results of the conventional direct shear test. The discrepancy between the direct shear test results and the shear strength predicted from the triaxial shear testing may partly be due to the inadequacies of the test data under low confinement, in particular in the region when  $\sigma_3$  is less than 1 MPa. In this low confinement region, based on the proposed criterion, the peak shear strength is highly sensitive to the normal stresses. The discrepancy could be minimized or eliminated if more test data in this region are available. In practice, however, due to the limitation of the available polyaxial loading device, obtaining the confining stress  $\sigma_3$  lower than 1 MPa is not possible. The test data under large confinements up to 18 MPa seem adequate and uniformly distributed.

An assessment of the effect of the degrees of the fracture roughness on the response to the shear velocity can not be made. Only one degree of roughness (JRC) is obtained from the tension-inducing method for each rock type. Nevertheless, the research findings clearly indicate that the rougher the fracture surface the more effect from the shear velocity is pronounced. This is also evidenced by that the shear strength of the smooth saw-cut surfaces is independent of the shear velocity. The granite fractures with the larger JRC values are more sensitive to the shear velocity than those with the lower JRC values in sandstone and marl.

In summary it is obvious that the triaxial shear test technique shows significant advantage over the direct shear test. It not only represents the stress condition similar to those of the in-situ condition, e.g., principal stresses across the fault or fracture plane, but also provides the shear strength results under various confining pressures. A significant finding obtained from this study is that the direct shear test results tend to overestimate the strengths of rock fractures at great depth, as demonstrated in Figures 6.2 and 6.5

## 7.2 Conclusions

All objectives and requirements of this study have been met. The results of the laboratory testing and analyses can be concluded as follows:

(1) The effect of shear velocity can be observed from  $\sigma_1$ - $\sigma_3$  and  $\tau$ - $\sigma_n$  diagrams. The lower shear velocity is applied, the lower peak and residual shear strengths are obtained. The shear strengths decrease proportionally with the decrease of the order of the shear velocity (see Figure 5.5 and Tables 5.1 through 5.3).

(2) The fractures with larger JRC values tend to be more sensitive to the shear velocity than those with lower JRC values (Figure 5.4). The shear strength of the smooth saw-cut surfaces is independent of the shear velocity (Figure 5.13).

(3) The fracture dilations measured prior to and after the peak strengths significantly decrease with increasing the confining pressures and decreasing the shear velocities. These can be observed from all rock types (Figures 5.9 through 5.11).

(4) The behavior of the fracture dilations above are supported by the post-test observations on the shear fractures that the reduction of the shear velocity notably increases the sheared-off areas on the fractures, particularly when the fractures are subject to high confining stresses (see Figure 5.12).

(5) An empirical strength criterion is proposed to describe the peak shear strength by incorporating the effects of shear velocity and confining pressure. First the magnitudes of shear velocities used in this study are normalized by that of the ISRM suggested method ( $2.5 \times 10^{-3}$  mm/s). The effect of the shear velocity is incorporated in the logarithmic form. The confining pressure effect is in the power form. The proposed equations fits well to the test results for all rock types. (see Figures 6.1 and 6.2). For the residual shear strength, the Coulomb criterion seems to be adequate to describe the increase of the shear strength with the normal stresses.

(6) The reliability of the peak shear strength criterion is assessed by predicting the shear strength under unconfined condition and comparing with the direct shear test results. They agree reasonably well. Some discrepancies are observed, which could be explained by the differences of the applied stress orientations with respect to the fracture plane between the two methods. The normal

stress for the direct shear test specimen is constant during shearing while that of the triaxial shear testing continuously increases with the shear stresses. The inadequacy of the triaxial test data under low  $\sigma_3$  (lower than 1 MPa) may be inadequate and hence resulting in an over-estimation of  $\sigma_1$  for the condition of  $\sigma_3=0$ .

(7) The triaxial shear testing technique performs here has clear advantages over the conventional direct shear tests. It allows testing or simulating the shear behavior of fractures under significantly larger confining pressures (in turn larger normal stresses) than those of the direct shear testing where it is limited by the unconfined compressive strength of the rocks. The applied stress conditions of the triaxial testing are also similar to those of the in-situ conditions where  $\sigma_1$  is the main drive to induce relative displacement of the fractures, joints or faults.

### **7.3 Recommendations for future studies**

Recognizing that the numbers of the specimens and the test parameters used here are relatively limited, more testing and measurements are recommended, as follows:

(1) The fracture areas used in this study ( $100 \times 50 \text{ mm}^2$ ) are relatively small even though they are well complied with the relevant standard practice and internationally suggested method. Testing on larger fracture areas would provide a more representative of the shear strength results when they are applied to the actual fractures under in-situ condition. The scale effect on the fracture shear strengths has also been addressed by Braton and Bandis (1980).

(2) The effects of the shear velocity would be more rigorously determined and its criterion be more accurately calibrated if lower shear displacement velocities

are applied, i.e., one or two orders of magnitude lower than those used in this study. The testing period would however be impractical to accept. The lowest shear velocity used here is  $1.15 \times 10^{-5}$  mm/s (or  $6.9 \times 10^{-4}$  mm/minute or 360 mm/year). This results in the test period of 2 days. The shear velocity with two orders of magnitude lower than this would take about 200 days (equivalent to 3.6 mm/year) to complete one fracture specimen. This would require special measurement device to monitor the displacements under such long period of testing. The results can however be a great benefit because the displacement velocity is similar to those of the actual fault movement in the north of Thailand (about 1 mm/year) (Fenton et al., 2003).

(3) It is desirable that fractures are prepared with larger angle  $\beta$ , as compared to the  $60^\circ$  used in this study. This will make the applied major principal stress aligning closer to the shear direction. As a result, the fracture shear strength obtained would be closer to those of the direct shear strength. The effect of the variation of angle  $\beta$  should also be assessed. It should be pointed out however that when the angle  $\beta$  is increased, the length-to-width ratio of the test specimen will significantly increase. This poses some difficulties for the sample preparation and testing. Note that the polyaxial loading device used here can not accommodate the block specimens with length-to-width ratio of greater than 2.5.

(4) The effects of confining pressure should be further investigated. In this study the maximum confining pressure is 18 MPa which is equivalent to the depth of about 1 km. It is well sufficient to apply the results and the proposed criterion to examine the mechanical stability of underground engineering structures where they are surrounded by the fractured rock mass. The maximum confining pressures used here may not be adequate to truly understand the mechanisms of fault movement in

the north of Thailand where the recorded epicenter is down to about 5 km depth. Such high confinement testing however can not be achieved by the polyaxial loading device used in this study. Special and high-loading device is needed for this task.

(5) It is invoked by the test results that fracture rough is a factor that is coupled with the shear velocity effect. The shear strengths of smooth fracture tend to be independent of the shear velocity. The rougher fracture surfaces, the greater effect from the shear velocity. Since the degree of roughness is limited to only one for each rock type tested here, it would be desirable to obtain shear strengths under the same shear velocity but different degrees of roughness or JRC values. This task would be very difficult to accomplish because fracture roughness obtained by tension-inducing method can not be controlled by test procedure. They are rather controlled by petrographic characteristics of the rock (e.g. grain size, mineral composition, texture, etc.). It should be also noted that comparison of the fracture shear strengths that are obtained with different JRC values and from different rock types may not be strictly valid as they may pose different joint wall strengths and shearing mechanisms.

(6) Increasing the number of the specimens would statistically enhance the reliability of the test results and the predictability of the proposed strength criterion.

(7) Performing the triaxial shear tests on a variety of rock types with different fractures, hardness and strengths would improve our understanding of the shear velocity effect on the fracture shear strength. In particular the fractures prepared in time-dependent rock would reveal the time-dependent strengths of the fracture rock wall as affected by the shear velocity. The knowledge on how the plastic or time-dependent rock wall fractures respond to the shear velocity would be benefit to understand the fault behavior at great depth.

(8) A high precision laser scanner system is needed to obtain the fracture profiles prior to and after shearing (preferable in 3-dimension). Care however should be taken to ensure that the line scanning in 2-dimension or the 3-dimensional images of the fractures prior to and after shearing can be precisely overlain to examine the alteration of the fracture surfaces due to shearing under various conditions.

(9) If the (#8) task can be accomplished, the magnitude of the potential energy required to shear-off the asperities under different shear velocities can be determined, and hence a new shear strength criterion based on the energy concept can be derived.



## REFERENCES

- ASTM C170/C170M-09, 1999. Standard test method for compressive strength of dimension stone. **Annual Book of ASTM Standards**, PA: American Society for Testing and Materials.
- ASTM D3967 Standard test method for splitting tensile strength of intact rock core specimens (Brazilian Method). **Annual Book of ASTM Standards**. West Conshohocken, PA: American Society for Testing and Materials.
- ASTM D5607-08. Standard test method for performing laboratory direct shear strength tests of rock specimens under constant normal force. **Annual Book of ASTM Standards**, Vol. 04.08. West Conshohocken, PA: American Society for Testing and Materials.
- Babanouri, N., Nasab, S.K., Baghbanan, A., Mohamadi, H.R. (2011). Over-consolidation effect on shear behavior of rock joints. **International Journal of Rock Mechanics & Mining Sciences** 48 (8): 1283-1291.
- Barton, N. (1967). The shear strength of rock and rock joint. **International Journal of Rock Mechanics and Mining Sciences & Geomech. Abstract** 13(10): 1-24.
- Barton, N. (1982). Characterizing rock masses to improve excavation design. Panel Report, Theme II Tunnelling and Excavation. **Proceedings of 4th Congress IAEG**, New Delhi.

- Barton, N. (2013). Shear strength criteria for rock, rock joints, rockfill and rock masses: Problems and some solutions. **Journal of Rock Mechanics and Geotechnical Engineering** 5(4): 249-261.
- Barton, N. and Choubey, V. (1977). The shear strength of rock joint in theory and practice. **Rock Mech** 10(1-2): 1-54.
- Barton, N.R. (1973). Review of a new shear strength criterion for rock joint deformation. **Engineering Geology** 7: 287-332.
- Boonsener, M. and Sonpiron, K. (1997). Correlation of tertiary rocks in northeast, Thailand. **Proceedings of International Conference on Stratigraphy and Tectonic Evolution of Southeast Asia and the South Pacific**, Bangkok, Thailand.
- Brady, B. H. G. and Brown, E. T. (2006). **Rock Mechanics for Underground Mining**, 3rd edition. Springer, Netherlands.
- Bunopas, S. (1992). Regional stratigraphic correlation in Thailand. In: **Proceedings of National Conference on Geological Resources of Thailand: Potential for Future Development**, Department of mineral Resources, Bangkok, Thailand.
- Chokchai, B. and Fuenkajorn, K. (2013). Effects of loading rate on joint shear strength in sandstones. **Proceeding of the Fourth Thailand Symposium on Rock Mechanics**, January 24-25, 2013, Im Poo Hill Resort, Nakhon Ratchasima, Thailand, Published by Geomechanics Research Unit, Suranaree University of Technology, Nakhon Ratchasima.

- Crawford, A. M. and Currant, J. H. (1981). The influence of shear velocity on the frictional resistance of rock discontinuities. **International Journal of Rock Mechanics and Mining Sciences & Geomech. Abstract** 18: 505-515.
- Curran, J. H and Leoun, P. K. (1983). Influence of shear velocity on rock joint strength. In: **Proceedings of International Congress on Rock Mechanics**, Melbourne A235–A240.
- Dieterich, J.H. (1972). Time-dependent friction in rock. **Journal of Geophysical Research** 77(20): 3690-3697.
- Fardin, N., Stephansson, O. and Jing, L. (2001). The scale dependence of rock joint surface roughness. **International Journal of Rock Mechanics and Mining Sciences** 38: 659–669.
- Fenton, C. H., Charusiri, P. and Wood, S. H. (2003). Recent paleoseismic investigations in Northern and Western Thailand. **Annals of Geophysics** 6(5): 957-981.
- Fuenkajorn, K. and Kenkhunthod, N. (2010). Influence of loading rate on deformability and compressive strength of three Thai sandstones. **Geotech. Geol. Eng.** 2010; 28: 707–715.
- Grasselli, G., Egger, P. (2003). Constitutive law for the shear strength of rock joints based on three-dimensional surface parameters. **International Journal of Rock Mechanics & Mining Sciences** 40 (1): 25-40.
- Hoek, E. Shear Strength of Discontinuities. In: Practical rock engineering. Available at: [http://www.rocscience.com/education/hoek\\_corner/](http://www.rocscience.com/education/hoek_corner/) [Date accessed: 2007].
- Homand-Etienne, F., Lefever, F., Belem, T. and Souley, M. (1999). Rock joints behavior under cyclic direct shear tests. Amadei, Kranz, Scott and Smealie

- editions. **Proceedings of the 37<sup>th</sup> U.S. Rock Mechanics Symposium**, June 06-09, 1999, Vail, Colorado, pp. 399-406.
- Jaeger, J.C., Cook, N.G.W., Zimmerman, R.W., 2007. **Fundamentals of Rock Mechanics (4th. Edn.)**. Blackwell Publishing, Malden, 475 p.
- Jaegger, L.C. (1971). Friction of rocks and stability of rock slope. **Geotechnique** 21(2): 97-134.
- Jiang, Y., Xiao, J., Tanabashi, Y. and Mizokami, T. (2004). Development of an automated servo-controlled direct shear apparatus applying a constant normal stiffness condition. **International Journal of Rock Mechanics and Mining Sciences** 41: 275-286.
- Kamonphet, T. and Fuenkajorn, K. (2013). Effect of cyclic loading on fracture shear strength. **Proceeding of the Fourth Thailand Symposium on Rock Mechanics**, January 24-25, 2013, Im Poo Hill Resort, Nakhon Ratchasima, Thailand, Published by Geomechanics Research Unit, Suranaree University of Technology, Nakhon Ratchasima.
- Kapang, P., Walsri, C., Sriapai, T. and Fuenkajorn, K. (2013). Shear strengths of sandstone fractures under true triaxial stresses. **Journal of Structural Geology** 48: 57-7.
- Kemeny, L. (2003). The time-dependent reduction of sliding cohesion due to Rock bridges along discontinuities: a fracture mechanics Approach. **Rock Mechanics and Rock Engineering** 36(1): 27-38.
- Kulatilake, P.H.S.W., Shou, G., Huang, T.H. and Morgan, R.M. (1995). New peak shear strength criteria for anisotropic rock joints. **International Journal of**

**Rock Mechanics and Mining Sciences & Geomechanics Abstracts** 32(7): 673-697.

- Ladanyi B. and Archambault G. (1997). Simulation of shear behaviour of a jointed rock mass. **Proceedings of the 11<sup>th</sup> Symposium of Rock Mechanics**. AIME
- Li, B., Jing, Y. and Wang, G. (2012). Evaluation of shear velocity dependency of rock fractures by using repeated shear tests. **Proceedings of 12th ISRM Congress, Harmonising Rock Engineering and the Environment**, Beijing, China, 2012: 699–702.
- Li, Y., Wang, J., Jung, W. and Ghassemi, A. (2012). Mechanical properties of intact rock and fractures in welded tuff from Newberry volcano. **Proceedings of Thirty-Seventh Workshop on Geothermal Reservoir Engineering**, Stanford University, Stanford, California, January 30 - February 1, 2012: SGP-TR-191.
- Mahawat, C., Atherton, M. P. and Brotherton, M. S. (1990). The Tak Batholith, Thailand: the evolution of contrasting granite types and implications for tectonic setting. **J. Southeast Asian Earth Sci** 4: 11–27.
- Mitchell, E. K., Fialko, Y. and Brown, K. M. (2013). Temperature dependence of frictional healing of Westerly granite: Experimental observations and numerical simulations. **Geochemistry, Geophysics, Geosystems** 14: 567-582.
- Mohr, O. (1914). **Abhandlungen aus dem Gebiete der Technische Mechanik** [Treatise on Topics in Engineering Mechanics], 2<sup>nd</sup> ed., Ernst und Sohn, Berlin.
- Morris, J.P. (2003). Review of rock joint models. **Lawrence Livermore National Laboratory Report**, UCR-ID-153650 (2003)

- Muralha, J., Grasselli, G., Tatone, B., Blumel, M., Chryssanthakis, P. and Yujing, Y. (2013). ISRM Suggested Method for Laboratory Determination of the Shear Strength of Rock Joints: Revised Version. **Rock Mech. Rock Eng** DOI 10.1007/s00603-013-0519-z.
- Naphudsa, P., Tepnarong, P. and Fuenkajorn, K. (2013). Effect of elevated temperatures on shear strength of fractures in granite. **Proceeding of the EIT-JSCE Joint International Symposium on International Human Resource Development for Disaster-Resilient Countries 2013**, September 12-13, 2013, Imperial Queen's Park Hotel, Bangkok, Thailand.
- Naphudsa, P. and Fuenkajorn, K. (2013). Thermal effects on shearing resistance of fractures in granite. **Proceeding of the Conference on Advances in Civil Engineering for Sustainable Development**, 27-29 August 2014, Thailand.
- Olsson, R. and Barton, N. (2001). An improved model for hydromechanical coupling during shearing of rock joints. **International Journal of Rock Mechanics and Mining Sciences** 38: 317–29.
- Patton, F.D. (1966). Multiple modes of shear failure in rock and related materials. **Ph.D. Thesis**, University of Illinois, Urbana.
- Rim, H., Choi, H., Son, B., Lee, C. and Song, J. (2005). Experimental study for shear behavior of pseudo rock joint under constant normal stiffness condition. **Underground Space Use: Analysis of the Past and Lessons for the Future**. Taylor & Francis, London, UK, pp. 175-181.
- Rong-Qiang, W. and Shao-Xian, Z. (2006). Effects of temperature and strain rate on fracture strength of rocks and their influence on rheological structure of the lithosphere. **Chinese Journal of Geophysics** 49(6): 1576-1574.

- Saeb, S. (1990). A variance on Ladanyi and Archambault's shear strength criterion. Barton and Stephansson editors. **Proceedings of the Rock Joints**, Balkema, Rotterdam, pp. 701-705.
- Singh, T.N., Verma, A.K., Kumar, T. and Dutt, A. (2011). Influence of shear velocity on frictional characteristics of rock surface. **Journal of Earth System Science** 120(1): 183-191.
- Stesky, R.M. (1978). Rock Friction-Effect of Confining Pressure, Temperature, and Pore Pressure. **Pure and Applied Geophysics** 116.
- Swan, G. and Zongqi, S. (1985). Prediction of shear behavior of joints using profiles. **Rock Mechanics and Rock Engineering** 18: 183-212.
- Walsri, C., Poonprakon, P., Thosuwat R. and Fuenkajorn, K. (2009). Compressive and tensile strengths of sandstones under true triaxial stresses. **Proceeding of the 2<sup>nd</sup> Thailand Symposium on Rock Mechanics**. Chonburi, Thailand. pp. 199-218.
- Wendai, L. (2000). Regression analysis, linear regression and probit regression. In 13 chapters. **SPSS for windows: statistical analysis**. Publishing House of Electronics Industry. Beijing.
- Yang, Z. Y., Di, C. C. and Yen, K. C. (2001). The effect of asperity order on the roughness of rock joints. **International Journal of Rock Mechanics and Mining Sciences** 38: 745-752.

## **BIOGRAPHY**

Miss. Matsee Kleepmek was born on October 10, 1987 in Changmai province, Thailand. She received her Bachelor's Degree in Engineering (Geotechnology) from Suranaree University of Technology in 2009 and received her Master's Degree in Engineering (Geotechnology) from Suranaree University of Technology in 2011. For her post-graduate, she continued to study with Doctor of Philosophy Program in the Geological Engineering Program, Institute of Engineering, Suranaree university of Technology. During graduation, 2010-2014, she was a part time worker in position of research associate at the Geomechanics Research Unit, Institute of Engineering, Suranaree University of Technology.

